

Towards Optical Spectroscopy of Ultracold Cesium Molecules

Diplomarbeit

zur Erlangung des akademischen Grades
eines Magisters der Naturwissenschaften
vorgelegt von

Dr. Johann Georg Danzl

unter der Betreuung von

a. Univ.-Prof. Dr. Hanns-Christoph Nägerl
Univ.-Prof. Dr. Rudolf Grimm

Institut für Experimentalphysik
an der Fakultät für Informatik, Mathematik und Physik
der Leopold-Franzens-Universität Innsbruck

Innsbruck, im Februar 2007

Contents

1 Introduction	5
2 Ultracold Quantum Gases	13
2.1 Towards Ground State Molecules	14
2.1.1 Ultracold Molecule Production	14
2.1.2 Manipulation of the Internal State of Ultracold Molecules	16
2.2 Interaction of Ultracold Particles	21
2.2.1 Long-Range Interaction between Atoms	22
2.2.2 Two-body Scattering	24
2.2.3 Feshbach Resonances	29
2.3 Bose Einstein Condensation	33
2.3.1 Bose-Einstein Condensation in the Non-interacting Gas	35
2.3.2 Bose-Einstein Condensation in Weakly Interacting Gases	37
3 Molecular Structure	39
3.1 Theory of Diatomic Molecules	40
3.1.1 The Born-Oppenheimer Approximation	41
3.1.2 Spin-Orbit Interaction	47
3.1.3 Hyperfine Interactions	50
3.1.4 Angular Momenta and Hund's Cases	50
3.2 Cs Molecular Structure	56
3.2.1 Ground State of the Cesium Molecule	56
3.2.2 Cs Excited State Potentials	57
3.2.3 Near Threshold Ground State Structure - Feshbach Molecules	60
3.3 Optical Transitions	64
3.3.1 The Franck-Condon Principle	65
3.3.2 Selection Rules	66
3.3.3 Optical Transitions near 1550 nm	69
4 Experimental Setup	71
4.1 The Spectroscopy Setup	72
4.1.1 Spectroscopy Laser	73
4.1.2 Reference Laser	74
4.1.3 The Wavemeter	76
4.1.4 Lock to the Wavemeter	79
4.2 Stabilization Scheme	80

Contents

4.2.1	Optical Resonators	82
4.2.2	Pound-Drever-Hall Prestabilization	86
4.2.3	Scanlock	89
5	Optical Molecular Spectroscopy of Feshbach Molecules	97
5.1	Sample Preparation	97
5.2	Integration of the Spectroscopy Setup into the LevT Experiment	100
5.2.1	Coupling the Spectroscopy Beam into the Experiment	100
5.2.2	Detection of the Spectroscopy Signal	103
5.3	Spectroscopic Measurements	103
5.3.1	Expected Transition Rates	104
5.3.2	Preliminary Results	109
6	Outlook	111
6.1	Optical Spectroscopy	111
6.1.1	Transition Rates	111
6.1.2	Reference Spectroscopy	114
6.1.3	Optical Dipole Traps with 1.55 μm Light	116
6.2	Transfer of Ultracold Cs Molecules to the Absolute Ground State	116
6.2.1	Choice of Initial and Intermediate State	117
6.2.2	Transfer Scheme	118
6.2.3	Alternative Transfer Schemes	122
6.2.4	Extension to Heteronuclear Systems	124
A	Microcontroller Assembler Program	127
A.1	Program code	128
B	Primer on Resonator Optics	141
C	Alignment Instructions for Wavemeter	145
D	Circuit Diagrams	147
D.1	Temperature Stabilization of Optical Resonators	147
D.2	Comparator Circuits	149
D.3	High-Voltage DC-DC Converter	150
	References	151

CHAPTER 1

Introduction

In recent years spectacular success in the field of ultracold quantum gases has sparked enormous interest in ultracold matter. Laser cooling techniques developed in the 1980s [CT98, Chu98, Phi98] led to better atomic clocks [Gib93] and opened up the field of ultracold physics with gaseous atoms and molecules. At ultralow temperatures in the nanokelvin range the thermal de Broglie wavelength associated with the motion of particles increases to values where the description of the gas can only be adequate if it fully takes into account the quantum mechanical wave nature of matter.

In dilute gases of bosonic constituents the cooling process culminates in a distinct phase transition from a thermal gas to a Bose-Einstein condensate (BEC) when the wave-functions of the individual particles start to overlap. This is marked by a macroscopic occupation of the lowest single-particle energy state of the system and results in the formation of a macroscopic matter wave. The first experimental realization of Bose-Einstein condensation came in 1995 [And95, Dav95], 70 years after the proposal by Einstein in 1925 [Ein25].

The coherent matter-wave character of these systems has since then been impressively confirmed by the experimental observation of matter-wave interference [And97], the generation of solitons and quantized vortices [Bur99, Den00, Str02, Kha02, Mat99, AS01], the observation of the superfluid to Mott-insulator transition [Gre02], and the generation of matter-wave lasers [Mew97, Hag99], to name just a few examples. Ultracold quantum gases can be prepared in precisely controlled states and are therefore amenable to detailed theoretical analysis, providing a stringent test for quantum theory. In addition, they allow measurements of fundamental quantities such as the fine structure constant, the gravitational constant or the electron dipole moment at an unprecedented level of precision [Ude02, Ye06b].

Following the achievement of Bose-Einstein condensation of atomic gases there has been an ever increasing interest in attaining the same degree of coherence in molecular systems and in fully controlling their properties at the quantum level. This has proven to be more challenging than for atoms due to the complex internal energy structure of molecules that hampers direct laser cooling. The most fruitful approach in the quest for Bose-Einstein condensation of molecules so far has been to cool an atomic sample to ultralow temperatures and then to associate atoms pairwise to very weakly bound dimer molecules. The resulting molecular ensemble has the same translational temperature as the atomic ensemble. This technique resulted in the formation of the first pure molecular quantum gas by our group in 2002 [Her03] and shortly thereafter

1 Introduction

by the Garching group [Dür04] and the MIT group [Xu03]. These molecules were formed from bosonic alkali atoms by means of a magnetic field ramp over a magnetically tunable Feshbach resonance, resulting in so-called Feshbach molecules. The molecules created in this association process are translationally very cold but vibrationally highly excited, i.e. very weakly bound. The presence of many lower lying bound molecular states renders these bosonic Feshbach molecules very sensitive to inelastic molecule-molecule collisions. Inelastic collisions lead to rapid loss from the molecular sample and therefore impede the Bose-Einstein condensation of Feshbach molecules consisting of bosonic atomic species.

The same strategy of Feshbach association was pursued with fermionic quantum gases. Fermionic atoms were associated from a two-component spin mixture to molecules of bosonic character. Due to a Pauli-blocking effect the resulting molecules proved to be much more stable against inelastic losses than their counterparts consisting of bosonic atoms. This finally led to the creation of the first Bose-Einstein condensate of molecules in Innsbruck [Joc03a] and at the same time in Boulder [Gre03]. These systems constitute extremely rich model systems for investigating phenomena in solid state physics such as superconductivity and have opened up the exciting possibility to study the crossover between a molecular condensate and a superfluid of Cooper pairs, the so-called BEC-BCS (Bardeen-Cooper-Schrieffer) crossover regime [Bar04b, Bar04a, Chi04a, Zwi05].

Ultimate control over all degrees of freedom is afforded by placing the ultracold quantum gas in an optical lattice potential [Gre02]. The number of particles per lattice site can be controlled at will, interaction between the particles can be tailored and the internal quantum state of the individual particles can be engineered. Therefore, these systems constitute very well controlled model systems for solid state physics and for fundamental quantum mechanics.

With the ability to control the internal states of atoms and molecules at the quantum level, coherent chemistry has come within reach [Hei00]. Ultracold molecules allow precision measurements leading to a better understanding of molecular structure [Chi04b]. Work is under progress to use cold dipolar molecules as quantum bits for quantum computation [DeM02, Sag05] and for the measurement of fundamental physical quantities such as the electron's dipole moment [Hud02, Stu04] that could potentially lead to new physics beyond the standard model. Recently, with the experimental confirmation of the existence of Efimov quantum states [Kra06b], a particular type of three-body bound states, the door to few-body quantum physics in the so-called universal regime has been opened up.

One important aim for the near future is the production of a BEC of molecules in their rotational and vibrational ground state. Such rovibrational ground state molecules would be stable against molecule-molecule collisions. The most promising experimental approach proposed by the Zoller group [Jak02] is to load an atomic BEC into an optical lattice and then to associate the atoms pairwise to vibrationally highly excited molecules with essentially unit efficiency. While in the lattice, the molecules are shielded from inelastic collisions. The molecules then will have to be trans-

ferred to their internal ground state. This should be possible by one or several steps of two-photon transitions involving electronically excited states. The authors specifically discuss a three-step process in Rb_2 to reach the vibrational ground state. The thus stabilized molecules can then be released from the lattice and would in principle form a molecular BEC.

The project presented in this thesis is aimed at optical spectroscopy of ultracold cesium (Cs) Feshbach molecules. The interest in this spectroscopy is twofold: First, the spectroscopy *per se* has implications for the derivation of more accurate molecular parameters. Second, and more importantly, precise spectroscopic knowledge of the first electronically excited state is necessary to drive two-photon processes to the vibrational ground state of the Cs dimer, as illustrated qualitatively in figure 1.1. The transitions we intend to drive represent the first step in such a two-photon process that would lead to the stabilization of the molecules against collisional losses as required for the production of a BEC of molecules in their rovibrational ground state.

There are distinct advantages of using ultracold samples for spectroscopy [Wei99, Bur02]. The virtual absence of the Doppler effect at ultralow temperatures allows high precision measurements which do not suffer from line broadening and line shifts. In addition, low temperatures allow trapping of the spectroscopic sample [Met99, Tak98] and therefore enable long interaction times such that even very weak transitions can be probed. The present study focuses on the wavelength range around 1550 nm, corresponding to energies of 6330 cm^{-1} - 6620 cm^{-1} above the $6S + 6S$ asymptote of two free ground state Cs atoms. This choice is motivated by the following points:

- The theoretical uncertainties for computed transition wavelengths based on ab initio potential curves are rather large in this region [Koc06a, Dul06] and can be improved by experimental input. There is data available from “classical” Fourier transform spectroscopy experiments, see e.g. reference [Ver87]. Spectroscopy of ultracold molecules can provide very high precision data in principle with sub-linewidth resolution. Feshbach molecules are slowly rotating and therefore we address rovibrational states with low rotational quantum numbers. This is in contrast to the classical spectroscopic experiments and reduces the uncertainty in determining “rotationless” molecular potentials.
- The two 0_u^+ electronically excited state potentials feature an avoided crossing that merits additional investigation. Spin-orbit coupling [LB04] leads to mixing of the underlying singlet and triplet states (see sections 2.2.1 and 3.2.2) and therefore helps to circumvent the usual spin selection rule in electric dipole transitions. Even more importantly, spin-orbit coupling can change Franck-Condon factors and accordingly transition probabilities drastically.
- When driving a two-photon process to the molecular vibrational ground state ($v=0$), the second laser coupling the electronically excited state to the $v=0$ ground state level could potentially drive unwanted optical transitions of the Feshbach molecules to the electronically excited state manifold. An important

1 Introduction

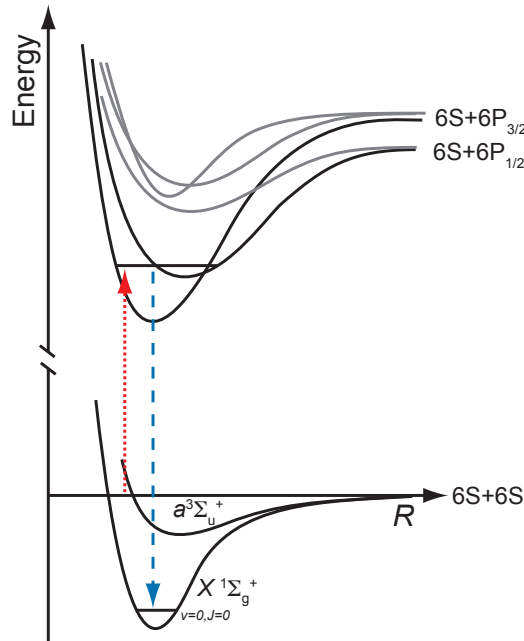


Figure 1.1: Transfer of Feshbach molecules to the vibrational ground state: Molecular potential curves for the electronic ground state and for several of the electronically excited states dissociating to the $6S + 6P_{1/2}$ and $6S + 6P_{3/2}$ atomic asymptotes of Cs are shown schematically. Molecular energy is plotted as a function of internuclear distance R . The potential curves dissociating to the $6S + 6S$ atomic threshold are the $X^1\Sigma_g^+$ singlet electronic ground state and the $a^3\Sigma_u^+$ lowest triplet state. Each of the potentials supports a series of bound rovibrational states. Rovibrational states correspond to horizontal lines. Feshbach molecules are very weakly bound and vibrationally highly excited. Their binding energy cannot be resolved on the scale of this plot, it is just below the $6S + 6S$ asymptote. The arrows indicate a two-photon process that transfers the population from loosely bound Feshbach state to the lowest rovibrational level ($v = 0, J = 0$) of the singlet ground state via an intermediate electronically excited state.

advantage of the chosen wavelength region is that the wavelength of the second laser can be chosen far from any optical transition of the Feshbach molecules because the vibrational level spacing in the region of the excited state potentials reached by the second laser from the Feshbach molecules is still large. Sufficient detuning from any molecular resonances suppresses such “parasitic” transitions driven by the second laser.

- Similarly, the 1550 nm laser used in the first step of the process is not expected to couple the $v=0$ level of the molecular ground state to any excited state levels. Again, parasitic transitions leading to molecular loss can be avoided.
- This project is also intended to clarify preliminary results previously obtained in our group with a borrowed laser in the same wavelength region. Although indi-

cations of molecular optical transitions in that wavelength region were thought to be seen with the borrowed laser, they were not reproducible and a thorough workup was not possible due to time limitations. This lack of reproducibility was attributed to insufficient stability of the free running laser and it was decided to evaluate these preliminary results more deeply in the framework of the present study.

- Many interesting experiments rely on the ability to trap the ultracold molecules. We currently trap molecules in quasi-electrostatic CO₂-laser traps. Because of its long wavelength of 10.6 μm CO₂-laser light does not drive any molecular transitions. However, these lasers are not suited to implement optical lattice potentials because the distance between individual lattice sites would be too large. We are interested in trapping ultracold molecules in a lattice with far off-resonant light, reducing the scattering rate from the trapping light with respect to near resonant light. High power lasers and amplifiers are available in two wavelength bands: 1064 nm and 1550 nm. We investigated the possibility to trap molecules with a broadband 1064 nm source by irradiating a sample of ultracold molecules trapped in a CO₂-trap with the 1064 nm light. We observed rapid molecular loss due to optical molecular transitions and concluded that this was not a good option. Narrow bandwidth 1064 nm light has been tested as well and seems to be a viable alternative. In the 1.55 μm region there are less potentials that can be reached and vibrational level spacing is larger than in the 1064 nm region, making it easier to avoid molecular resonances for the trapping. Therefore, the 1.55 μm wavelength region is attractive for trapping and for generating optical lattices. The current project is also intended to evaluate this possibility.
- A technical advantage of the wavelength region around 1.5 μm is the commercial availability of highly stable, widely tunable laser sources developed for the telecommunication industry.

The type of spectroscopy presented here should be distinguished from photoassociation spectroscopy. Photoassociation occurs when two colliding atoms absorb a photon and are thereby transferred to an electronically excited bound molecular state [Jon06, MS01]. The excited state can then decay back into two free atoms or into a bound molecular state in the electronic ground state. In the present study, we already start from weakly bound molecules formed by Feshbach association. Accordingly, transition probabilities at a given detuning from the excited state asymptote are larger than in the case of photoassociation due to more favorable wave function overlap. This potentially enables the study of more deeply bound levels in the electronically excited state.

In contrast to classical laser spectroscopic experiments that start from low lying vibrational levels in the ground state we start from very high vibrational ground state levels, with the potential to address higher vibrational levels in the electronically excited manifold. In that sense, this type of spectroscopy closes a gap between classical laser

1 Introduction

spectroscopy on molecular beams and photoassociation spectroscopy. In the present study, we work in a region of very large detunings from the excited state asymptotes, i.e. with low lying vibrational level in the electronically excited state, which is also accessible to classical spectroscopy [Ver87]. We can however obtain a much higher resolution than in typical classical spectroscopic experiments.

This project is intended to explore one possible route for the formation of a ground state molecular BEC. For the formation of a molecular BEC we want to start from a very cold and dense atomic sample, i.e. from a sample with high phase space density. During the process of molecule creation and transfer to the rovibrational ground state a high phase space density must be maintained and must finally reach the condensation threshold implying that molecule production and the population transfer mechanism to the rovibrational ground state should be very efficient. The requirements for the production of a molecular BEC are by far more stringent than in other experiments involving ultracold ground state molecules such as quantum computing with polar molecules [Sag05].

This thesis is organized as follows. Chapter 2 provides an introduction to the field of ultracold quantum gases with special emphasis on molecular quantum gases. It gives a brief overview over the formation of ultracold molecules and strategies to reach a molecular BEC in the absolute internal ground state in section 2.1. Interactions between ultracold particles are discussed in some detail in 2.2. This provides the basis for the formation of ultracold molecules by means of Feshbach resonances as discussed in section 2.2.3 and sets the framework for integrating the two approaches to ultracold molecules relevant to the optical spectroscopy of Feshbach molecules, namely the “atomic” viewpoint and the “molecular” viewpoint. Chapter 2 closes with a brief primer concerning the physics of Bose-Einstein condensation in section 2.3 in order to put the present study in the context of its primary goal, namely the creation of a ground state molecular BEC.

Chapter 3 provides a brief review of molecular theory aimed at the reader unfamiliar with molecular structure. It emphasizes the structure of homonuclear diatomic molecules in section 3.1. The next section is dedicated to the structure of cesium molecules, both in the electronic ground state and in the first electronically excited state. The treatment of the ground state molecular structure includes a discussion of the properties of Cs Feshbach molecules. Optical molecular transitions to electronically excited states and in particular transitions from Feshbach molecular states to electronically excited states in the wavelength region around 1550 nm are addressed in section 3.3 together with the relevant selection rules.

Chapter 4 lays out the experimental setup including the tunable stabilization of the spectroscopy laser. A stabilization scheme was developed that allows for stabilization on a sub-MHz level during an experimental run while maintaining full tunability of the wavelength. The spectroscopy laser and a reference laser locked to an atomic hyperfine transition are coupled into an optical resonator that is continuously scanned. The locking scheme stabilizes the position of a transmission resonance of the spectroscopy laser relative to two adjacent resonances of the reference laser. To achieve a narrow

linewidth, the spectroscopy laser is prestabilized to a second optical resonator with the Pound-Drever-Hall method. A Michelson interferometer type wavemeter is used in addition to measure the wavelength of the spectroscopy laser.

Chapter 5 is dedicated to the spectroscopy experiments conducted so far. It sets out with a description of the preparation of ultracold molecules in section 5.1. The integration of the spectroscopy setup into the Cs BEC experiment or, synonymously, into the LevT experiment is discussed in section 5.2. Preliminary results are discussed in section 5.3 in conjunction with the transition rates expected for our experimental parameters.

Chapter 6 provides an outlook where technical improvements and the prospects of reaching a molecular ground state BEC are discussed.

In the appendix, a primer on resonator optics and some additional technical information such as a commented version of the assembler code used for a microcontroller-based laser stabilization and electronic circuit designs are given.

CHAPTER 2

Ultracold Quantum Gases

Ultracold *quantum* gases as opposed to classical gases equate with a regime where the quantum nature of matter plays a prominent role. Ultracold quantum gases for the first time provide the means to prepare an atomic or molecular sample with full control over external and internal degrees of freedom. They allow the preparation of pure quantum states at will and the coherent manipulation of matter.

The present study is intended to lay the groundwork for the production of a Bose-Einstein condensate of molecules in their absolute internal ground state. This chapter deals with the concepts needed to understand the production of ultracold molecules, the manipulation of their internal state and the formation of a Bose-Einstein condensate.

Section 2.1 first explains the different strategies to produce ultracold molecules in a general way and then deals with the manipulation of the internal state of ultracold molecules. We use magnetically tunable Feshbach resonances for ultracold molecule formation. The resulting molecules are therefore called Feshbach molecules. The main part of the chapter is dedicated to the knowledge specifically required for understanding the molecule production technique employed in our experiments. This procedure is closely linked to the particularities of two-body scattering processes in ultracold quantum gases. Section 2.2 provides the background on ultracold interactions necessary to understand the concept of Feshbach molecules. In the ultracold regime, long range interactions play an important role and therefore they are discussed in section 2.2.1. The concepts of elastic and inelastic scattering are introduced in section 2.2.2. Ultracold elastic scattering processes can be fully described by a single parameter, namely the *s*-wave scattering length and therefore some emphasis is put on this important concept. This leads to the discussion of Feshbach resonances in section 2.2.3. They arise when a bound state in a so-called closed channel couples to the incident scattering state. The properties of Cs Feshbach molecules are discussed more fully in section 3.2.3.

The chapter concludes with an outline of the physics of Bose-Einstein condensation in section 2.3, considering briefly the quantum statistical basis for Bose-Einstein condensation in section 2.3.1 and the case of real gases exhibiting weak interactions in section 2.3.2. This background is useful for understanding the work towards a BEC of molecules in their absolute internal ground state.

2.1 Towards Ground State Molecules

In our experiments, we associate ultracold molecules from an ultracold atomic sample of bosonic ^{133}Cs atoms by means of magnetically tunable Feshbach resonances [Her03, Mar05]. This technique in principle allows coherent transfer from the atomic scattering state to a bound molecular state and results in translationally very cold, but vibrationally highly excited or “hot” molecules. Before discussing the foundations of this molecule production scheme in more detail, we will take a broader look at different strategies to produce ultracold molecules in section 2.1.1. Strategies to manipulate the internal state of ultracold molecules are required for the production of a molecular ground state BEC. These are discussed in section 2.1.2.

2.1.1 Ultracold Molecule Production

Molecules are to date not amenable to direct laser cooling that has been so highly successful in the quest for ever lower temperatures and for Bose-Einstein condensation of atomic gases. This inability is due to the highly complex energy structure of molecules preventing the implementation of a simple closed cooling cycle. Two basic strategies to produce ultracold molecules have been employed: association of molecules from precooled atoms and direct cooling of molecules.

Association of Molecules from Precooled Atoms

An atomic sample can be laser cooled and then molecules can be associated from these precooled atoms. Feshbach association results in very weakly bound molecules. Photoassociation of atoms results in molecules in an electronically excited state. These either decay to free atoms or to loosely bound levels in the electronic ground state. Clearly, this approach is restricted to a narrow set of molecular species, i.e. diatomic molecules, and one could term the vibrationally highly excited or very weakly bound molecules “physicist’s molecules” because their properties can very precisely be traced back to properties of the constituent atoms [Jon06].

Magnetically Tunable Feshbach Resonances Ultracold molecule production by means of magnetically tunable Feshbach resonances is discussed in section 2.2.3.

Photoassociation Photoassociation was the first technique to associate laser cooled atoms to bound molecules. Two colliding atoms absorb a photon while they are transferred to an electronically excited bound molecular state. This state can then decay back to two free atoms but it also has a certain probability to decay to weakly bound molecular ground state levels, as illustrated in figure 2.1. The resulting ground state molecules normally have high vibrational quantum numbers but, due to the properties of ultracold collisions discussed in section 2.2.2, have low rotational quantum numbers.

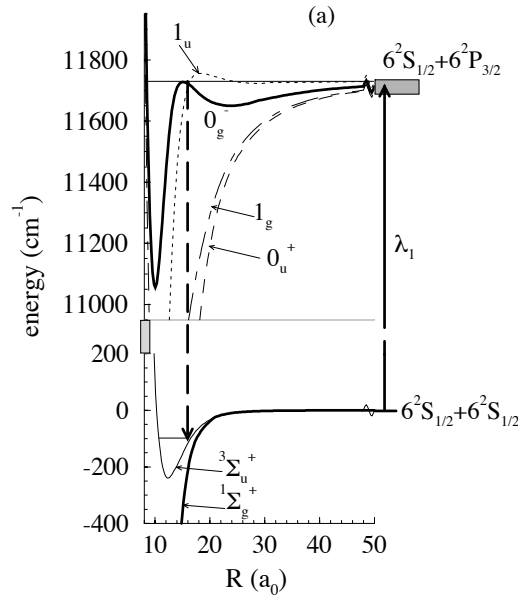


Figure 2.1: Photoassociation of two colliding Cs atoms: At large internuclear distance, the colliding atoms absorb a photon λ_1 . The resulting electronically excited state molecule can then decay back to the continuum of two free atoms (not indicated) leading to trap loss or to bound levels of the singlet ground state $^1\Sigma_g^+$ or lowest triplet state $^3\Sigma_u^+$, indicated by the dashed arrow. This second step can either involve spontaneous emission of a photon or stimulated emission in the case of two-color photoassociation. For both the electronic ground and excited states only the region near the dissociation threshold is shown. Figure taken from [Fio98].

Photoassociation of laser cooled atoms was first demonstrated by the Heinzen group in 1993 for Rb atoms [Mil93]. The first photoassociation of cold Cs molecules was performed by the Orsay group in 1997 [Fio98]. Crucial to our experiments is the ability to trap molecules of different internal states. This is most conveniently done by means of an optical far-off resonance trap (FORT). The first direct observation of optically trapped cold neutral molecules was reported by Knize and coworkers in 1998 [Tak98]. They employed CO_2 lasers to trap ultracold Cs_2 molecules generated by photoassociation. CO_2 laser light does not drive any molecular transitions, which makes it well suited to trap molecules. The recent review article by Jones, Tiesinga, Lett, and Julienne gives a very good overview of the different aspects of photoassociation [Jon06], the review article by Masnou-Seeuws and Pillet puts special emphasis on the Cs experiments [MS01].

Direct Cooling of Molecules

The second approach to cold molecule production is to take stable molecules and cool them directly by means other than laser cooling. The phase space densities (see section 2.3) achieved hitherto with this approach are orders of magnitude below those required

for Bose-Einstein condensation. The great advantage of this method is that a larger variety of molecular species, in particular more complex molecules, can potentially be cooled. The most established technique for directly cooling molecules is buffer-gas cooling [Wei98]. Slowing of supersonic jets of polar molecules can be achieved by pulsed electric fields in Stark-decelerators [Bet99, Bet00].

2.1.2 Manipulation of the Internal State of Ultracold Molecules

It is important to have means to precisely control and manipulate the internal state of molecules in order to transfer the Feshbach molecules to more tightly bound molecular states. The basic discussion here follows the review article by Vitanov, Halfmann, Shore, and Bergmann [Vit01] and an earlier review article by the same group [Ber98].

Incoherent Population Transfer

When a two-state system where the population is initially in the lower state is illuminated with intense light of the appropriate frequency from an incoherent light source, the population in the excited state will monotonically approach its saturation value of 50%.

Optical pumping Optical pumping is a widely used method for population transfer in a three-level system and exploits spontaneous emission. If states $|1\rangle$ and $|2\rangle$ are coupled by a light field and $|2\rangle$ spontaneously decays to state $|3\rangle$ that has an energy such that the radiation field cannot transfer it to either $|1\rangle$ or $|2\rangle$, population will be effectively transferred from $|1\rangle$ to $|3\rangle$. Optical pumping does not require a coherent light source and has been used widely to prepare atoms in a defined stable or metastable state. In the case of molecules, it suffers from severe limitations due to lack of selectivity. When excited state molecules decay into ground state vibrational levels, the transition probabilities to the individual levels are governed by the Franck-Condon (FC) factors, as discussed in section 3.3.1, that are of similar magnitude for neighboring levels.

Stimulated emission pumping Stimulated emission pumping takes this idea further by not only coupling states $|1\rangle$ and $|2\rangle$ by means of a pump field but also states $|2\rangle$ and $|3\rangle$ with a dump or Stokes field that is supplied after the pump field. Such a three level coupling scheme is shown in figure 2.2. The Stokes field leads to stimulated emission from state $|2\rangle$ to $|3\rangle$. If the pump field is strong enough to saturate the first transition, 50% of the population is transferred to state $|2\rangle$. If the dump field is then strong enough to saturate the second transition, again 50% of the population of state $|2\rangle$ are transferred to $|3\rangle$, the rest decaying according to the natural branching fraction of spontaneous emission of state $|2\rangle$. This yields an overall transfer efficiency of 25%. The scheme can be improved to a transfer efficiency of 1/3 if the pump and dump fields

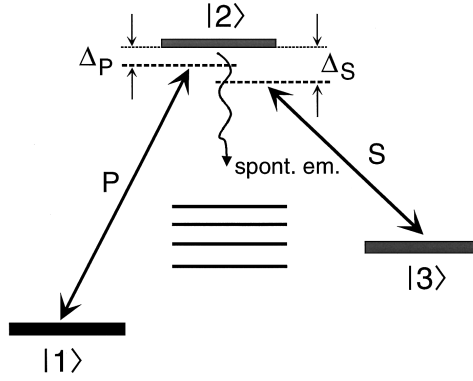


Figure 2.2: Three level coupling: States $|1\rangle$ and $|3\rangle$ are coupled by the pump field P (with a detuning Δ_P) and the Stokes field S (with a detuning Δ_S) via an intermediate level $|2\rangle$ that can decay by spontaneous emission to other states. The basic coupling scheme holds both for coupling by incoherent radiation and by coherent radiation. Figure taken from [Ber98].

are supplied simultaneously. Stimulated emission pumping has been applied recently in the group of David DeMille [Sag05] to produce ultracold RbCs molecules in the $\nu = 0$ level of the singlet ground state potential.

Transfer by Coherent Methods

Application of coherent radiation resonant with the energy spacing of a two level system results in an oscillatory behavior of the population in the excited state, known as Rabi oscillations. Their frequency Ω is related to the strength of the transition by

$$\Omega(t) = \frac{\mathbf{D}_{12} \cdot \boldsymbol{\varepsilon}(t)}{\hbar} \quad (2.1)$$

with the dipole matrix element \mathbf{D}_{12} between states $|1\rangle$ and $|2\rangle$ and the envelope of the electric field amplitude of the laser $\boldsymbol{\varepsilon}(t)$. Planck's constant divided by 2π is denoted by $\hbar = 1.05457168 \times 10^{-34}$ J s. The population can in principle be completely transferred to the excited state for $\Omega t = \pi, 3\pi, \dots$. This concept can be generalized to three-level systems with the analogous result that in principle complete population transfer is possible. It should be kept in mind, however, that the population then actually passes through an intermediate state and inevitable population losses take place by spontaneous emission unless the excitation time is much shorter than the lifetime of the intermediate state.

To alleviate the problem of losses due to spontaneous decay of the intermediate level, the two lasers can be detuned from the resonance frequency, creating a two-photon resonance with a “virtual” excited state, i.e. a two-photon Raman transition. The effective Rabi frequency for such a process is $\Omega = \frac{\Omega_1 \Omega_2}{2\Delta}$, where $\Omega_{1,2}$ are the Rabi frequencies for the first (second) step and Δ is the detuning from the intermediate state.

2 Ultracold Quantum Gases

The effective spontaneous emission rate is $\gamma = \gamma_i \frac{\Omega^2}{4\Delta^2}$, where γ_i is the natural linewidth of the intermediate state [Jak02].

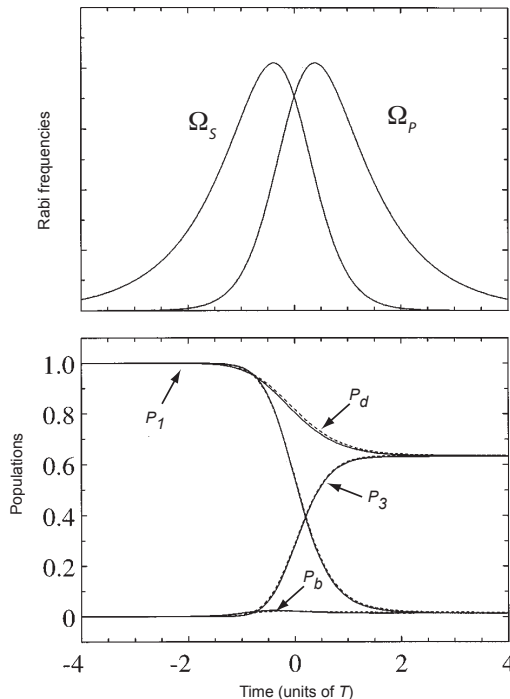


Figure 2.3: STIRAP pulse sequence and population transfer: *top:* The Stokes pulse with Rabi frequency Ω_S is applied before the pump pulse Ω_P with temporal overlap between the two pulses. *bottom:* STIRAP with transfer via a decaying state. The population P is transferred from the initial state $|1\rangle$ ($P_1 = 1$) to the final state $|3\rangle$ with population P_3 . The dark state with population P_d corresponds to the adiabatic state $|0\rangle$. Hardly any population reaches the bright state (P_b) from which decay can occur. In an ideally adiabatic situation, no population at all would be dissipated and the final state population P_3 would reach unity. Figure adapted from [Vit97].

STIRAP A completely different and at first sight surprising two-photon transfer scheme is the *Stimulated Raman Adiabatic Passage* (STIRAP) scheme [Ber98, Vit01]. In the usual sequence of pulses discussed above first a pump pulse is applied to transfer population from the initial state $|1\rangle$ to the intermediate state $|2\rangle$ and then a dump or Stokes pulse is applied to transfer population from $|2\rangle$ to $|3\rangle$. In STIRAP, first the Stokes pulse is supplied that couples $|2\rangle$ and $|3\rangle$. Then, with some temporal overlap, the pump pulse coupling $|1\rangle$ and $|2\rangle$ is supplied, as illustrated in figure 2.3. The light field induces a coupling between the bare states $|1\rangle$, $|2\rangle$ and $|3\rangle$, resulting in three new adiabatic states $|+\rangle$, $|-\rangle$ and $|0\rangle$. The adiabatic state $|0\rangle$ is a coherent superposition of states $|1\rangle$ and $|3\rangle$ only with no contribution from the excited state $|2\rangle$. Hence, state $|0\rangle$

allows for efficient populations transfer on time scales exceeding the lifetime of state $|2\rangle$. The relative contributions from the individual bare states to each of the adiabatic states evolve with time according to the evolution of the Rabi frequencies of the Stokes and pump pulse, Ω_S and Ω_P , respectively. For state $|0\rangle$ this relation reads

$$|0\rangle = \cos \vartheta(t)|1\rangle - \sin \vartheta(t)|3\rangle, \quad (2.2)$$

where $\vartheta(t)$ is the mixing angle between states $|1\rangle$ and $|3\rangle$ given by

$$\tan \vartheta(t) = \frac{\Omega_P(t)}{\Omega_S(t)}. \quad (2.3)$$

Initially all the population resides in state $|1\rangle$. When the Stokes pulse is applied and the pump pulse is still off, the mixing angle ϑ is zero. As the Stokes pulse declines and the pump pulse takes over, the mixing angle smoothly evolves to a value of $\frac{\pi}{2}$. At the end of the pulse sequence, the adiabatic state $|0\rangle$ has only contributions from $|3\rangle$, ideally resulting in 100% transfer efficiency from the initial to the final state. The necessary conditions for STIRAP are (i) two photon resonance between states $|1\rangle$ and $|3\rangle$, (ii) counterintuitive pulse ordering, and (iii) adiabatic evolution. In the *adiabatic limit* which corresponds to this idealized situation, no population resides in state $|2\rangle$ at any time and therefore its properties do not influence the transfer process. However, in reality, the adiabatic limit is only approximately reached. If the coupling is insufficient, i.e. if the Rabi frequencies are too small, some population will reach the leaky state $|2\rangle$ and irreversible radiative decay out of the three-level system can ensue. Dissipation from the intermediate state reduces the transfer efficiency to below unity.

Vitanov and Stenholm [Vit97] discuss an analytical model from which they derive the dependence of the final state population on the decay rate of the intermediate state in the limit of low dissipation

$$P_3 \sim \exp\left(\frac{-\pi^2\gamma}{2\alpha^2}\right), \quad (\alpha^2 \gg \pi\gamma) \quad (2.4)$$

where γ is the dimensionless decay rate of the intermediate state $\gamma = \Gamma \cdot T$, with the characteristic pulse length T and the intermediate state decay rate Γ . The parameter α is proportional to the pulse area, i.e. the time integral of the Rabi frequencies. The peak Rabi frequencies are taken equal for both pulses.

In numerical simulations of the three-level system with a decaying intermediate state

$$i\frac{d}{dt}\begin{pmatrix} c_1 \\ c_2 \\ c_3 \end{pmatrix} = \begin{pmatrix} 0 & \Omega_P & 0 \\ \Omega_P & \Delta - i\Gamma & \Omega_S \\ 0 & \Omega_S & 0 \end{pmatrix} \begin{pmatrix} c_1 \\ c_2 \\ c_3 \end{pmatrix} \quad (2.5)$$

we empirically found a condition for efficient transfer that is equivalent to the low dissipation condition of equation 2.4. Here, we used the rotating wave approximation and set the detuning from the two-photon resonance to zero. The detuning from the

intermediate state is $\Delta = \Delta_S = \Delta_P$. Decay from the intermediate state is modeled by the term $-i\Gamma$. The condition for efficient transfer then reads

$$T \cdot \left(\frac{\Omega_m}{2\pi}\right)^2 \gg \Gamma, \quad (2.6)$$

where Ω_m is the peak Rabi frequency which is taken equal for both pulses. Half of the population is transferred to the final state $|3\rangle$ if both sides of equation 2.6 are equal.

STIRAP has recently been used in our group to transfer ultracold Feshbach molecules from their initial vibrational state to the next lower lying vibrational level [Win06b].

Further Transfer Schemes The idea to use time resolved wave-packet dynamics to tailor the internal state of molecules has been studied mainly theoretically so far. It was proposed that chirped pulses and optimal control theory could lead to preferential transfer of molecules to specific low vibrational states in two-color photoassociation experiments [LK04, Koc06b].

We recently demonstrated the possibility to populate a variety of weakly bound molecular states by adiabatically following avoided crossings between states by means of magnetic field ramps or non-adiabatically jumping the crossings [Mar07]. Although this technique gives an extremely high degree of control over the internal state of molecules, it is only applicable to states close to the scattering threshold.

Another possibility is to transfer molecules from one ground state vibrational level to the next lower lying levels by means of microwave radiation. Going down the vibrational ladder a few steps might improve the starting position for two-photon transitions to very low-lying vibrational levels.

Ground State Molecule Production

There is a series of proposals of how to transfer weakly bound ultracold molecules to the vibrational and rotational ground state ($v = 0, J = 0$) of the electronic molecular ground state $X^1\Sigma_{(g)}^+$. This section is intended as a first introduction whereas the topic is discussed in some more detail in section 6.2.

The proposal by Zoller and coworkers for the production of a ground-state molecular BEC [Jak02] has already briefly been mentioned in the introduction. It involves molecule production and transfer to the ground vibrational state in an optical lattice where the molecules are shielded from inelastic molecule-molecule collisional losses and subsequent release from the lattice. The molecules are first formed by two-color photoassociation and then transferred to the rovibrational ground state by two consecutive two-photon transfer steps. The authors give guidelines for the case of Rb_2 . Instead of two-color photoassociation, we would form molecules via Feshbach association (see sections 2.2.3 and 3.2.3).

In the case of heteronuclear diatomic molecules, the absence of the *gerade/ungerade* symmetry of homonuclear dimers is advantageous. Excitation can

occur via the triplet component of the Feshbach molecules and singlet/triplet mixing in the electronically excited state can be exploited for transfer to the singlet ground state. Stwalley [Stw04] discusses the transfer of dialkali Feshbach molecules to the ($X^1\Sigma^+, v = 0, J = 0$) state via an intermediate state with mixed $b^3\Pi$ and $A^1\Sigma^+$ character (for state labeling conventions, see section 3.1.1). With the current spectroscopy setup we are addressing mixed $b^3\Pi_u/A^1\Sigma_u^+$ states in Cs_2 , see section 3.2.2.

DeMille and coworkers [Sag05] recently transferred ultracold RbCs molecules formed by photoassociation to the vibrational ground state with a rather narrow distribution of the rotational quantum number. They exploited singlet/triplet mixing in the excited state as analyzed in reference [Ber04]. The scheme relied on singlet/triplet mixing of energetically somewhat higher lying states than suggested by Stwalley.

2.2 Interaction of Ultracold Particles

The realization that cold collision phenomena would open up an exciting new field of physics came with early work on spin polarized hydrogen in the 1970s. The field experienced a dramatic surge with the advent of laser cooling techniques [CT98, Chu98, Phi98] in the 1980s pushing the temperature limits to the millikelvin and microkelvin range. Evaporative cooling [Ket96] has provided us with the possibility of performing experiments at nanokelvin temperatures and to reach quantum degeneracy and Bose-Einstein condensation.

The temperature range accessible via Doppler and polarization gradient cooling between ~ 1 mK and ~ 1 μ K is often termed the regime of *cold* collisions [Wei99]. Here, the quantum mechanical wave nature of the particles becomes important. The de Broglie wavelength

$$\lambda_{dB} = h/p, \quad (2.7)$$

with Planck's constant h and particle momentum $p = (2mE)^{1/2}$ becomes comparable to or longer than the chemical bond length.

The *ultracold* regime is reached when the de Broglie wavelength grows to a scale comparable to the mean distance separating atoms in a dilute gas at the critical density for Bose-Einstein condensation (see section 2.3). Wave functions of the individual atoms start to overlap and the atomic ensemble enters the regime of quantum degeneracy. The de Broglie wavelength is on the order of micrometers which is enormous in comparison to the diameter of an atom or the typical chemical bond length. 1 μm corresponds to 1.9×10^4 a_0 or Bohr radii, whereas atomic diameters are less than 10 a_0 . As will be detailed below in this regime scattering between ground state atoms takes place through radial motion and is isotropic. Ultracold collisions can largely be described in terms of a single parameter a , the s -wave scattering length. The translational energy of the atoms lies below the recoil imparted on the atom by scattering of a single photon. The study of ultracold collision processes is motivated by their relevance to the following areas [Wei99, Bur02]:

1. Quantum degenerate gases: First, when trapping particles magnetically or optically, one has to understand trap loss mechanisms that result from particle collisions. Second, the ratio of elastic or “good” collisions and inelastic or “bad” collisions determines whether quantum degeneracy can be reached by evaporative cooling.
2. Precision Measurements: In photoassociation spectroscopy the scattering state is coupled to an electronically excited molecular state. This has been used to study long-range excited states not amenable to classical spectroscopy as well as the properties of the scattering wave function and near threshold ground state levels. Conventional laser spectroscopic techniques can only address tightly bound levels both in the ground and excited states easily. Feshbach spectroscopy allows for extremely precise analysis of the molecular structure right below the scattering threshold if combined with a thorough theoretical analysis [Chi04b]. Our definition of the second rests on the hyperfine splitting of the Cs ground state atom. Atomic collisions cause density dependent clock shifts [Gib93, PDS02] and their study is of particular interest to build better atomic clocks.
3. Control of the outcome of collisions: It has long been the dream of chemists and chemical physicists to be able to precisely control the outcome of a collision between two particles, i.e. to control chemical reactions on a quantum level. In the realm of ultracold particles the scattering properties can be tuned by external optical or magnetic fields. The scattering state can be transferred to a bound state, thereby inducing the formation of molecules as discussed in more detail in section 2.2.3. Ultimate control over particle interactions can be achieved in an optical lattice.

2.2.1 Long-Range Interaction between Atoms

The Hamiltonian that describes a system of two interacting ground state alkali atoms is composed of the atomic Hamiltonian for each atom, a kinetic energy operator for the relative radial motion, two Born-Oppenheimer potentials with symmetry $^1\Sigma_g^+$ and $^3\Sigma_u^+$ (see section 3.1.1), the nuclear rotation operator $\frac{\hbar^2 \ell^2}{2\mu R^2}$, and weaker relativistic interactions H_{rel} . Here ℓ denotes the nuclear mechanical angular momentum, μ is the reduced mass of the atom pair and R the separation between the two nuclei. The *van der Waals* interaction and the *exchange* interaction can be viewed as the mean energy and half the energy difference between the $^1\Sigma_g^+$ singlet and $^3\Sigma_u^+$ triplet Born-Oppenheimer potentials which comprise all the Coulomb interaction between the electrons and nuclei. For two interacting neutral atoms in their ground state, all the permanent electric multipoles are absent. The long range dispersion forces between them are governed by the attractive induced-dipole-induced-dipole van der Waals interaction [Jon06]. The van der Waals interaction scales as $-\frac{C_6}{R^6}$, where C_6 is the van der Waals coefficient. Weaker higher order contributions scale as R^{-8} , R^{-10} , ... Note that the van der Waals interaction

is only dependent on the distance between the two particles but not on the spin. In the case of two colliding alkali atoms, the single unpaired or valence electron determines the interaction. When the distance between the colliding atoms gets small enough for the electronic wave functions to overlap, the exchange energy starts to significantly contribute to the interaction. This interaction arises from wave function overlap and depends on electronic spin. The electronic spins s_a and s_b of the individual atoms a and b couple to a total spin $S = s_a + s_b$ with the associated quantum number $S = 0$ or $S = 1$. States with $S = 0$ are called *singlet* states and states with $S = 1$ are called *triplet* states. The van der Waals coefficient C_6 is the same for the singlet and the triplet interaction potentials, therefore these are degenerate at large separation. At smaller separation, in the region of conventional chemical bonding, the two potentials become distinct due to the increasing contribution from the exchange energy which is attractive for the singlet state and repulsive for the triplet state, see figure 2.4.

In the region of large internuclear separation, the hyperfine splitting of the atoms is

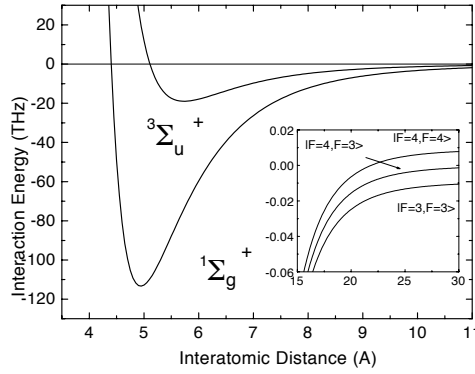


Figure 2.4: Cs interaction potentials: Singlet $X^1\Sigma_g^+$ and triplet $a^3\Sigma_u^+$ interaction potentials for two colliding Cs atoms. At large internuclear separation, the energy structure is dominated by the hyperfine interaction as shown in the inset. Note the different energy scales. The complete labeling of the molecular states is discussed in section 3.1.1. Figure adapted from [Chi01].

larger than the splitting between singlet and triplet states and than the thermal energy of the colliding atoms in the ultracold limit. Therefore, three different scattering continua have to be considered, each separated by the ground state hyperfine splitting of the Cs atom. At zero magnetic field, they can be labeled by the total atomic angular momentum quantum numbers F , where $F = i + j$ is the sum of the nuclear spin i and the total electronic angular momentum j . For alkali atoms in their electronic ground state $j = s$ and therefore $F = i + s$. In Cs, nuclear spin is $7/2$ and the total angular momentum can take on the values $F = 3$ or $F = 4$ and therefore, these thresholds are labeled $|F = 3, F = 3\rangle$, $|F = 4, F = 3\rangle$, and $|F = 4, F = 4\rangle$ as indicated in the inset in figure 2.4. Each of these curves has unresolved degeneracies that can be labeled by the quantum number f , where $f = F_a + F_b$ [Jon06].

In contrast to the lighter alkali species, the cesium atom is peculiar in that not only the van der Waals and the exchange interactions play an important role but also the weaker relativistic interactions H_{rel} . These are the magnetic dipole-dipole and second order spin-orbit interactions that stem from spin-spin interactions between the two atoms. The second order spin-orbit interaction is synonymous with the indirect spin-spin coupling. Together with the atomic hyperfine structure, this is crucial for understanding the characteristic scattering properties of cesium and the molecular structure of weakly bound Cs molecules [Chi04b].

2.2.2 Two-body Scattering

When two atoms a and b in quantum states $|\alpha_a\rangle$ and $|\alpha_b\rangle$, where α denotes all relevant quantum numbers, collide and end up in quantum states $|\alpha'_a\rangle$ and $|\alpha'_b\rangle$, then an interaction is termed *elastic* if the resulting states $|\alpha'_i\rangle$ are identical to the initial states $|\alpha_i\rangle$, ($i = a, b$). No exchange of energy between inner degrees of freedom and translational degrees of freedom takes place. Elastic collisions lead to the thermalization of an ensemble of particles and are therefore crucial for the thermalization during evaporative cooling on the way to Bose-Einstein condensation. Thus the term “good” collisions has been coined. In contrast, *inelastic* collisions are those where the internal states of the colliding particles change, $|\alpha'_i\rangle \neq |\alpha_i\rangle$. Two atoms or molecules that are not in their absolute internal ground state can collide and release energy that is distributed to the translational motion of the collision partners. This process can heat the sample if the products are trapped. Alternatively, it leads to particle loss because the resultant states are not trappable or because the kinetic energy is higher than the trap depth.

The atomic scales of length, time, and spectral line width in the ultracold regime are in sharp contrast to the usual relations valid for scattering at room temperature. At room temperature, the thermal de Broglie wavelength λ_{dB} is on the order of a few thousandth of a nanometer and gas phase chemical reactions can usually be interpreted as the interaction of classical nuclear point particles moving along potential surfaces defined by their associated electronic charge distributions [Wei99]. Due to the high kinetic energy of the particles, the interaction time is short. In contrast, in the ultracold regime, the de Broglie wavelength is several hundred times typical molecular bond lengths and the collisional interaction time is several times the spontaneous emission lifetime of an atom. The inhomogeneous Doppler width is smaller than the natural linewidth of atomic dipole transitions, which enables high precision free-bound and bound-bound spectroscopy. In addition, if an external field is applied, all atoms in an ensemble are coupled to it, instead of only a certain velocity class that fulfills the resonance condition. As will be illustrated below, the quantum state of the collision partners can be precisely controlled and therefore, matter wave effects can be studied. The long collision durations aid in controlling the outcome of a collision by external fields.

The ground state hyperfine splitting, which is 9.192631770 GHz in Cs, is orders of magnitude larger than the translational energy of the colliding atoms. Therefore, the hyperfine structure provides well defined scattering channels as illustrated in figure 2.4. When collisional resonances as discussed in section 2.2.3 occur, the scattering state couples only to one or very few bound states. Similarly, the outgoing channels are well defined and only one or a few channels typically have to be considered.

As a consequence, ultracold scattering processes are traceable and amenable to detailed theoretical analysis that reveals the underlying molecular structure. In this sense, they lie at the interface between atomic and molecular physics. Ultracold scattering experiments allow for extremely precise testing of the theoretical models for interparticle interaction that contain no adjustable parameters [Bur02]. Such threshold-resonance spectroscopy can be done with high precision considering the very small spread introduced by thermal effects. A temperature of 1 μK yields a thermal energy spread of $\frac{k_B T}{h} = 21$ kHz, where $k_B = 1.3806505 \times 10^{-23}$ J K⁻¹ is the Boltzmann constant.

On the scale of these ultralow collision energies, the interaction potential for two scattering particles already has a significant impact on the scattering wave function at distances much larger than the classical extension of the interaction potential. Therefore, ultracold scattering experiments are sensitive to the asymptotic region of the potential which is hardly accessible to conventional spectroscopy. Note, however, that the group of Tiemann has obtained spectroscopic data starting from tightly bound ground state molecules [Sam00] that is very competitive with data obtained from ultracold collision experiments involving photoassociation.

The quantum mechanical treatment of ultracold scattering processes is greatly facilitated by introducing a partial wave decomposition of the stationary scattering wave function of the relative motion of the atom pair. A general introduction to quantum mechanical scattering is given in the book by Cohen-Tannoudji, Diu, and Laloë [CT99], its application to ultracold scattering processes is discussed in reference [Wei99]. The partial wave method decomposes the scattering wave function according to the quantum numbers ℓ and m_ℓ . The angular momentum of relative motion between the two colliding atoms is given by ℓ , whereas its orientation with respect to a laboratory fixed axis defined by the magnetic field axis is given by m_ℓ .

The partial waves are termed *s*, *p*, *d*... partial waves for $\ell = 0, 1, 2, \dots$. Partial waves with angular momentum $\ell \neq 0$ experience an effective repulsive potential barrier that has to be overcome for scattering to occur. In the ultracold regime, the kinetic energy of the particles is not sufficient to overcome this barrier for partial waves with $\ell > 0$. The classical turning points for this centrifugal barrier are located at large interatomic distances R . Therefore, scattering is effectively reduced to *s-wave scattering*, resulting in an isotropic process.

When dealing with scattering among identical atomic species, the scattering wave function has to be symmetrized with respect to exchange of identical particles [Wei99]. In general, if two atoms a and b of the same species in identical quantum states $|\alpha_a\rangle = |\alpha_b\rangle$ collide, only either even or odd partial waves can contribute to collision

2 Ultracold Quantum Gases

rates depending on whether the atoms are composite bosons or composite fermions. For the case of composite bosons, only even partial waves occur whereas for the case of composite fermions, only odd partial waves are possible. If the two quantum states are not identical, both even and odd partial waves are possible. ^{133}Cs is a composite boson and therefore only even partial waves can contribute to scattering, as will be seen in section 3.2.3.

Elastic Scattering

In elastic s -wave scattering the effect of the scattering process reduces to a mere phase shift δ_0 between the incoming wave and the outgoing wave for values of the interatomic separation R much larger than the typical length scale of the interaction potential. For a van der Waals potential, this length scale is set by the van der Waals length l_{vdW} which is connected to the C_6 coefficient by

$$l_{vdW} = \frac{1}{2}(mC_6/\hbar^2)^{1/4}, \quad (2.8)$$

where m is twice the reduced mass of the atom pair which in the case of identical particles coincides with the mass of a single atom [Koh06]. For Cs the van der Waals length is on the order of $100 a_0$.

In the interaction region the wave function oscillates rapidly due to the interaction potential. The behavior of the wave function in the interaction region depends crucially on the precise shape of the interaction potential. Therefore, also the phase shift imparted by the scattering process is crucially dependent on the exact shape of the potential.

In the ultralow energy limit, as the scattering wave vector k goes to zero the following relation for the phase shift δ_0 converges to a constant value a that has the dimension of a length:

$$-\lim_{k \rightarrow 0} \frac{\tan \delta_0(k)}{k} = a \quad (2.9)$$

The entity a is a characteristic quantity for the particular scattering process and contains the information about the phase shift experienced by the scattering wave function. It is called the *elastic s -wave scattering length* and has a direct connection to the scattering cross section σ and a wealth of other phenomena in ultracold collision physics. The scattering length has a very intuitive interpretation given e.g. in reference [Bur02]. When extrapolating the unperturbed long-range scattered wave to small R , one obtains a node at $R = a$ which is independent of the collision energy, provided that the collision energy is small. In the case of negative scattering length this corresponds to a virtual node. This interpretation emphasizes the relation between the scattering length and the scattering phase shift δ_0 . It should be noted that just as the phase shift δ_0 depends on the precise characteristics of the interaction potential, the scattering length is exquisitely dependent on the precise interaction between the particles. The singlet

and triplet potentials can be assigned their respective scattering lengths a_S and a_T . For $a = 0$ the incoming and outgoing wave functions interfere destructively and therefore no s -wave interaction can take place. This is called the Ramsauer-Townsend effect.

The scattering length is closely related to the location of the last bound state of the interaction potential. If the last bound state is located just below the zero energy threshold, the scattering length is large and positive. If the potential is just not deep enough to support another bound state, the scattering length is large and negative. If the last bound state exactly coincides with the zero energy threshold, the scattering length diverges. This is called a *zero energy resonance*. Positive scattering length corresponds to repulsive interaction, negative scattering length corresponds to attractive interaction.

In the zero energy limit the elastic scattering cross section σ_{el} for the scattering of identical bosonic atoms is given by

$$\sigma_{el} = 8\pi a^2. \quad (2.10)$$

This elastic cross section can be much larger than the cross section at room temperature [Bur02]. This is crucial for evaporative cooling to quantum degeneracy. It vanishes identically for fermions in identical spin states because s -wave scattering is forbidden. For nonzero collision energies that are still in the s -wave scattering regime, the elastic cross section for large values of a is

$$\sigma_{el} = \frac{8\pi a^2}{1 + k^2 a^2}. \quad (2.11)$$

For $k^2 a^2 \ll 1$ the zero energy limit is recovered, for $k^2 a^2 \gg 1$ this expression reduces to

$$\sigma_{el} = \frac{8\pi}{k^2}, \quad (2.12)$$

which is termed the *unitarity limit*. It sets an upper limit to the elastic cross section for a given collision energy.

As stated before, the scattering length is large and positive when the potential depth is such that a bound state exists just below the zero energy threshold. The binding energy E_b of this last bound state is given by the formula

$$E_b = -\frac{\hbar^2}{ma^2} \quad (2.13)$$

where again m is the mass of a single atom in the case of identical particles. This universal description holds for Feshbach molecules (see section 2.2.3) associated with so-called entrance channel dominated Feshbach resonances [Koh06]. A more accurate description of the binding energy in this case is given by the Gribakin-Flambaum correction [Gri93] introducing the mean scattering length \bar{a} :

$$E_b = -\frac{\hbar^2}{m(a - \bar{a})^2} \quad (2.14)$$

The wave function of such a very loosely bound state “lives” predominantly outside the classical region set by the extent of the interatomic potential, such a state is therefore called a *halo state*. In the region of interatomic distances R large compared to the classical turning point $R_{classical}$, the bound state wave function assumes the general form

$$\phi_b(R) = \frac{1}{\sqrt{2\pi a}} \frac{e^{-R/a}}{R} \quad (2.15)$$

with a mean distance or bond length between the atoms of $a/2$. Note that the characteristic long range of these isotropic diatomic halo molecules is determined by a single parameter of the interaction potential, namely the s -wave scattering length. It is customary to refer to such a situation where physical quantities such as the binding energy and wave function depend only on the scattering length rather than on the details of the interaction itself as the *universal regime* [Koh06]. This universal description holds for halo molecules such as the ^4He dimer as well as highly excited long range Feshbach molecules that we use for our spectroscopic experiments.

The van der Waals length of Cs atoms ($l_{vdW} = 101 a_0$) corresponds to a halo state binding energy of $h \cdot 2.6$ MHz. Description as a halo state is only appropriate for binding energies considerably smaller than this value. The scattering length approximation for Cs is only good for temperatures below $1 \mu\text{K}$.

Inelastic collisions - Spin Changing Collisions

For colliding ground state alkali atoms different scattering channels arise from the hyperfine structure of the individual atoms. If the total energy E_α of a scattering channel, i.e. the sum of the individual atoms' energies $E_{F_a, m_{F_a}}$ and $E_{F_b, m_{F_b}}$ is below the total energy of the system, the channel is said to be *open*. If E_α is above the total energy of the system, the channel is said to be *closed*. This nomenclature is illustrated in figure 2.5.

The van der Waals interaction is not spin-dependent. Therefore, it cannot couple different spin states. The exchange interaction in contrast can induce relaxation of spin states in inelastic collisions. It conserves the angular momentum ℓ of the relative motion between the atoms and its projection m_ℓ and therefore only transitions between states with the same m_f are allowed. Such transitions are suppressed for atoms in stretched states $|F, m_F = \pm F\rangle$.

Contrary to this, the relativistic interactions that are particularly important for the case of Cs atoms allow an exchange of up to two units of angular momentum between internal and external degrees of freedom, and enable inelastic collisions even for stretched states.

The state $|3, -3\rangle$ can be trapped magnetically but inelastic collisional losses prohibited Bose-Einstein condensation of Cs in magnetic traps. In contrast, the $|3, 3\rangle$ state cannot be trapped magnetically but inelastic two-body processes are absent. Therefore, losses

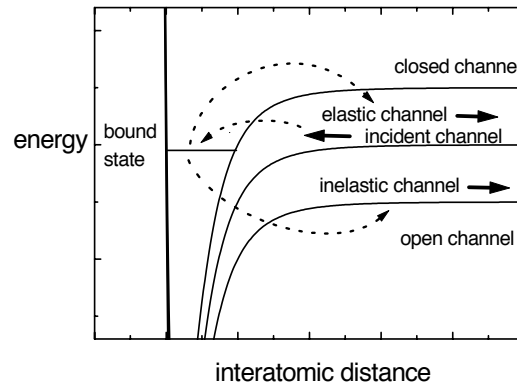


Figure 2.5: Scattering channels and Feshbach resonances: A channel is said to be *elastic* if the internal state of the colliding atoms does not change. An *open* channel has an energy below the total energy of the incident channel, a *closed* channel has higher energy than the incident channel. A *Feshbach resonance* arises when the incident channel couples to a bound state in a closed channel. Figure taken from [Chi01].

are dominated by weaker three-body processes [Web03c] and Bose-Einstein Condensation could be achieved [Web03b].

2.2.3 Feshbach Resonances

In our experiments ultracold molecules are associated from trapped atoms by means of magnetically tunable Feshbach resonances. The following section gives a brief introduction to the physics of Feshbach resonances and the production of Feshbach molecules. The material is taken from the review article by Köhler, Góral and Julienne, where a much more exhaustive discussion can be found [Koh06]. The molecular structure of cesium Feshbach molecules is discussed in more detail in section 3.2.3 in the context of near-threshold molecular states of Cs dimers.

The existence of resonance phenomena in the context of cold atomic gases was first predicted by Stwalley [Stw76]. Magnetically tunable Feshbach resonances were first predicted by Stoof and coworkers [Tie93] and observed experimentally in the group of Ketterle [Ino98]. With Cs, they were first observed by Vuletic and colleagues [Vul99b]. Resonances refer to the energy dependent enhancement of inter-particle cross section due to the existence of a metastable state. This can be a bound state of a subsystem that couples to its environment, which is then referred to as Feshbach resonance, as illustrated in figure 2.5. Shape resonances in contrast arise when a bound state resides behind a potential barrier. The ground state hyperfine splitting provides three well defined scattering potentials that are separated from each other by an energy of $9.2 \text{ GHz}\cdot h$. Each of these potentials supports bound molecular states. The individual molecular states exhibit different magnetic moments. In a two-channel approach [Koh06], the effect of an external magnetic field simply corresponds to a magnetic field

dependent overall shift of the closed channel potential relative to the entrance channel. Therefore the energy of a bound state belonging to a closed channel can be tuned relative to the energy of the scattering state by means of the Zeeman effect. This bound state is referred to as *bare Feshbach state* and labeled “bound state” in figure 2.5.

When the bare Feshbach resonance state is brought into energetic degeneracy with the entrance channel and the scattering atoms are allowed to couple to it, a *Feshbach resonance* occurs. The coupling between the entrance channel and the closed channel leads to a new eigenstate of the coupled system or synonymously to a *dressed state*. These dressed states are the so called *Feshbach molecules*. From an experimental point of view most often the term “Feshbach molecule” is used for any molecule produced by means of a Feshbach resonance, even if it corresponds to the bare Feshbach resonance state. This somewhat sloppy usage is adopted in this thesis.

Coupling can be induced by strong electronic interaction such as the exchange interaction, and by the relativistic interactions introduced in section 2.2.1. The nonrelativistic interactions preserve rotational angular momentum ℓ and consequently lead to *s*-wave Feshbach resonances since scattering in the ultracold regime is reduced to *s*-wave scattering. The relativistic interactions in contrast lead to much weaker coupling of the *s*-wave scattering state to bound molecular states with angular momentum $\ell = 2, 4, \dots$, so called *d*-wave, *g*-wave, . . . states. The Feshbach resonances that arise from coupling of the *s*-wave scattering state to *d*- or *g*-wave molecular states are called *d*-wave and *g*-wave Feshbach resonances, respectively. Near-threshold bound states of Cs_2 will be treated in section 3.2.3. Note that, as already pointed out in section 2.2.2 on page 26, only even partial waves occur for the case of two identical bosonic atoms in identical spin states.

The scattering length as well as the collisional cross section is greatly modified by the presence of a Feshbach resonance, as illustrated in figure 2.6. In the vicinity of a Feshbach resonance the scattering length shows a dependence on magnetic field according to

$$a(B) = a_{bg} \left(1 - \frac{\Delta B}{B - B_0} \right), \quad (2.16)$$

with the off-resonant background scattering length a_{bg} . At the position B_0 of the resonance, the scattering length shows a singularity. This is the magnetic field where the bare Feshbach resonance state is degenerate with the scattering threshold. The width ΔB of the resonance can vary from μG to hundreds of Gauss and is mainly dependent of the magnitude of the coupling between the incident channel and the bound state. The coupling strength is given by the matrix element between the bare Feshbach resonance state ϕ_{res} and the entrance channel wave function ϕ_0^+ with the coupling operator W according to

$$\Delta B = \frac{m(2\pi\hbar)^3}{4\pi\hbar^2 a_{bg} \mu_{res}} \left| \langle \phi_{res} | W | \phi_0^+ \rangle \right|^2 \quad (2.17)$$

As already pointed out, the relativistic interactions in cesium can weakly couple states of different relative angular momentum ℓ and lead to narrow higher order Feshbach res-

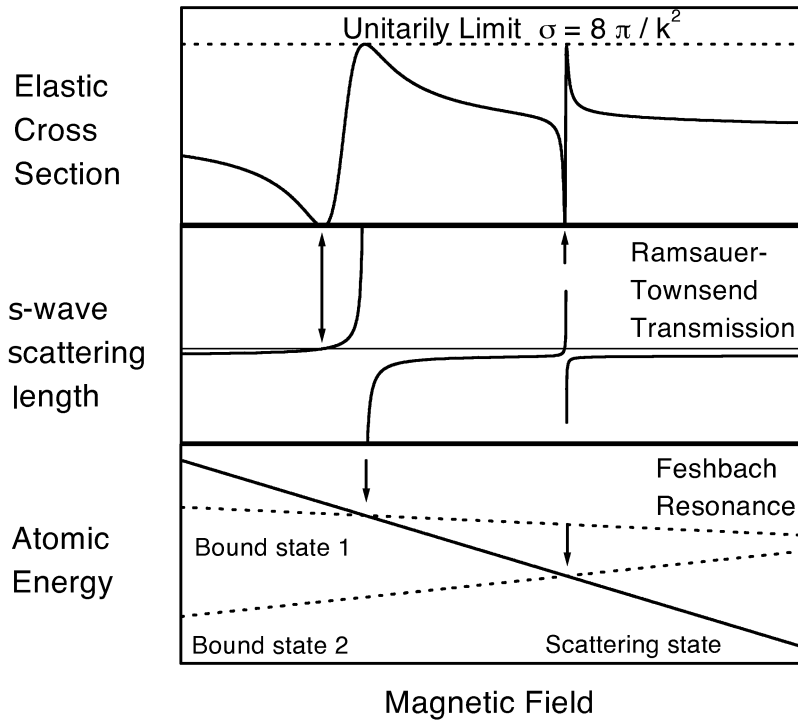


Figure 2.6: Elastic scattering cross section and scattering length near Feshbach resonances: Different bound states and the scattering state differ in magnetic moment. Therefore, their energies vary differently with the magnetic field due to the Zeeman effect. At the intersection of bound states with the scattering state, Feshbach resonances appear (arrows in lowest panel). The s -wave scattering length varies dispersively in the region of the resonance. Where the s -wave scattering length is zero, the elastic cross section goes to zero. This is the Ramsauer-Townsend effect. When the scattering length becomes very large, the elastic scattering cross section reaches its maximum value which is the unitarity limit, as discussed in section 2.2.2. Note the different width in magnetic field of the two displayed Feshbach resonances. The width is determined by the coupling strength and the difference in magnetic moments between the bound state and the scattering state. (Picture taken from [Chi01]).

onances. The above relation further depends on the difference μ_{res} in magnetic moment between the scattering state and the bare Feshbach resonance state, which is typically on the order of one Bohr magneton μ_B in Cs. Figure 2.6 shows this behavior as two different molecular states intersect the scattering threshold and produce Feshbach resonances of different widths. Also shown is the variation of the elastic scattering cross section as discussed in section 2.2.2.

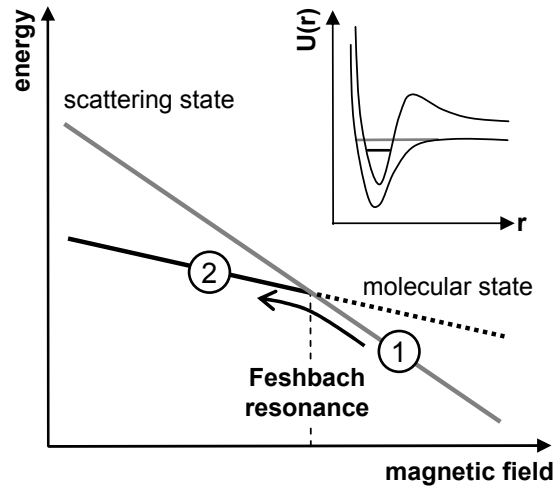


Figure 2.7: Molecule production at a Feshbach resonance: Zeeman diagram for the atomic scattering state and the molecular bound state. The Feshbach resonance corresponds to the crossing point of the atomic scattering state and a molecular state. Molecules at (2) are created from the atomic cloud at (1) by a downward sweep of the magnetic field across the resonance. The inset shows the configuration (2) where the molecular state is below the scattering continuum.

Formation of Feshbach Molecules

The formation of Feshbach molecules is illustrated in figure 2.7. The energies of the scattering state and a molecular state differ in their magnetic field dependence and intersect at a certain position. This is the position of the Feshbach resonance. For molecule formation, the magnetic field is set to a value above the resonance (1) and then the magnetic field is ramped adiabatically over the resonance to (2). This corresponds to bringing the bare Feshbach resonance state from above the scattering threshold into degeneracy with the scattering state and then further down corresponding to a bound state in (2). The inset shows the entrance channel and the closed channel with its associated Feshbach state at position (2) after the sweep. Here, the Feshbach state corresponds to a weakly bound molecular state.

Atom-molecule coherence was first demonstrated by Wieman and coworkers [Don02] applying time-dependent magnetic field variations around a zero-energy resonance of ^{85}Rb . Production of ultracold molecules by magnetic field sweeps from Bose-Einstein condensates was achieved in several groups soon thereafter [Her03, Dür04, Xu03]. In two-component spin mixtures of fermionic atoms, the same technique was applied successfully [Cub03, Joc03b, Reg03, Str03]. Figure 2.2.3 shows a cloud of ultracold Cs_2 molecules formed in this way and coupled out of an atomic sample by a Stern-Gerlach type technique [Her03]. The Stern-Gerlach separation by means of a magnetic field gradient is due to the different magnetic moments of the atomic and the molecular state.

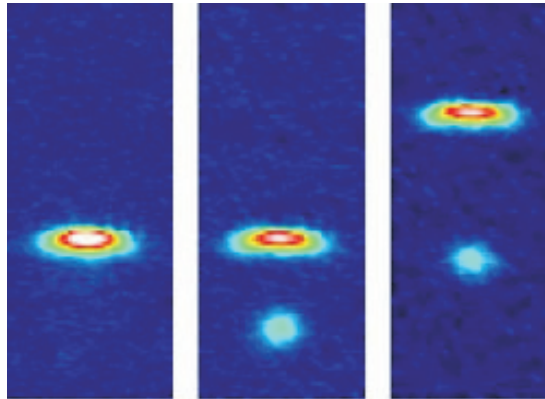


Figure 2.8: Ultracold quantum gas of Cs molecules: *left:* Absorption picture of an atomic cloud after release from the trap. The atoms are levitated by a magnetic field gradient. *middle:* Association of atoms by means of a magnetic field sweep across a Feshbach resonance. Ultracold Feshbach molecules appear as a separate cloud when the levitation gradient is adjusted to levitate the atoms. *right:* When the levitation field is adjusted for the molecules, the atoms are accelerated upwards. Figure taken from [Her03].

2.3 Bose Einstein Condensation

We are working on the production of a Bose-Einstein condensate (BEC) of molecules in their absolute internal ground state. In order to reach the phase space density necessary for the condensation of molecules it is necessary to (i) start from a sufficiently cold and dense atomic sample, (ii) efficiently produce Feshbach molecules, and (iii) efficiently transfer the molecules to their rovibrational ground state. The efficiency of Feshbach molecule production is greatly increased in an atomic BEC. For transfer to the rovibrational ground state, an optical lattice provides the necessary shielding from detrimental collisional losses. Loading of the optical lattice and preparation of exactly two atoms per lattice site for Feshbach molecule production is preferentially from an atomic BEC. In conclusion, it is advantageous to use an atomic BEC as starting point in the quest for a molecular ground state BEC. Here the basic physics of Bose-Einstein condensation is discussed, which lays the groundwork for the understanding of both atomic and molecular BECs. This section is intended as a primer for readers unfamiliar with the physics of Bose-Einstein condensation. A much more exhaustive treatment of the topic can be found in a series of review articles and dedicated books [Ket99, Cor02, Ket02, Cor99, Dal99, Pet02, Pit03].

Bose-Einstein condensation is possible for bosonic particles and can be defined as the macroscopic occupancy of the system's lowest single-particle quantum state. The onset of Bose-Einstein condensation is heralded by a distinct phase transition. The term

2 Ultracold Quantum Gases

macroscopic here states that *many* particles occupy the same state. The phenomenon of Bose-Einstein condensation was first predicted in 1925 by Einstein [Ein25] based on work by Bose on photon statistics [Bos24]. Experimentally, liquid helium was for a long time the only system where the phenomenon of Bose-Einstein condensation could be studied, at least in the regime of strong particle interactions. The possibility to study Bose-Einstein condensation of noninteracting particles, i.e. of an ideal gas, or of weakly interacting particles had to await the development of laser cooling and trapping techniques in the 1980s and the implementation of the evaporative cooling technique [Ket96]. Bose-Einstein condensation was first realized experimentally in 1995 by E. Cornell, C. Wieman and collaborators [And95] in a dilute gas of ^{87}Rb . Soon, other alkali species [Dav95, Bra95, Bra97, Fri98, Cor00, Mod01] and several non-alkali species followed. Although Cs was initially thought to be a good candidate for Bose-Einstein condensation, condensation was prohibited in magnetically trapped samples due to unexpectedly large two-body losses. Bose-Einstein condensation of Cs was first achieved by our group [Web03b] by adopting an optical trapping approach instead of magnetically trapping the sample.

In 2003, it became possible to Bose-Einstein condense Feshbach molecules composed of two fermionic atoms [Joc03a, Gre03]. These are much more stable against inelastic collisions than molecules composed of bosonic atoms. The Bose-Einstein condensation of Feshbach molecules composed of bosonic atoms has been hindered hitherto by the presence of inelastic loss channels due to dimer-dimer collisions.

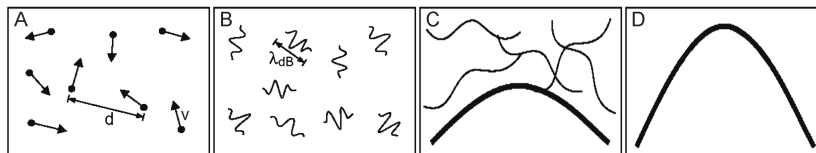


Figure 2.9: Bose-Einstein condensation: The sequence *A – D* illustrates the transition from a classical gas at high temperature to a Bose-Einstein condensate. *A*: In a classical gas, particles can be considered point-like entities moving at high velocities with the mean distance d between the particles being much larger than the extent of the individual particle. *B*: At smaller temperatures, the thermal de Broglie wavelength λ_{dB} of the particles increases and the quantum mechanical wave nature of the particles starts to play a role. *C*: The phase transition to a Bose-Einstein condensate occurs when the wave functions of the individual particles start to overlap, i.e. when the de Broglie wavelength becomes comparable to the distance between the particles $\lambda_{dB} \sim d \sim n^{-1/3}$. *D*: At zero temperature, the system can be described by a single macroscopic wave function and the condensate is pure with no thermal particles remaining. Figure adapted from [Ket99].

Figure 2.9 gives a very intuitive illustration of the phenomenon of Bose-Einstein condensation. At room temperature, atoms in a gas can effectively be regarded as point-like particles moving at high velocity. The extent of the particles is much smaller than the mean interparticle distance d which is proportional to $n^{-1/3}$, where n is the

number density. The quantum mechanical wave nature of the atoms or molecules can be neglected. At lower temperatures, the atoms move more slowly and accordingly, the thermal de Broglie wavelength $\lambda_{dB} = \sqrt{2\pi\hbar^2/(mk_B T)}$ increases. Here m is the atom's mass, \hbar is Planck's constant divided by 2π and k_B is the Boltzmann constant. The de Broglie wavelength gives a measure of the spatial extent of the wave packet associated with the particles. Its increasing magnitude indicates that the quantum mechanical wave nature of the atoms start to play a role. When the individual wave packets start to overlap, the phase transition to Bose-Einstein condensation ensues and the particles start to form a macroscopic matter wave. The wave packet overlap can be measured by the so called *phase space density* ρ defined by

$$\rho = n\lambda_{dB}^3, \quad (2.18)$$

where n is the density of particles. When $\rho \geq 1$, wave packets start to overlap. At the same time the sample is cooled, it must be assured that the usual transition from gaseous to liquid to solid is prevented by diluteness of the sample. Diluteness is assured by the condition

$$n|a^3| \ll 1, \quad (2.19)$$

where a is the s -wave scattering length which is the single most important parameter describing particle interactions in the ultracold regime as discussed in section 2.2.2. The scattering length is thus of fundamental importance for the physics of Bose-Einstein condensation.

Typical values for the scattering length are around 100 Bohr radii and densities are $n \approx 10^{13} - 10^{15}$ particles/cm³ with temperatures below 1 μ K. Therefore, both the diluteness requirement and the condition for wave function overlap can be met simultaneously.

2.3.1 Bose-Einstein Condensation in the Non-interacting Gas

The phenomenon of Bose-Einstein condensation can be inferred from purely quantum statistical considerations without taking particle interactions into account. This gives a fairly good estimate for the temperature at which condensation takes place and the fraction of particles in the condensate. In contrast, to derive the energy and shape of a condensate, one has to resort to a treatment including particle interactions as will be done in section 2.3.2.

Quantum gases obey different statistics depending on whether the particles involved are bosons or fermions. For the bosonic case, the mean occupation number of a single particle state ν with energy ε_ν is given by the Bose distribution function

$$N_\nu = \frac{1}{e^{\frac{\varepsilon_\nu - \mu}{k_B T}} - 1}. \quad (2.20)$$

The energy of the individual single-particle states ε_ν is determined by the trapping potential that confines the gas, whereas the chemical potential μ assures the normalization

2 Ultracold Quantum Gases

to the total particle number N via the relation

$$N = \sum_{v=0}^{\infty} N_v. \quad (2.21)$$

For a room temperature gas, the single-state occupancy is much less than one for any given state and in particular for the ground state ε_0 . This implies that the chemical potential μ is much smaller than the ground state energy ε_0 . When the temperature is lowered and the particle number N is kept constant, μ increases in order to ensure that equation 2.21 is fulfilled. However, the chemical potential cannot increase beyond the ground state energy ε_0 because this would imply diverging or negative occupancy of the ground state. At the onset of Bose-Einstein condensation, the ground state ε_0 starts to be populated macroscopically by a large number of particles. It is convenient to treat the number of particles N_{ex} that occupy states $v > 0$ other than the ground state separately. Taking the upper limit for the chemical potential into account, one immediately sees that the maximum number of particles outside the ground state is given by

$$N_{ex,max} = \sum_{v=1}^{\infty} \frac{1}{e^{\frac{\varepsilon_v - \varepsilon_0}{k_B T}} - 1}. \quad (2.22)$$

By necessity then, if $N_{ex,max}$ is smaller than the total number of particles N in the system, the particles that cannot be accommodated in the excited states must be residing in the ground state. This marks the onset of the condensation process. The temperature at which $N_{ex,max}$ becomes smaller than the total particle number N is called the critical temperature T_c . It usually corresponds to energies $k_B T_c$ much greater than the energy difference between the ground and first excited state in the trapping potential. The number of particles in the ground state N_0 can grow to N as μ approaches ε_0 when the temperature is lowered.

In statistical physics, the sum over the states in equation 2.22 is replaced by an integration over the density of states. It turns out that the phase space density ρ introduced above is the most convenient parameter to experimentally monitor the progression towards condensation. First, it can easily be calculated from quantities measured in the experiment and secondly Bose-Einstein condensation sets in at a well-defined value of ρ . Evaluating the case of a three dimensional harmonic oscillator trapping potential $U(\mathbf{r}) = \frac{m}{2}(\omega_x^2 x^2 + \omega_y^2 y^2 + \omega_z^2 z^2)$, the relation for the phase space density reads

$$\rho = N \left(\frac{\hbar \bar{\omega}}{k_B T} \right)^3, \quad (2.23)$$

where $\bar{\omega}$ is the geometrically averaged trap frequency $\bar{\omega} = \sqrt[3]{\omega_x \omega_y \omega_z}$. For the case of a three-dimensional harmonic oscillator potential, Bose-Einstein condensation sets in when the phase space density reaches a value of

$$\rho = 1.202. \quad (2.24)$$

In the case of a non-interacting, i.e. an ideal Bose-Einstein condensed gas in a harmonic oscillator potential, the condensate wave function $\phi(\mathbf{r})$ takes on the shape of the harmonic oscillator ground state wave function which is a gaussian distribution

$$\phi(\mathbf{r}) = \left(\frac{m\bar{\omega}}{\pi\hbar}\right)^{3/4} \exp\left(-\frac{m}{2\hbar}(\omega_x x^2 + \omega_y y^2 + \omega_z z^2)\right). \quad (2.25)$$

2.3.2 Bose-Einstein Condensation in Weakly Interacting Gases

Real gases exhibit interactions which greatly modify the wave function of the condensate. In addition, evaporative cooling in the final stage of BEC production depends on rapid thermalization of the sample mediated by elastic collisions. Evaporative cooling preferentially removes the hottest particles in the sample. Each lost particle therefore carries away more than the average energy per particle, therefore cooling the sample. The particle loss is overcompensated by the reduction of the energy in the system and thus the phase space density increases.

The Gross-Pitaevskii Equation

To derive the properties of a weakly interacting Bose-Einstein condensate, one could write down the many-body Hamiltonian in second order quantization and solve it numerically. An alternative approach is to treat the interactions as a mean-field effect, which can be conveniently done in the dilute limit where $n|a|^3 \ll 1$. One decomposes the boson field operator $\hat{\Psi}$ that describes the production and annihilation of particles according to

$$\hat{\Psi}(\mathbf{r}, t) = \Phi(\mathbf{r}, t) + \hat{\Psi}'(\mathbf{r}, t), \quad (2.26)$$

with the complex expectation value of the boson field operator $\Phi(\mathbf{r}, t) \equiv \langle \hat{\Psi}(\mathbf{r}, t) \rangle$ and a first order perturbation term $\hat{\Psi}'(\mathbf{r}, t)$ that is usually neglected for ultralow temperatures since it represents excitations. $\Phi(\mathbf{r}, t)$ is related to the condensate density via $n(\mathbf{r}, t) = |\Phi(\mathbf{r}, t)|^2$ and is called condensate wave function or ‘‘order parameter’’. In this approximation, the many-particle Schrödinger equation becomes the Gross-Pitaevskii equation

$$i\hbar \frac{\partial}{\partial t} \Phi(\mathbf{r}, t) = \left(-\frac{\hbar^2 \nabla^2}{2m} + U(\mathbf{r}) + g|\Phi(\mathbf{r}, t)|^2 \right) \Phi(\mathbf{r}, t). \quad (2.27)$$

The cardinal feature of this equation is the non-linear term $g|\Phi(\mathbf{r}, t)|^2$ which constitutes the mean field interaction term. The coupling constant

$$g = \frac{4\pi\hbar^2 a}{m} \quad (2.28)$$

accounts for the magnitude of the interaction by its dependence on the s -wave scattering length a . The Gross Pitaevskii equation can be used to describe collective excitations, soliton propagation and vortex formation.

2 Ultracold Quantum Gases

With the ansatz $\Phi(\mathbf{r}, t) = \phi(\mathbf{r}) \exp(-i\mu t/\hbar)$ one obtains the stationary Gross-Pitaevskii equation

$$\left(-\frac{\hbar^2 \nabla^2}{2m} + U(\mathbf{r}) + g|\phi(\mathbf{r})|^2 \right) \phi(\mathbf{r}) = \mu\phi(\mathbf{r}), \quad (2.29)$$

where μ is the chemical potential.

The Thomas-Fermi Regime

The confinement by the trapping potential imparts a momentum uncertainty on the condensate via the Heisenberg uncertainty principle. In the limit where the kinetic energy of the condensate is negligible with respect to the interaction energy, which is called the *Thomas-Fermi regime*, the stationary Gross-Pitaevskii relation reduces to

$$\mu = U(\mathbf{r}) + g n(\mathbf{r}). \quad (2.30)$$

The density of the condensate is zero where $\mu < U(\mathbf{r})$ and

$$n(\mathbf{r}) = \frac{\mu - U(\mathbf{r})}{g} \quad (2.31)$$

for $\mu > U(\mathbf{r})$. Note that this is *not* a Gaussian distribution but instead, for the case of a harmonic oscillator trapping potential, represents an inverted parabola. The BEC also shows this shape during expansion after release from the trap distinguishing it from the thermal background that shows a Gaussian shape. This has been used widely as a direct indicator for Bose-Einstein condensation.

CHAPTER 3

Molecular Structure

This chapter is intended to acquaint the reader with some basic concepts needed to understand the molecular structure of Cs dimers. For us, this understanding is instrumental in the quantum mechanical control of ultracold cesium molecules.

A series of different techniques have been employed in the study of Cs molecules. “Classical” laser and Fourier transform spectroscopy is most suited to study tightly bound vibrational states both in the electronic ground and excited states [Wei85, Ver87, Ami88b, Ami88a, Ami02]. A substantial improvement in the study of long range interaction and loosely bound molecules came with the advent of photoassociation spectroscopy [Fio98, Tak98, Fio99, Com00, Van04, Wes04, Kra05]. The technique of Feshbach spectroscopy has unveiled the detailed energy structure of molecular states right at the dissociation threshold [Vul99b, Vul99a, Chi00, Leo00, Chi04a].

The experiments with ultracold molecules performed in our group so far have been concerned with a regime where the molecules can essentially be seen as a pair of largely unperturbed atoms that are separated by distances much larger than the length scale of typical chemical bonds. With the current spectroscopic experiments we are addressing tightly bound rovibrational states in the electronically excited state. This corresponds to a region of tight chemical bonding where the molecular character is much more important and a description in terms of individual atoms is not adequate any longer. In this respect, the spectroscopic experiments broaden the scope of our experiments because we simultaneously address both the regime of Feshbach molecules that can be seen as a pair of atoms and the regime of tight molecular binding. In order to discuss which molecular electronically excited states can be accessed from the Feshbach molecules and what transition rates to expect, a background on the structure of diatomic molecules and their symmetries has to be given. Molecular symmetries are closely linked to the selection rules for optical transitions. In the region addressed by the 1.55 μm spectroscopy laser, we are primarily dealing with excited state potentials of 0_u^+ symmetry that arise from the Born-Oppenheimer potentials discussed in the next section through spin-orbit coupling. The energy structure of the 0_u^+ potentials is perturbed in the whole range of binding energies by the phenomenon of resonant coupling, as will be discussed below.

We are planning to implement a scheme of coherent population transfer from the Feshbach states to the rovibrational ground state of the $X^1\Sigma_g^+$ electronic ground state via an intermediate electronically excited state in order to stabilize the molecules against inelastic molecule-molecule collisions. This is required for the formation of a ground

state molecular Bose-Einstein condensate. The choice of intermediate state depends on dipole selection rules and expected transition rates between the Feshbach state and the intermediate state on the one side and the intermediate state and the rovibrational ground state on the other side. There is a series of possible routes for such a transfer. We are currently evaluating the possibility to drive a two-photon process with very large detunings of the intermediate state with respect to its potential asymptote. The second step in this transfer process, i.e. between the intermediate state and the rovibrational ground state of the molecule has been evaluated by classical spectroscopic experiments with the difference that these experiments were mainly dealing with rotationally highly excited levels. What we are currently implementing is the first step of this transfer process which has not been addressed experimentally in the regime of very large detunings from the excited state asymptote. In order to evaluate this scheme and alternative schemes based for example on more than one two-photon transitions or on different intermediate electronic states and detunings from the potential asymptote, knowledge of the relevant molecular symmetries, coupling between molecular excited states by the spin-orbit interaction and the properties of Feshbach molecules is required. The relevant theoretical aspects are discussed below whereas different transfer schemes are discussed in section 6.2.

The chapter is organized as follows. First, a review of molecular theory with emphasis on the homonuclear dimers will be given in section 3.1. An overview of molecular states, their labeling and properties is given in section 3.1.1. The production of ultracold molecules has been discussed in the previous chapter. Here, the particular properties of the Cs dimer, both in the electronic ground state and the first electronically excited states are treated in section 3.2. This chapter includes a discussion of the properties of Cs Feshbach molecules in section 3.2.3. Optical transitions are discussed in section 3.3. The important Franck-Condon principle (section 3.3.1) and the relevant selection rules (section 3.3.2) lay the groundwork for the discussion of optical transitions between Feshbach states and electronically excited states in the wavelength region of interest for the current spectroscopic experiments in section 3.3.3.

3.1 Theory of Diatomic Molecules

This section gives an overview of the structure of diatomic molecules. In order to understand diatomic molecules, one has to understand the nature of the binding between the two constituent atoms and how the properties of the individual atoms translate into properties of the molecule. In the bound molecule, the nuclei are separated by some equilibrium distance R_e around which the nuclei can exert vibrational motion. Due to the large mass of the nuclei in comparison to the electrons, the motion of the nuclei is much slower than the motion of the electrons. This feature is exploited in the Born-Oppenheimer approximation and will lead to the concept of potential curves. The rotation of the molecule as a whole about an axis perpendicular to the internu-

clear connection is an additional degree of freedom that modifies the energy spectrum. In addition, molecular states are characterized by the way the electronic spins of the constituent atoms add up whereas nuclear spin has an important role for symmetry considerations. It will be necessary to explore which quantities are “good” quantum numbers, meaning that they are conserved. All these topics will be discussed very briefly here, a much more exhaustive coverage can be found in textbooks on molecular physics, for example the book by Demtröder [Dem05] and the book by Lefebvre-Brion and Fields [LB04]. A very compact and practical introduction to the most relevant aspects of molecular theory is given in the book by Hill and Lee [Hil07]. The discussion here mainly follows this latter reference.

3.1.1 The Born-Oppenheimer Approximation

A diatomic molecule can, in simplest approximation, be seen as two heavy masses in close proximity connected by a massless spring. The nuclei can vibrate and at the same time rotate about an axis that contains the center of mass perpendicular to the internuclear line. The possibility of vibrating and rotating at the same time implies that these two movements are not completely independent of each other. With respect to the electronic motion, the radial symmetry of single atoms is broken by the presence of the second atom.

The general Hamiltonian in the center-of-mass coordinates takes on the form

$$\hat{H} = -\frac{\hbar^2}{2\mu}\nabla^2 - \frac{\hbar^2}{2m_e}\sum_{i=1}^N\nabla_i^2 + V(\mathbf{r}_i; \mathbf{R}_1, \mathbf{R}_2) + \zeta. \quad (3.1)$$

The nabla operator ∇ acts on the nuclear separation R , μ is the nuclear reduced mass $M_1M_2/(M_1 + M_2)$, m_e is the electronic mass, the sum is over all electrons and ∇_i acts on the electronic coordinates. $V(\mathbf{r}_i; \mathbf{R}_1, \mathbf{R}_2)$ comprises the electrostatic repulsion between the two nuclei and the repulsion between individual electrons and the attraction between electrons and nuclei. ζ represents smaller relativistic terms such as spin-spin and spin-orbit interactions. These are very important for understanding the structure of Cs Feshbach molecules as discussed in section 3.2.3. Neglecting the relativistic interactions will lead to a “nonrelativistic” model of the molecule. The strongest of the relativistic interactions in the molecule is the spin-orbit interaction [Jon06] that will be discussed separately in section 3.1.2. The model developed in this section is based on the notion of a “nonrelativistic atom” and neglects the hyperfine structure and spin-orbit interaction of the atom. Hyperfine structure will be included in the discussion of Feshbach molecules in section 3.2.3.

Theoretical analysis is greatly facilitated if a solution is found that allows to treat the electronic and the nuclear wave functions separately. This is known as the Born-Oppenheimer separation. The overall wave function $\Psi(\mathbf{R}_\alpha, \mathbf{r}_i)$ is written as the product

3 Molecular Structure

of the electronic wave function $\psi_{el}(\mathbf{R}_\alpha, \mathbf{r}_i)$ and the nuclear wave function $\psi_N(\mathbf{R}_\alpha)$

$$\Psi(\mathbf{R}_\alpha, \mathbf{r}_i) = \psi_{el}(\mathbf{R}_\alpha, \mathbf{r}_i) \cdot \psi_N(\mathbf{R}_\alpha), \quad (3.2)$$

where $\alpha = 1, 2$. Substituting this ansatz into the Schrödinger equation $\hat{H}\Psi = E\Psi$ one finds that it is possible to separate the Schrödinger equation into an electronic equation and a nuclear equation by neglecting terms that couple the electronic and the nuclear motion. This is the *Born-Oppenheimer approximation* and it is motivated by the fact that nuclear motion happens on a timescale much slower than the electronic motion. This is due to the much larger mass of the nuclei with respect to the electrons. Therefore, when the distance between the nuclei changes during one cycle of nuclear vibration, the electrons can adapt instantaneously to any given value of the internuclear distance. The fact that the electrons move much faster than the nuclei and that the electronic wave functions can adapt instantaneously to any variation of the nuclear configuration is reflected by the term *adiabatic approximation* for the Born-Oppenheimer approach.

The nuclear coordinates enter the electronic equation as fixed parameters. The electronic wave equation can be solved assuming that the internuclear distance R is fixed to yield the energy eigenvalue for each value of R . For each stationary electronic distribution $\psi_{el,n}(r)$, where r represents the electronic coordinates, there is a well defined energy $E_n^{el}(R)$ for any given fixed value of R . The index n emphasizes the fact that these are different for different electronic states.

The *molecular potential energy curves* $U_n(R)$ are the sum of the electrostatic repulsion between the nuclei $V_N = Z_1 Z_2 e^2 / (4\pi\epsilon_0 R)$ and the electronic energies:

$$U_n(R) = V_N(R) + E_n^{el}(R) \quad (3.3)$$

These molecular potential curves enter the nuclear Schrödinger equation and therefore constitute the potential in which the nuclei exert their motion. The nuclear dynamics consist of vibration and rotation and can be described by the following ansatz if the coupling between these two movements is neglected:

$$\psi_N = \psi_{vib} \cdot \psi_{rot}. \quad (3.4)$$

Binding potentials feature a potential well that supports a series of bound *rovibrational states*. Writing down the nuclear equation, one can determine the quantized energies of the nuclear motion in these potentials. Assuming for example the unphysical case that the distance R between the atoms is fixed at R_e (rigid rotator), one obtains for the rotational structure in units of wave numbers¹:

$$F(\ell) = \frac{E_{rot}}{hc} = B_e \ell(\ell + 1). \quad (3.5)$$

¹Wave numbers are defined in the spectroscopic literature as the inverse vacuum wavelength $1/\lambda_{vacuum}$. They are given in cm^{-1} where 1 cm^{-1} corresponds to roughly 30 GHz.

3.1 Theory of Diatomic Molecules

Here, the rotational quantum number² is denoted by ℓ . $B_e = \frac{h}{8\pi^2\mu R_e^2}$ is called the *rotational constant* of the molecule, where the internuclear distance is approximated by the equilibrium distance R_e and μ is the reduced mass of the nuclear system. When considering the vibrational motion of the nuclei, one has to know something about the potential energy curve $U_n(R)$. The simplest approximation is to expand the potential in a Taylor series around the equilibrium position. This yields the quantized vibrational energies in wavenumbers with vibrational quantum number v

$$G(v) = \omega_e \left(v + \frac{1}{2} \right) - \omega_e x_e \left(v + \frac{1}{2} \right)^2 + \omega_e y_e \left(v + \frac{1}{2} \right)^3 + \dots \quad (3.6)$$

The first term describes the energy structure of a harmonic oscillator. The higher order terms are corrections where the constants $\omega_e x_e$ and $\omega_e y_e$ can be determined spectroscopically.

It is unphysical to neglect the effect of rotation on the vibration of the molecule, because the rotation will tend to pull the two nuclei further apart. The rotational energy structure of the vibrating rotor is given by

$$F_v(\ell) = B_v \ell(\ell + 1) - D_v \ell^2(\ell + 1)^2 + \dots, \quad (3.7)$$

where both B_v and D_v depend on the vibrational quantum number v .

Putting the different contributions together, the energy of a given rovibrational state in wave numbers amounts to

$$E_{rovib}(v, \ell)/(hc) = \nu_e + G(v) + F_v(\ell), \quad (3.8)$$

ν_e is the energy of the bottom of the electronic state given in wave numbers (zero for the ground state).

Sometimes an expression for the energy of the vibrating rotator that was introduced by Dunham is used in the literature. For a brief summary see reference [Hil07]. Reference material for molecular constants of diatomic molecules is available online [NIS07].

Molecular State Labeling

Different electronic states of diatomic molecules are classified according to three criteria:

1. their energy E_n ,
2. the angular momenta and spins of the electrons and their couplings, and
3. the symmetry properties of the electronic wave function.

²The symbol for the rotational quantum number is not completely agreed on in the literature. We use ℓ here as customary in scattering theory to stay consistent with the previous discussion in section 2.2.2. In molecular theory and spectroscopy, it is denoted by R , see references [LB04, Hil07].

3 Molecular Structure

The choice the quantum numbers used to label molecular states depends on which quantum numbers are good, meaning that they are associated with conserved quantities. We will first be concerned with the usual Born-Oppenheimer potentials and then discuss some extensions.

Energy Labeling Based on their energetic sequence, it is customary to distinguish molecular electronic states by latin letters. The ground state of the molecule is traditionally labeled with the letter X. The energetically next higher state that can be reached from the ground state by an allowed optical dipole transition is denoted A, the next excited state B, and so forth. States that cannot be reached from the ground state (e.g. triplet states when the ground state is singlet) are denoted by a, b, c... in the order of increasing energy. For historical reasons, there are exceptions to this general rule.

Angular Momenta An electron has orbital angular momentum³ ℓ as well as spin s . The orbital angular momenta ℓ_i of the individual electrons in the molecule add up vectorially to an overall electronic angular momentum $\mathbf{L} = \sum \ell_i$ and the individual spins add up to yield the total electronic spin $\mathbf{S} = \sum s_i$.

Contrary to individual atoms⁴, where the nuclear charge distribution is spherically symmetric, the internuclear electric field reduces the symmetry from spherical to cylindrical. The internuclear axis of diatomic molecules determines a quantization axis. The usual quantum numbers are not good quantum numbers any more because they are associated with operators that do not commute with the Hamiltonian. Generally speaking, for diatomic molecules the projections of the different angular momenta on the internuclear axis are good quantum numbers. Similar to the case of the Stark effect for atoms in an external electric field we can expect that \mathbf{L} is not conserved. In contrast, M_L , the projection of \mathbf{L} along the electric field direction, is a good quantum number. It can assume the values $M_L = -L, -L + 1, \dots, L - 1, L$. States with $L \geq 1$ are doubly degenerate due to the fact that $\pm M_L$ states have the same energy. Therefore, it makes sense to denote the states with the absolute value of M_L rather than with M_L . This degeneracy holds for the non-rotating molecule but it is lifted in the rotating molecule. The absolute value of the projection of \mathbf{L} on the internuclear axis is denoted by

$$\Lambda = |M_L|, \quad (3.9)$$

and therefore

$$\Lambda = 0, 1, 2, \dots, L.$$

³This is not to be confused with the angular momentum of the nuclear rotation for which we use the same symbol.

⁴As a reminder, atomic states are labeled according to $n^{2s+1}l_j$, where n is the principal quantum number, s is the quantum number for total electron spin, l is the total electron orbital angular momentum and $j = s + l$. The electron orbital angular momentum is encoded by letters S, P, D, \dots for $l = 0, 1, 2, \dots$. So for the ground state of the Cs atom the designation $6^2S_{1/2}$ arises. F is the quantum number for the total atomic angular momentum including nuclear spin. The ground state hyperfine transition is the clock transition defining our second.

For molecular state labeling, the different values of Λ are encoded by greek capital letters in analogy to the electronic orbital angular momentum of atoms that is encoded by latin capital letters:

$$\begin{array}{cccc} \Lambda = & 0 & 1 & 2 & \dots \\ \text{State:} & \Sigma & \Pi & \Delta & \dots \end{array}$$

In contrast to the electronic angular momentum, the quantum number S associated with the total electronic spin \mathbf{S} and its projection on the quantization axis both remain good quantum numbers if the electrostatic interaction is dominant since the Hamiltonian does not involve the electrons' spin. The projection is denoted by the quantum number

$$\Sigma = M_S = -S, -S + 1, \dots, S. \quad (3.10)$$

Note that the symbol Σ is used for two different things. First to label states with $\Lambda = 0$ and second for the projection quantum number of the aggregate electronic spin M_S . For $\Lambda = 0$ states, states with the same S but different Σ are degenerate. For $\Lambda \neq 0$ states, there will be a splitting in $2S + 1$ components according to the value of Σ . This is due to the magnetic field generated by the electron motion that leads to spin-orbit coupling, as discussed further below.

One defines the total electronic angular momentum [Hil07, LB04] as

$$\mathbf{J}_a = \mathbf{L} + \mathbf{S}. \quad (3.11)$$

\mathbf{J}_a is not fixed in space but precesses around the internuclear axis because the field exerts a torque on it. Again, only the projection of \mathbf{J}_a is a conserved quantity. The associated quantum number is

$$\Omega = |M_{J_a}|, \quad (3.12)$$

which can take on the values $\Omega = J_a, J_a - 1, \dots, \frac{1}{2}$ or 0. It is immediately clear that

$$\Omega = |\Lambda + \Sigma|.$$

One can define a vector of length Ω coinciding with the internuclear axis

$$\mathbf{\Omega} = \Omega \cdot \hat{\mathbf{z}}$$

where $\hat{\mathbf{z}}$ is a unity vector along the internuclear axis.

Born-Oppenheimer potentials are labeled according to the quantum number Λ and their multiplicity due to the aggregate electronic spin S . The multiplicity is $2S + 1$, defining singlet states for $S = 0$ and triplet states for $S = 1$. When spin-orbit coupling is taken into account as described below, the projection quantum number $\Omega = |\Lambda + \Sigma|$ is used as a further label. The designation of a state then reads:

$$^{2S+1}\Lambda_{\Omega}.$$

3 Molecular Structure

There are situations where Λ and Σ lose their meaning and therefore cannot be used to characterize molecular states. This will be discussed briefly in sections 3.1.2 and 3.1.4.

These angular momentum quantum numbers alone, however, are not sufficient to characterize a given potential. In addition, molecular symmetries have to be taken into account.

Symmetries For Σ states ($\Lambda = 0$), a “ \pm ” right superscript indicates a reflection symmetry of the spatial component of the electronic wave function in a plane containing the internuclear axis [Jon06]. A “+” sign indicates that the wave function is left unaltered by this operation whereas a “-” sign indicates that the wave function changes sign. This symmetry is only used for state designation in Σ states because for $\Lambda \neq 0$ the \pm states are energy degenerate.

For *homonuclear* diatomic molecules like Cs_2 , there is an additional symmetry concerning inversion of all electrons through the center of charge, which is equivalent to the exchange of nuclei. This is denoted by right subscripts “g” and “u”. If the sign of the wave function does not change when the inversion operation is applied, the state is said to have *gerade* symmetry, if the sign changes, the state is said to have *ungerade* symmetry. Both symmetries will be of major importance for determining selection rules.

The complete labeling for a particular electronic state of a homonuclear diatomic molecule is then

$$^{2S+1}\Lambda_{\Omega,g/u}^{(\pm)}$$

preceded by the letter that designates the energetic order of the states and in the case of Σ states with the addition of the “ \pm ” right superscript. Such state labeling is appropriate for most of the classical spectroscopic experiments on Cs_2 .

Long-Range Interactions between Atoms

The picture of two separated atoms interacting with each other is well suited to describe the long range part of the adiabatic Born-Oppenheimer potentials. As already discussed in section 2.2.1, for two ground state atoms, there is an attractive induced-dipole-induced-dipole interaction that is known as van der Waals interaction. The van der Waals interaction scales as $-\frac{C_6}{R^6}$ to leading order. The van der Waals coefficient C_6 is the same for the singlet ground state and lowest triplet state and thus the potentials are degenerate at large separations. At smaller separations, the exchange energy in the molecular Hamiltonian plays a more important role and the potentials become distinct. For excited states in homonuclear alkali dimers, when one atom is in a 2P state, the long range potential scales as $\frac{1}{R^3}$. This is due to a resonant dipole-dipole interaction

and results in a much longer range of the interaction than for the ground state. The Σ states scale as $\pm 2C_3/R^3$ and the Π states scale as $\pm C_3/R^3$ in terms of a single constant C_3 .

In heteronuclear alkali dimers both the ground and the excited state long range potentials scale as $-\frac{1}{R^6}$.

3.1.2 Spin-Orbit Interaction

The non-relativistic interactions set the largest energy scale in a molecule. The relativistic interactions, such as spin-orbit and hyperfine interactions, are weaker. Nevertheless, they are much larger than the energy scale defined by the translational motion of ultracold atoms [Jon06], which becomes immediately clear if one compares the atomic hyperfine splitting of 9 GHz in Cs with the translational energy of $\sim 21 \text{ kHz}\cdot h$ at a temperature of 1 μK .

The strongest of the relativistic interactions is the spin-orbit interaction. Spin-orbit interaction can lead to coupling between individual Born-Oppenheimer potentials, see section 3.2.2. Generally speaking, the coupling between individual Born-Oppenheimer potentials is relevant in the region of large internuclear distances, i.e. near to dissociation asymptote, where the Born-Oppenheimer interaction is reduced to a magnitude comparable to the spin-orbit interaction. This region is shown in the left panel of figure 3.1 for the potassium dimer. Each electronic state with given Λ has a multiplicity of $2S+1$ because Σ can adopt the values $-S, -S+1, \dots, S$, corresponding to different values of Ω . These $2S+1$ different molecular states for a given value of Λ and S are called *fine structure terms*, in analogy to the treatment in atoms. The simplest approach to model the spin-orbit interaction is to define a fine structure coupling term W_{SO} in the molecular Hamiltonian [Dem05] according to

$$W_{SO} = A \cdot \Lambda \cdot \Sigma$$

where A is a coupling constant, splitting states with $\Lambda > 0$. In general, the R -dependence of the spin-orbit interaction has to be taken into account by introducing a more complex effective Hamiltonian [Kok00b].

One can think of the coupling between L and S in terms of a magnetic field created by L that acts on S .

Molecular State Labeling

If the coupling between L and S is so strong that the electric field between the nuclei can't break it up, then Λ and Σ are not good quantum numbers any more and Hund's case c for the coupling of angular momenta applies, as will be discussed in section 3.1.4. Examples are the coupled 0_g^- electronically excited states that have been amply used in Cs_2 photoassociation. The respective potentials have to be computed by taking

the spin-orbit interaction into account [Jon06]. The states are then labeled according to the Hund's case c notation

$$\Omega_{g/u}^{\pm}$$

Here the superscript \pm for $\Omega = 0$ states refers to a reflection symmetry of the total electron wave function through a plane containing the internuclear axis [Jon06]. It differs from the reflection symmetry of nonrelativistic Σ states. In contrast to the nonrelativistic adiabatic Born-Oppenheimer potentials, these potentials are often referred to as *relativistic adiabatic* potentials [Jon06]. When considering the (attractive) electronic states dissociating to the $nS + nP_{1/2}$ and $nS + nP_{3/2}$ atomic asymptotes, where n is the principal atomic quantum number ($n = 6$ for the case of Cs), it is customary to differentiate potentials of the same $\Omega_{g/u}^{\pm}$ symmetry by a shorthand for the atomic asymptote they dissociate to: either $\Omega_{g/u}^{\pm}(P_{1/2})$ or $\Omega_{g/u}^{\pm}(P_{3/2})$.

Connection with the Born-Oppenheimer Potentials

The reader might wonder what the relationship between the relativistic potentials and the Born-Oppenheimer potentials is. One can look at this connection from two points of view: First, one is interested in how the relativistic potential energy curves arise from the Born-Oppenheimer energy curves. Second, it is interesting to realize which nonrelativistic Born-Oppenheimer potential energy curves are approached by each of the relativistic potentials. This is discussed here exemplarily for 0_u^+ states of the $nS + nP$ excited state of homonuclear alkali dimers, where n denotes the principal quantum number of the atom (6 in Cs atoms) because these are the states most relevant to the current project:

1. Hund's case c potentials are found as eigenvalues by diagonalizing the Hamiltonian containing the nonrelativistic potentials on the diagonal and the spin-orbit interaction W_{SO} on the off-diagonal. The spin-orbit interaction obeys the selection rules $u \leftrightarrow u$ and $g \leftrightarrow g$ concerning the inversion symmetry discussed above and $+ \leftrightarrow +$, $- \leftrightarrow -$ for reflection in a plane containing the nuclei [Pic06]. The relativistic adiabatic potentials $0_u^+(P_{1/2})$ and $0_u^+(P_{3/2})$ result as eigenvalues from diagonalizing the matrix

$$\begin{pmatrix} A^1\Sigma_u^+ & W_{SO} \\ W_{SO} & b^3\Pi_u \end{pmatrix}.$$

In the heavier alkali dimers like Cs_2 the spin-orbit coupling is large and therefore there are marked perturbations in the molecular spectra. One can think of the vibrational ladders of two states being coupled by the spin-orbit interaction. If two energies in the different potentials are nearly degenerate, the phenomenon of resonant coupling arises and the levels are strongly perturbed which is a peculiarity of the 0_u^+ potentials. An example for Rb_2 can be found in reference [Ami99] and an example for perturbations in Cs_2 photoassociation spectra can be found in reference [Pic06].

potential. This is schematically depicted in the right panel of figure 3.1. On the right, the dissociation limit into two free atoms is shown. The labeling here is for the particular case of K_2 . In the region of large internuclear distance, the relativistic potentials are listed. The lines indicate which Born-Oppenheimer potential they approach. The figure has to be read by taking into account that only gerade states in one region connect to gerade states in another region and only ungerade states connect to ungerade states.

3.1.3 Hyperfine Interactions

It was already discussed in section 2.2.1 that the atomic hyperfine structure provides well defined channels for ultracold scattering processes. For alkali atoms, the hyperfine structure is given by $a_{hf} \mathbf{s} \mathbf{i}$, where a_{hf} is the atomic hyperfine constant and \mathbf{i} is the nuclear atomic spin. Hyperfine interaction can couple the adiabatic Born-Oppenheimer potentials with different g/u symmetry or different total electronic spin S [Jon06]. For homonuclear dimers, the singlet ground state and lowest triplet potentials are coupled. At short range, the singlet and triplet potentials are well split. The effective hyperfine interaction is $a_{eff} \mathbf{S} \mathbf{I}$, where $\mathbf{I} = \mathbf{i}_a + \mathbf{i}_b$ is the total molecular nuclear spin. The connection between the long range part and the short range part is subtle. The wave function splits where the hyperfine and the exchange interaction become comparable in magnitude. One part samples the singlet potential and one part samples the triplet potential. They recombine and interfere on the way out, determining the precise pattern of the outgoing wave function in atomic scattering.

When molecular rotation ℓ is taken into account, it is found that ℓ is still a good quantum number. In order to find the potential curves for a given degree of rotational excitation, it suffices to add a term $\hbar^2 \ell(\ell + 1)/(2\mu R^2)$.

3.1.4 Angular Momenta and Hund's Cases

So far, rotation of the molecule and the coupling between the different angular momenta as a whole has not been taken into account systematically. It is worthwhile to take a more systematic look at these issues. Table 3.1 gives an overview of the different angular momenta encountered in a molecule and the conventional abbreviations. These are not always consistent in the literature, here we largely follow the convention by [Hil07, LB04, Hou01]. For example, in scattering theory, the mechanical rotation of the molecule about an axis that is perpendicular to the internuclear axis and contains the center of mass, is denoted by ℓ , as we do in this thesis. In the spectroscopic literature, it is customary to designate it with \mathbf{R} and the associated quantum number R . We defined Ω in section 3.1.1 as the projection of \mathbf{J}_a on the molecular axis. This is equivalent with the projection of \mathbf{J} because ℓ is by definition perpendicular to the internuclear axis. In section 3.2.3 we use $\mathbf{f} = \mathbf{F}_a + \mathbf{F}_b$ for the sum of the angular momenta of the individual ground state atoms including nuclear spin in order to be consistent with our previous publications and with the abbreviations used by the Stanford-NIST

collaboration for the Cs Feshbach molecules, see e.g. [Chi04b, Mar07]. The quantum number F is frequently used for total atomic spin, but this should not lead to confusion.

Table 3.1: **Molecular angular momenta and quantum numbers:** The different angular momenta relevant for diatomic molecules are listed. R and ℓ are used synonymously. Ω is either defined as the projection of \mathbf{J} or \mathbf{J}_a , both definitions being equivalent. The definitions of f and F below the horizontal line are those used by the Stanford-NIST analysis of ultracold Cs Feshbach molecules [Chi04b]. F_a and F_b are the total atomic angular momenta including nuclear spin of the alkali ground state atoms. $M = m_f + m_\ell$ is the projection on an external magnetic field. We allow this double use of F in this thesis because this quantum number is only used in the context of Cs Feshbach molecules in section 3.2.3 and so there is no risk of confusion. qu. n. = quantum number, a.m. = angular momentum, w/o = without. Table adapted from [Hil07].

Operator	Description	Total qu. n.	Projection qu. n.
ℓ or R	Mechanical rotation	ℓ or R	identical zero
L	Electronic orbital a.m.	L	Λ
S	Electronic spin	S	Σ
I	Nuclear spin	I	\dots
J	Total a.m. w/o nuclear spin: $\ell + L + S$	J	$\Omega = \Lambda + \Sigma $
F	Total a.m.: $J + I$	F	\dots
J_a	Total electronic a.m.: $L + S$	J_a	Ω
N	$\ell + L = J - S$	N	Λ
O	$J - L = \ell + S$	O	\dots
f	$F_a + F_b$	f	\dots
F	$f + \ell$	F	M

Hund’s cases are limiting cases for the different possibilities of how the individual angular momenta L , S , J_a or Ω (see below), and ℓ add up in a molecule to yield the total angular momentum J . This depends on the relative strength of the different couplings and determines which quantum numbers are “good” (well-defined). The nonrelativistic Born-Oppenheimer interaction locks the electron orbital angular momentum L to the internuclear axis. The spin-orbit interaction couples L with S . The mechanical rotation of the molecule couples the electron angular momenta L and S to the rotational angular momentum ℓ [Jon06]. Often, the coupling scheme changes with the internuclear separation R because the relative magnitude of the different interactions change and the angular momenta recouple in a different way. Hund’s cases determine which choice of basis function is appropriate for theoretical treatment. This choice depends on the internuclear distance. We are only ever dealing with one particular molecule, the different coupling cases apply to different ranges of internuclear separation of the same molecule.

There are five cases $a - e$ discussed by Hund, not all of them are relevant to the current study. Schematic illustrations are given in figure 3.2. The discussion here follows

3 Molecular Structure

the review article by Jones and coworkers [Jon06], the book by Demtröder [Dem05] and the book by Hill and Lee [Hil07]. A good online resource for the calculation of rotational structure is the tutorial by Jon Hougen, available online at [Hou01].

In section 3.1.1 equation 3.7 constitutes an expression for the rotational energy structure. The only quantum number that remains good in all coupling cases is J . Analyzing the different coupling possibilities, it is seen that the rotational progression is not always determined by J . Therefore, we can generalize equation 3.7 to the following form, again in wavenumbers (cm^{-1}):

$$F_v(X) = B_v X(X + 1) + \dots \quad (3.13)$$

The letter X stands for the appropriate angular momentum quantum number determining the rotational pattern. X is determined by the way the individual angular momenta couple in a particular Hund's case. Only in pure Hund's coupling cases, this simple expression is appropriate. When the coupling scheme is intermediate between two cases, more complex relations than equation 3.13 result.

In conventional molecular spectroscopy, the states that can be analyzed lie deep down in the respective potential wells and typically have inner and outer classical turning points below $20 a_0$. For such separations, the splitting between individual Born-Oppenheimer potentials is much larger than the relativistic spin-orbit energies and rotational energies. These states are best described by Hund's cases a and b which differ in the relative strength of the spin-orbit and rotational interaction.

Hund's case a

In Hund's case a the interaction between the electronic spin S and the magnetic field caused by the precession of the electronic angular momentum L around the internuclear axis is larger than the direct coupling between L and S . The electronic orbital angular momentum L is coupled to the molecular axis by the strong axial internuclear field. Therefore, also S is constrained to precess around the internuclear axis, but the vectors L and S precess independently around the internuclear axis. Their projections Λ and Σ are well defined and so is the sum of these projections Ω . The coupling of the vector Ω and the rotational angular momentum ℓ yields

$$\mathbf{J} = \mathbf{\Omega} + \boldsymbol{\ell}.$$

Remember that $\boldsymbol{\ell}$ and $\mathbf{\Omega}$ are perpendicular to each other.

Typically for $\Lambda \neq 0$ and $S \neq 0$ Hund's case a is valid for low J . For example low lying states in the $b^3\Pi_u$ electronic potential largely obey Hund's case a coupling, even though there are small contributions to the wave functions from the $A^1\Sigma_u^+$ state due to spin-orbit coupling even below the $A^1\Sigma_u^+$ potential minimum.

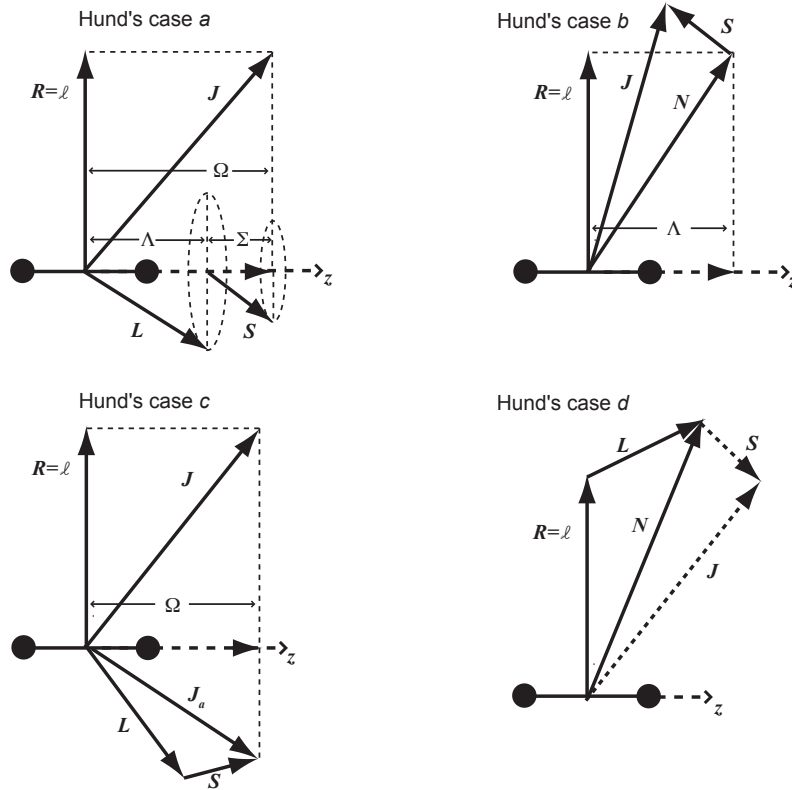


Figure 3.2: Vector model for Hund's cases *a* – *d*: Details are given in the text. Designation of the different angular momenta is consistent with references [Hi107, LB04]. Figure adapted from reference [Dem05].

The good, i.e. well defined, quantum numbers are $n, J, S, \Lambda, \Sigma, \Omega$ and the projection of \mathbf{J} on an axis in the laboratory frame M_J . The quantum number n includes the energetic numbering of the electronic states.

The rotational progression is [Dul04]

$$F_v(J) = B_v[J(J+1) - \Omega^2 + S(S+1) - \Sigma^2] + \dots, \quad (3.14)$$

where $J = \Omega, \Omega + 1, \dots$. The usual way

$${}^{2S+1}\Lambda_{\Omega,(g/u)}^{(\pm)}$$

to label molecular potentials is useful for case *a* coupling.

Hund's case *b*

Hund's case *b* is important for molecules with small spin-orbit coupling. In case *b*, the electron spin \mathbf{S} is only very weakly coupled or not coupled at all to the molecular axis.

3 Molecular Structure

Typically, states with $\Lambda = 0$ and $S \neq 0$ obey Hund's case *b* coupling. Weak coupling is easily understood when $\Lambda = 0$ because the magnetic field with which S can interact will be very small, but it also can occur in situations with $\Lambda \neq 0$. The spin S will tend to couple to the rotation vector instead of the internuclear axis. L is still coupled to the molecular axis and therefore Λ is a good quantum number. Since S is decoupled from the molecular axis, Σ and Ω lose their meaning as quantum numbers. The vector $\Lambda \cdot \hat{z}$, where \hat{z} is a unity vector along the internuclear axis, adds up with ℓ to form an angular momentum [Dem05] N

$$N = \Lambda \cdot \hat{z} + \ell$$

and N couples with S to yield the total angular momentum

$$J = N + S.$$

The rotational progression is given by [Dul04]

$$F_v(J) = B_v[N(N+1) - \Lambda^2] + \dots$$

The $a^3\Sigma_u^+$ lowest triplet state of the alkali dimers can serve as an example. For singlet states ($S = 0$) case *a* and *b* are equivalent and they are labeled by case *a* nomenclature. The $X^1\Sigma_u^+$ electronic ground state is an example of such a situation.

Hund's case *c*

Hund's case *c* typically applies when states with different Ω are widely separated compared to the other energy scales as in the left panel of figure 3.1, meaning that the spin-orbit interaction is comparable to the Born-Oppenheimer interaction and both are larger than the rotational interaction. It was mentioned in section 3.1.2 that the quantum numbers Λ and Σ lose their meaning and therefore molecular state labeling is according to $\Omega_{g/u}^{(\pm)}$. This scheme is usually addressed in photoassociation experiments where electronically excited states near the asymptote are reached. In the present study, spin-orbit coupling has resonant character for the 0_u^+ potentials and plays an important role over the whole range of binding energies. For Hund's case *c* the spin-orbit interaction is larger than the coupling of L to the molecular axis. L and S couple first to give $J_a = L + S$ before coupling to the internuclear axis. Its projection Ω is a good quantum number, whereas the quantum numbers Λ and Σ are not defined any more. The projection defines $\Omega = J_a \cdot \hat{z}$. Ω couples to the mechanical rotation ℓ to yield the total angular momentum J

$$J = J_a \cdot \hat{z} + \ell.$$

The states are labeled with Ω and the relevant symmetries, which was discussed in section 3.1.2. Therefore, this labeling convention is often referred to as "case *c*" labeling. The rotational progression is $X = J$, as in case *a*.

Hund's case d

For Hund's case d neither L nor S is coupled to the internuclear axis. This case applies to very weakly bound states of the two alkali dimer electronic ground state potentials, $X^1\Sigma_g^+$ and $a^3\Sigma_u^+$ [Jon06]. The molecular orbitals are basically a combination of atomic s-orbitals, which implies that $L = 0$ and there is no spin-orbit interaction. The rotational progression is therefore $X = \ell$. For the weakly bound levels of the electronic ground state in alkali dimers, the hyperfine interaction that couples the electron spin to the nuclear spin cannot be ignored and, in addition, the weaker relativistic interactions like second-order spin-orbit and magnetic spin-spin interactions play a role. For an adequate description of Cs Feshbach molecules (see section 3.2.3) all these contributions have to be taken into account.

Summary of Molecular Symmetries

For completeness this section gives a short summary of molecular symmetries. For our purposes the first three points are the most relevant ones.

- For Σ states ($\Lambda = 0$) a “ \pm ” right superscript indicates a reflection symmetry of the spatial component of the electronic wave function in a plane containing the internuclear axis. This symmetry is only used for designation of Σ states because for $\Lambda \neq 0$ the \pm states will be energy degenerate.
- The designation is slightly different for Hund's case c states. Here the superscript “ \pm ” for $\Omega = 0$ states refers to a reflection symmetry of the total electron wave function through a plane containing the internuclear axis [Jon06].
- Inversion i only applies to homonuclear molecules and designates molecule-fixed inversion of the coordinates of all electrons and nuclei through the center of mass. It defines g/u symmetry.
- The nuclear wave function is given by $\psi_N = \psi_{vib} \cdot \psi_{rot}$. The vibrational part depends only on the internuclear separation R and therefore always has positive symmetry with respect to reflection and inversion [Hil07]. The rotational wave function is proportional to the spherical harmonics $Y_{\ell,m}$ and thus has the following symmetry under inversion: $\psi_{rot} \rightarrow \psi_{rot}$ for even ℓ and $\psi_{rot} \rightarrow -\psi_{rot}$ for odd ℓ .
- The total wave function of a homonuclear molecule, including rotation but excluding nuclear spin, is classified as s (symmetric) or a (antisymmetric) according to whether it is even or odd with respect to nuclear exchange [LB04].
- For heteronuclear systems with $\Lambda = 0$, in Σ^+ states the even rotational levels have positive symmetry (\oplus) and for Σ^- states the even rotational levels have negative symmetry (\ominus).

3 Molecular Structure

In homonuclear molecules, the g/u symmetry has to be taken into account: each rotational level of a given electronic state is assigned either positive (\oplus) or negative (\ominus) symmetry. This combines with the g/u symmetry and leads to levels that are either symmetric (s) or antisymmetric (a) [Hil07]. Similarly, rotational states can either be classified as e or f states [LB04].

- Reflection σ_v of the total molecular wave function (electronic-vibration-rotation or rovibronic wave function) in the molecule-fixed coordinate system [LB04, Dem05] through a plane containing the internuclear axis specifies the parity \pm of a state. In fact, parity is defined by the even/odness of the complete molecular wave function with respect to inversion of the laboratory-frame coordinates of all electrons and nuclei, but the operation of σ_v is equivalent to this.
- ^{133}Cs has nuclear spin $7/2$. The nuclei behave as fermions and the overall wave function including nuclear spin will transform like a fermion under exchange of the identical nuclei.

3.2 Cs Molecular Structure

In this section, the specific properties of the cesium dimer will be reviewed. For the current spectroscopic experiments, the properties of Cs Feshbach molecules and the properties of the first electronically excited state of Cs_2 are most important. Feshbach molecules have been studied in detail. There is spectroscopic data available for tightly bound vibrational levels in various excited states that were obtained with classical spectroscopy. The current project is aimed at driving optical transitions of the Feshbach molecules in the $1.55 \mu\text{m}$ wavelength region, i.e. driving a transition from very loosely bound molecules in the electronic ground state to tightly bound excited state levels. Calculations of expected transition wavelengths are currently based on ab initio potential curves. We plan to transfer the Feshbach molecules to the rovibrational ground state of the $X^1\Sigma_g^+$ electronic ground state by means of a two-photon transfer process. The $X^1\Sigma_g^+$ state is spectroscopically well known [Wei85, Ami02].

3.2.1 Ground State of the Cesium Molecule

Ground state potential curves for the singlet and the triplet state are shown in figure 2.4 along with the three different scattering channels defined by the atomic hyperfine structure. The dissociation limit D_e of the singlet ground state $X^1\Sigma_g^+$ is [Ami02, Wei85]

$$D_e(X^1\Sigma_g^+) = 3649.88 \pm 0.45 \text{ cm}^{-1}, \quad (3.15)$$

corresponding to ~ 110 THz. The number of singlet vibrational levels is 155. The lowest vibrational level is located at 20.981 cm^{-1} (629 THz) above the potential minimum and the rotational constant for the $v = 0$ singlet vibrational level is $B_v = 0.0117313$

cm^{-1} , which corresponds to 352 MHz. The spacing between the first and the second vibrational level is 41.855 cm^{-1} , corresponding to 1.26 THz.

The lowest triplet state has the symmetry ${}^3\Sigma_u^+$, its potential depth is $\sim 290 \text{ cm}^{-1}$ [Wei85] and the number of bound levels is ~ 50 .

3.2.2 Cs Excited State Potentials

Tightly bound vibrational levels of various Cs_2 electronically excited states have been studied with classical Fourier transform spectroscopy, see e.g. references [Ver87, Ami88b, Ami88a]. States near the dissociation threshold are accessible to photoassociation spectroscopy. The first electronically excited state of the Cs dimer exhibits some interesting features. First, the 0_u^+ states experience strong perturbations in the form of resonant coupling between states that exhibit the same symmetry but approach different atomic asymptotes. Secondly, the $0_g^-(P_{3/2})$ and $1_u(P_{3/2})$ states of the alkali dimers have become famous for the long range nature of the potentials where there is either a single potential minimum at very large internuclear distances or an additional outer well in the potential curve that supports long-range bound states. In such long-range states the atoms actually spend all their time far apart from each other. The $0_g^-(P_{3/2})$ state has been exploited for the formation of ultracold Cs_2 molecules [Fio98] and studied in detail in [Fio99]. Spectra of the $1_u(P_{3/2})$ state of Cs_2 have been obtained by the Orsay group [Com00]. The review article by Masnou-Seeuws and Pillet [MS01] treats photoassociation and ultracold molecule production with a special emphasis on Cs. Figure 3.3 shows Hund's case *c* ab initio potential curves calculated by Spiess [Spi89].

In the context of the present study states that are farther detuned from the atomic transition are of primary interest, most notably the 0_u^+ and $1_u(P_{1/2})$ states (Hund's case *c* notation). The two 0_u^+ states dissociate to different atomic asymptotes, namely the $6S + 6P_{1/2}$ and the $6S + 6P_{3/2}$ asymptotes in cesium. The two 0_u^+ states arise from spin-orbit coupling between the $A^1\Sigma_u^+$ and the $b^3\Pi_u$ states in Hund's case *a* notation as introduced in sections 3.1.2 and 3.1.4. The Hund's case *a* states are *diabatic potentials* with respect to the spin-orbit interaction whereas the Hund's case *c* representation are *adiabatic* with respect to the spin-orbit coupling [Pic06]. As mentioned above they are obtained by diagonalizing the Hamiltonian that contains the spin-orbit coupling as off-diagonal elements. The relation between the two representations is illustrated in figure 3.4. Note that the Hund's case *a* potentials cross each other whereas the Hund's case *c* potentials produce an avoided crossing at $\sim 11a_0$. The 0_u^+ states are noteworthy for constituting a textbook example of resonant coupling between two states that have the same symmetry but dissociate to different atomic asymptotes [LB04]. This resonant coupling arises between rovibrational states in the singlet and triplet potentials whose constants of motion are nearly degenerate. It requires the total angular momenta J of the levels to be equal. It is associated with a spoiling of the spin quantum number.

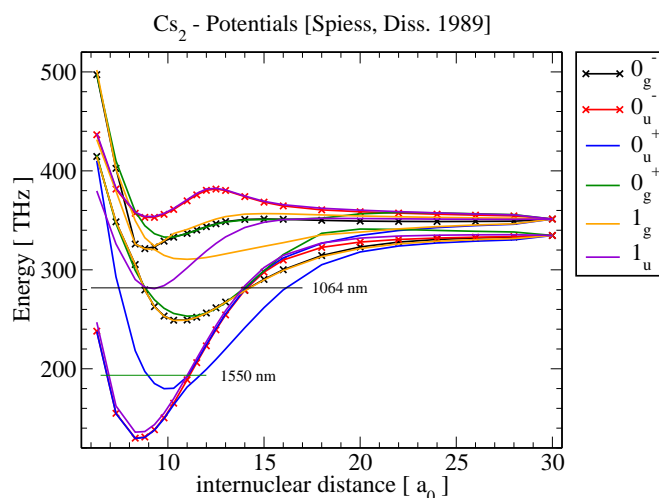


Figure 3.3: Cs₂ excited state potential curves: Ab initio potential curves for the first electronically excited state of Cs₂. The two atomic asymptotes that the potentials dissociate to can be clearly discerned. These are the 6S+6P_{3/2} and the 6S+6P_{1/2} asymptotes. Each of the potentials can be traced to one of these asymptotes and therefore it is convenient to label states of the same symmetry additionally with a shorthand for the asymptote they dissociate to, e.g. 0_u⁺(P_{1/2}) and 0_u⁺(P_{3/2}). There is an avoided crossing between these two states at $\sim 11a_0$. The two horizontal lines indicate the approximate regions accessible to spectroscopy with a laser of 1550 nm wavelength and of 1064 nm wavelength starting with very weakly bound Feshbach molecules in the ground state. The potentials accessible by a 1.55 μm laser all have *ungerade* symmetry, which means that they can only be accessed from a *gerade* state by an allowed optical dipole transition. Therefore, only the singlet ground state is expected to contribute to transition rates. In contrast, some of the potentials accessible by the 1064 nm laser that we use for atom trapping in our experiments can also be accessed from the lowest triplet state, because they have *g* symmetry. Figure courtesy of Christiane Koch and Olivier Dulieu.

The contribution of the singlet and the triplet state to a given molecular level varies with internuclear distance R reflecting the recoupling of the angular momenta as the atoms move closer [Pic06]. The coupling leads to characteristic perturbations in the molecular spectra manifested as irregularities in the vibrational level spacing and in the rotational constants. The first experimental observation of spectral perturbations in alkali dimers dates back to the year 1909 [Woo09] and they have been addressed both experimentally and theoretically, see for example [Ami99] for the case of Rb₂ and [Pic06, Dio01] for the case of Cs₂ or [Kok00b, Kok00a] for further theoretical treatment. The theoretical calculation of bound levels in these potentials is very sensitive to the potential shape. Shifting the repulsive wall by 0.01 a_0 for example already leads to a modification of the position of the energy levels and of the perturbation structure to such an extent that it cannot be hoped to find agreement between theory and experiment based on the current accuracy of molecular potentials. In addition, theoretical results are very sensitive to the choice of the magnitude and R -dependence of the

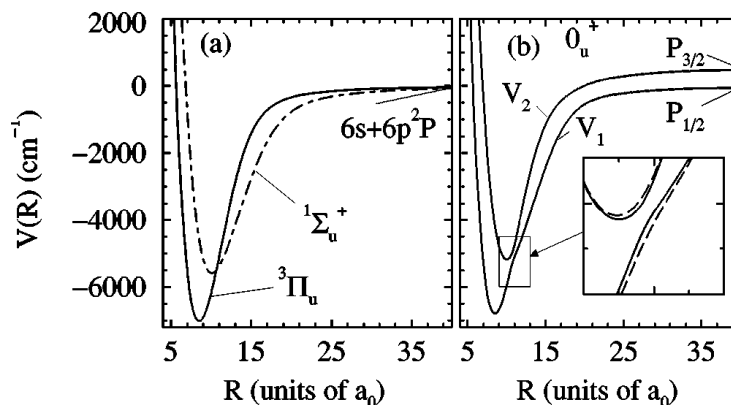


Figure 3.4: Cs₂ 0_u⁺ states: The left panel shows the states in Hund's case *a* representation that cross each other at $\sim 11a_0$. The Hund's case *c* potentials in the right panel produce an avoided crossing instead. They are calculated taking the spin-orbit interaction into account. The dashed and solid lines represent two different theoretical models. Figure taken from [Kok00b]

spin-orbit coupling [Kok00b]. Even though the Hund's case *c* potentials account for the spin-orbit coupling between the two Hund's case *a* potential curves, the resonant coupling effect precludes the picture of two uncoupled Hund's case *c* channels with their separate vibrational ladders. The perturbations are present over the entire spectral range of the potential reflected by an oscillation of the rotational constant between a small value corresponding to the 0_u⁺(P_{1/2}) unperturbed series and a larger value corresponding to the 0_u⁺(P_{3/2}) series.

Even though the absolute position of deeply bound levels in the electronically excited state is hard to predict from ab initio calculated potential curves, such calculations are still a very useful guidance for the experiment in order to determine the expected level spacing and expected transition rates. The potential curves can be further adjusted for the available experimental data, see for example the spectroscopic experiments by Vergès and Amiot [Ver87].

The position of the theoretical potential curves as a whole can be fixed to an experimental value. The A¹Σ_u⁺ state (Hund's case *a* notation) has been studied by Fourier transform spectroscopy by Vergès and Amiot [Ver87]. They derive a potential energy curve and determine the T_e value to $T_e = 9627.06 \text{ cm}^{-1}$. T_e is the energy difference between the bottom of the potential wells of the excited state and of the ground state. The energy of the bottom of the well of the A¹Σ_u⁺ state corresponds to the energy of the bottom of the well of the 0_u⁺(P_{3/2}) state, as can be seen from figure 3.4. They determine the rotational constant to $B_e = 9.06 \cdot 10^{-3} \text{ cm}^{-1}$ and the equilibrium distance between the atoms, i.e. the position of the bottom of the potential well, to $R_e = 0.5292 \text{ nm}$. The potential depth was evaluated to be $D_e(A^1\Sigma_u^+) = 5200.7 \text{ cm}^{-1}$. The experiment was done with a heat pipe containing Cs₂ and therefore mainly rotationally highly excited levels are addressed whereas in the ultracold regime, slowly rotating molecules are

3 Molecular Structure

created.

The dissociation energy of the singlet ground state $X^1\Sigma_g^+$ is $D_e(X^1\Sigma_g^+) = 3649.88 \text{ cm}^{-1}$ [Ami02]. With $T_e(A^1\Sigma_u^+) = 9627.06 \text{ cm}^{-1}$, the bottom of the $A^1\Sigma_u^+$ well is located 5977.18 cm^{-1} above the $6S + 6S$ threshold.

3.2.3 Near Threshold Ground State Structure - Feshbach Molecules

Near threshold molecular structure is not easily addressed experimentally by conventional spectroscopic studies [Wei85]. Recently, it has been addressed by two-color photoassociation [Van04] and Feshbach-spectroscopy, especially by the Stanford group with theory support from NIST [Vul99a, Vul99b, Chi00, Leo00, Chi04b]. The singlet and the triplet scattering length for Cs are $a_S = 280.37 a_0$ and $a_T = 2440 a_0$, respectively [Chi04b], the C_6 coefficient is $6860 E_H a_0^6$, where $E_H = 4.35974 \text{ aJ}$ is one Hartree, $C_8 = 860000 E_H a_0^8$.

In different regions of internuclear separation, it is convenient to use different basis sets. In the region of large internuclear distance the loosely bound molecule can be seen as being composed of two largely unperturbed ground state atoms. At smaller internuclear separation the exchange energy becomes comparable to and finally much larger than the atomic hyperfine energy and the individual electron spins couple to each other to yield the total molecular spin S . Molecular spin can take on the values $S=0$ and $S=1$ characterizing the singlet and triplet Born-Oppenheimer potentials, respectively. This is reflected by the choice of molecular basis for short range and for long range.

The molecular basis $|(SI)f\ell FM\rangle$ is useful at short range. Here, S is the total electron spin $S = s_a + s_b$ and I is the total nuclear spin $I = i_a + i_b$. They couple to form $f = S + I$. The nuclear mechanical angular momentum is given by ℓ and total angular momentum is $F = f + \ell$. M is the projection of F on the magnetic field axis.

At long range, it is more convenient to use a separated atoms basis but it leads to off-diagonal elements at short range [Koh06]. The long range basis set $|(F_a F_b)f\ell FM\rangle$ couples the total atomic spins F_a and F_b to yield $f = F_a + F_b$. Here, the total molecular angular momentum is $F = f + \ell$ and M is again the projection of F on the magnetic field axis. This basis is useful at low magnetic fields where the Zeeman levels do not anti-cross and where f may be viewed as a good quantum number [Koh06]. Although, strictly speaking, the atomic total angular momenta F_a and F_b are only good quantum numbers in the case of zero magnetic field, they remain approximately good quantum numbers in the region of weak magnetic fields. The work in our experiments is performed at low magnetic fields, therefore, this is an appropriate description. The selection rules for the Born-Oppenheimer Hamiltonian conserve ℓ and $f = F_a + F_b$. Bound states can therefore be labeled by the quantum numbers f, ℓ for zero magnetic

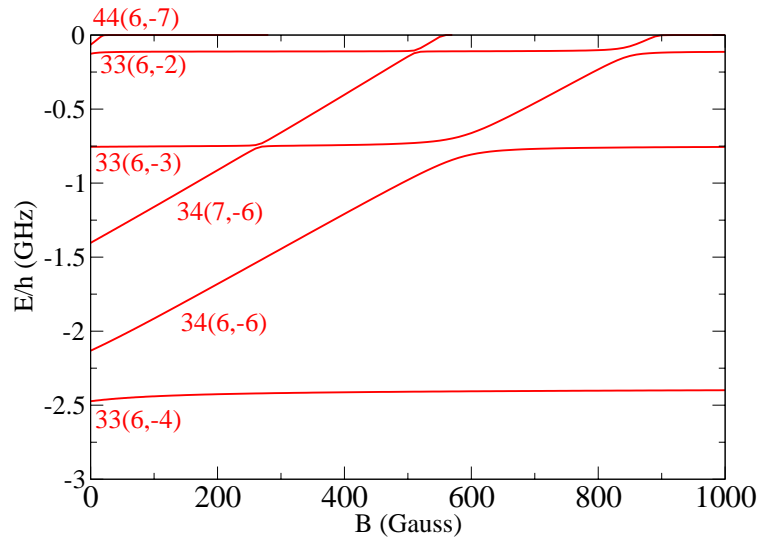


Figure 3.5: Cs molecular s -states: Energy structure of the Cs dimer below the $(3,3) \times (3,3)$ continuum as a function of magnetic field. Only s -states ($\ell = 0$) are shown. Labeling is according to the quantum numbers $F_a F_b(f, \nu)$, where ν is the vibrational quantum number as counted from threshold downwards. In the top left corner, the $6s$ state $44(6,-7)$ is barely seen, it turns over near 20 Gauss into the $33(6,-1)$ state which is not resolved.

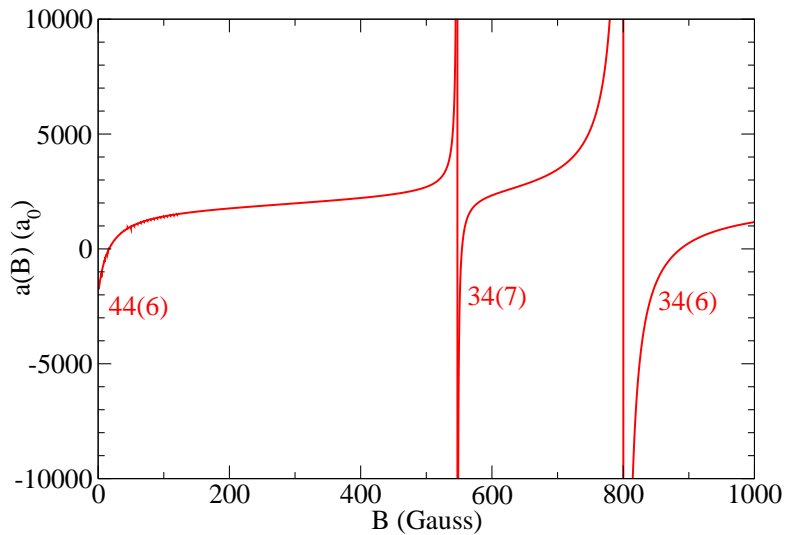


Figure 3.6: Scattering length of Cs: The scattering length of Cs in the $(3,3) \times (3,3)$ scattering channel is greatly modified as a function of magnetic field by the $44(6,-7)$, the $34(7,-6)$ and the $34(6,-6)$ states coupling to the $33(6,-1)$ state and then intersecting threshold.

3 Molecular Structure

field. At magnetic fields not equal to zero, the projection $m_f = m_{F_a} + m_{F_b}$ can be used as a label along with ℓ .

In the terminology of Feshbach molecules, states with $\ell = 0, 2, 4, \dots$ are denoted s, d, g, \dots states. Only even rotational quantum numbers occur because of the bosonic nature of ^{133}Cs , similar to the partial waves discussed on page 26.

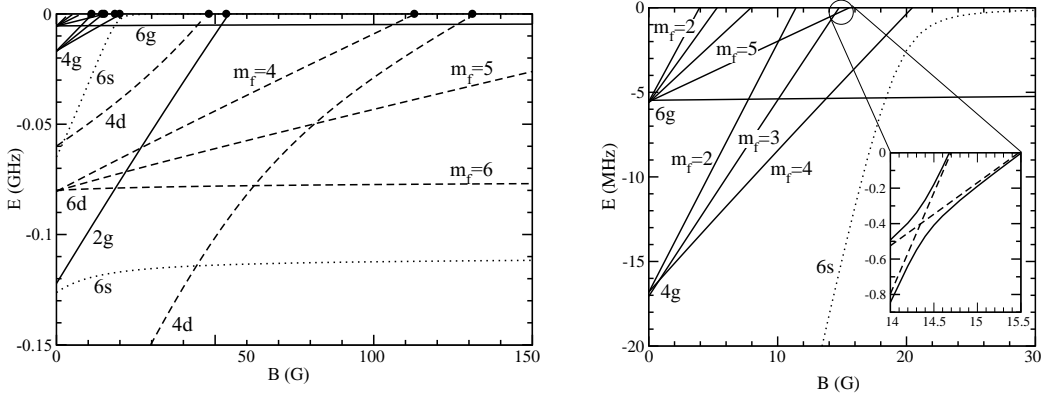


Figure 3.7: Low field molecular Cs dimer states: In the low-field region, shown here for 0-150 G and 0-30 G, state labeling can be done according to $f\ell(m_f)$. This is the region of magnetic fields relevant to our work. The molecular states up to g states ($\ell = 4$) below the $(3,3)\times(3,3)$ scattering threshold are shown. Note the different energy scales. The state $44(6,-7)/33(6,-1)$ that was not resolved in figure 3.5 can be identified as the $6s$ state turning over at 20 G. The filled circles in the left panel indicate the positions of d and g wave Feshbach resonances. Figure taken from [Chi04b].

The molecular Hamiltonian, including relativistic interactions, conserves parity and the total angular momentum $\mathbf{F} = \mathbf{f} + \boldsymbol{\ell}$ and its projection M for $B = 0$ or only $M = m_f + m_\ell$ for nonzero fields [Chi04b]. The Cs atoms in our experiment are polarized in their lowest internal hyperfine state $|F = 3, m_F = 3\rangle$ and therefore $m_f = 6$. Since only s -wave collisions are possible in the ultracold regime, m_ℓ is zero. The sum $M = m_f + m_\ell = 6$ is conserved during the collision, therefore only states with projection of the total angular momentum $M = 6$ are possible. The following discussion will focus on molecular states below the atomic $|F = 3, m_F = 3\rangle + |F = 3, m_F = 3\rangle$ scattering continuum or synonymously the $(3,3)\times(3,3)$ continuum which are relevant to our work.

Let us consider first molecular states in the basis $|(F_a F_b) f \ell F M\rangle$ with the rotational quantum number $\ell = 0$, i.e. s -states as shown in figure 3.5 at magnetic fields from 0 to 1000 Gauss. Weakly bound $6s$ states belonging to the channel $F_a = 3, F_b = 3$ and $f = 6$ are horizontal lines in this plot. The numbering is $F_a F_b(f, v)$, where v is the vibrational quantum number as counted from threshold downwards. Note that the state $33(6,-1)$ just below threshold is not resolved in this plot but plays an important

role for the characteristic behavior of the scattering length of Cs.

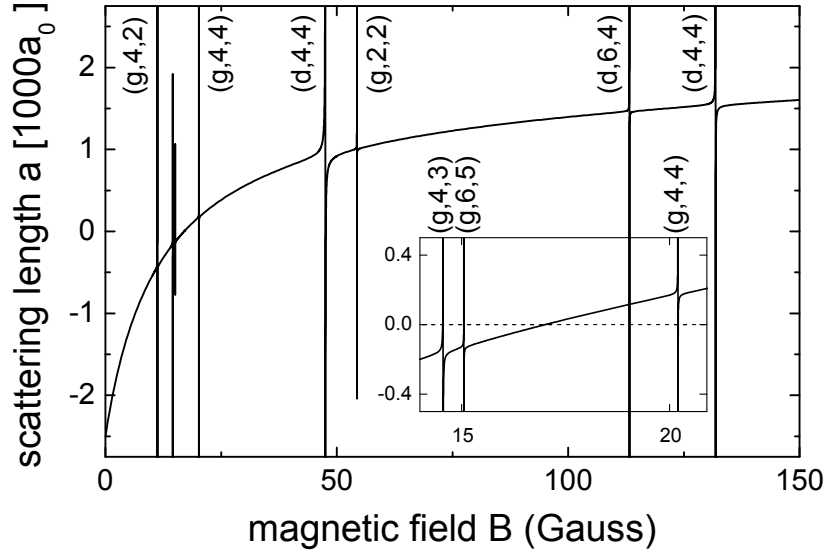


Figure 3.8: Cs scattering length: Scattering length of Cs up to 150 G. There is a smooth tunability due to the s wave Feshbach resonance caused by the $44(6,-7)$ state. In addition, a series of narrow higher order Feshbach resonances that are caused by coupling of the scattering threshold to d and g bound states can be identified. There is a d wave resonance at 48 G and g wave resonances at 11.0 G, 14.4 G, 15.0 G, 19.9 G, and 53.5 G. Figure taken from [Chi04b].

The inclined lines in this plot correspond to potentials associated with the scattering channels $F_a, F_b=3,4$ or $4,4$. Since these have different magnetic moments, they intersect the $3,3$ states and lead to strong avoided crossings. In fact, these states couple to the $33(6,-1)$ state lying just below threshold. Three broad s -wave Feshbach resonances arise from these states intersecting the threshold at -11.7 G, 550 G, and 800 G, as indicated in figure 3.6. At 11.7 G there is a Feshbach resonance for two colliding atoms in the $F = 3, m_F = -3$ state which translates into the value of -11.7 G for the $F = 3, m_F = 3$ state. Only the “shoulder” of this resonance which underlies the tunability of the scattering length at small magnetic field can be seen. The position of the Feshbach resonances is not identical with the position one would expect from the intersection of the unperturbed molecular state with the threshold. This is due to the strong avoided crossings with the $33(6,-1)$ state just below threshold. These Feshbach resonances give rise to the outstanding tunability of interactions in ultracold Cs quantum gases. In the current setup of the Cs BEC experiment, the region of small magnetic fields between 0 and 150 Gauss has been explored.

Examining the region of low magnetic fields closer and taking states with $\ell \neq 0$ into account, one finds a very rich spectrum of molecular states as indicated in figure

3.7. In particular, due to the relativistic interactions, several narrow higher order Feshbach resonances arise. These are shown up to g -wave resonances in the figure. In these plots, the $33(6,-1)$ state can be identified and is simply denoted as $6s$. It runs just below threshold but does not run parallel to it, causing the aforementioned Feshbach resonance at 550 G. As already pointed out, f remains approximately a good quantum number in the low field region and therefore the states are labeled with $f\ell$. States with different m_f can be traced back to zero magnetic field to a given value of f . Crossings between bound states are avoided when the second order spin-orbit and spin-spin interactions are taken into account [Chi04b]. One can broadly classify states into those that are appreciably curved and those that are not. The curvature arises from strong avoided crossings between states of the same $f\ell$ mediated by the Born-Oppenheimer, hyperfine and Zeeman interactions. These avoided crossings are much larger than the weak, i.e. narrow, avoided crossings mediated by second order spin-orbit and spin-spin interactions. It is now possible to experimentally populate all the shown states and in addition l -wave states ($\ell = 8$) not shown in the figure by either adiabatically following avoided crossings or by jumping them with fast magnetic field variations [Mar07]. The molecular states shown in figure 3.7 also couple to the continuum and yield narrow higher order Feshbach resonances, namely 8 g -wave and 3 d -wave resonances. All of these resonances can be used to populate the corresponding molecular states [Mar07]. The relativistic interactions in Cs are strong enough to warrant coupling of the s -wave scattering state to g -wave molecular states with $\Delta\ell = 4$. The s -wave scattering length is modified accordingly as a function of magnetic field as indicated in figure 3.8. In addition to the smooth tunability of the scattering length that mirrors the high magnetic field “shoulder” of the Feshbach resonance caused by the $44(6,-7)$ state, there is a series of narrow resonances. Note the zero crossing of the scattering length near 17 G.

Molecular states near threshold experience strong mixing of the singlet and triplet state. One can calculate the expectation value of the total electronic spin for these states. A value close to one indicates that the state is predominantly triplet, a value near 0 indicates that the state is predominantly singlet. Assuming that the individual states were composed of a statistical mixture of singlet and triplet components, the triplet component would be 75 % due to the threefold degeneracy of the triplet state and the absence of degeneracy of the singlet state.

3.3 Optical Transitions

The wavelength of the transition between two levels is given by the energy difference ΔE_{rovib} of the two involved rovibrational levels, see equations 3.8 and 3.13

$$\Delta E_{rovib}/(hc) = (v'_e - v''_e) + (G'(v') - G''(v'')) + (F'_v(J') - F''_v(J'')), \quad (3.16)$$

where J is the total angular momentum apart from nuclear spin [Hil07], see section 3.1.4. Here, the prime indicates the upper level and the double prime the lower level. By writing down the Hamiltonian for the coupling of two states by electromagnetic radiation and treating it with perturbation theory, one can determine the strength of the transition between the two states. If one then neglects retardation effects of the radiation across the particle, the *dipole approximation* is reached. The probability per second that an atom or a molecule absorbs a photon and accordingly the transition probability from state $|g\rangle$ to state $|e\rangle$ is found to be

$$\frac{dW_{ge}}{dt} = \frac{2\pi}{\hbar^2} |\mathbf{E}_0 \cdot \mathbf{D}_{ge}|^2, \quad (3.17)$$

where \mathbf{E}_0 is the electric field vector of the laser and \mathbf{D}_{ge} is the *dipole matrix element* between the initial and the final state [Dem05]. The strength of optical transitions between two states is then by the dipole matrix element between the initial and the final state wave functions $\Psi_g(\mathbf{r}, \mathbf{R})$ and $\Psi_e(\mathbf{r}, \mathbf{R})$ which has the form

$$\mathbf{D}_{ge} = \langle \Psi_e(\mathbf{r}, \mathbf{R}) | \mathbf{d} | \Psi_g(\mathbf{r}, \mathbf{R}) \rangle, \quad (3.18)$$

where \mathbf{d} is the dipole operator. The integration goes over all electronic and nuclear coordinates. The dipole operator for a diatomic molecule is

$$\mathbf{d} = -e \cdot \sum_i \mathbf{r}_i + Z_1 e \mathbf{R}_1 + Z_2 e \mathbf{R}_2 = \mathbf{d}_{el} + \mathbf{d}_N.$$

For homonuclear molecules $Z_1 = Z_2$ and since $\mathbf{R}_1 = -\mathbf{R}_2$ the nuclear contribution is zero $\mathbf{d}_N = 0$. In alkali dimers, only the valence electrons contribute appreciably to the electric dipole moment, inner shell electrons can be neglected.

Based on fundamental symmetries it can be determined between which states non vanishing dipole matrix elements can exist. These are the so called *selection rules*. Transitions that are forbidden by these rules can often still be driven due to higher order magnetic dipole or electric quadrupole matrix elements, but these are typically orders of magnitude smaller.

3.3.1 The Franck-Condon Principle

In order to simplify the calculation of molecular transition probabilities, it is very useful to make use of the fact that the time scale for electronic excitations is much shorter than the time scale for the nuclear motion. This implies that an electronic transition takes place at fixed internuclear distance R , i.e. the nuclei do not move appreciable during the time when the electronic transition takes place. This is analogous to the Born-Oppenheimer approximation, where the different timescales for electronic and nuclear motion led to the separation of the wave function into an electronic and a nuclear component and to the concept of potential energy curves.

3 Molecular Structure

In a classical picture, the nuclei move most slowly near the turning points of the potential and therefore spend most time in these regions. A transition is favored when one of the turning points of the ground state potentials nearly coincides with a turning point of the excited state potential. Quantum mechanically spoken, the Franck-Condon principle states that a transition is likely to take place if significant overlap exists between the initial and final state wave functions. This is analogous to the classical picture since the wave functions are peaked near the turning points of the potentials. Applying the Born-Oppenheimer separation of the total wave function $\Psi(\mathbf{r}, R)$ into an electronic wave function $\psi_{el}(\mathbf{r}, R)$ and a nuclear wave function $\psi_N(R) = \psi_{vib}(R) \cdot \psi_{rot}$, one can rewrite the matrix element as

$$\mathbf{D}_{ge} = \langle \psi_{el,e} \cdot \psi_{rot,e} | \mathbf{d}_{el} | \psi_{el,g} \cdot \psi_{rot,g} \rangle \cdot \langle \psi_{vib,e}(R) | \psi_{vib,g}(R) \rangle, \quad (3.19)$$

where we neglected the R -dependence of the electronic matrix element in order to separate it from the nuclear component, it is often evaluated at some mean distance \bar{R} or at the equilibrium distance R_e . It should be stressed that the electronic matrix element does in general depend on R and can lead to non-Franck-Condon behavior of transition probabilities. This relation assumes that the nuclear contribution to the matrix element vanishes as in homonuclear diatomic molecules and in transitions between different electronic states. The allowed transitions that render the first factor in equation 3.19 non-zero depend on certain selection rules as outlined below. In first approximation, its value can be taken similar to the atomic value.

The second factor in equation 3.19 represents the overlap of the excited state and ground state vibrational wave functions. Its square is called the *Franck-Condon factor* (FC factor) and crucially determines the strength of a given transition.

$$\text{FC factor} = |\langle \psi_{vib,e}(R) | \psi_{vib,g}(R) \rangle|^2 \quad (3.20)$$

3.3.2 Selection Rules

Selection rules determine which matrix elements can be nonzero. They fall into two categories: those that apply to all coupling cases and those that apply only to a particular Hund's case. If the initial and the final state are in the same coupling case, the respective selection rules for that case apply. If they are in different coupling cases, only the general rules hold. Designation of the angular momenta is according to table 3.1. The following selection rules hold for dipole transitions between different electronic states of diatomic molecules [Hil07, Dem05]. First we will briefly introduce the general selection rules and then the case-specific rules.

General Selection Rules

$$\Delta J = 0, \pm 1 \quad \text{with} \quad J' = 0 \Leftrightarrow J'' = 0 \quad (3.21)$$

As alluded to in section 3.1.1, each rotational level either has positive or negative symmetry \oplus and \ominus both in homonuclear and in heteronuclear diatomics. The selection

rule is

$$\oplus \leftrightarrow \ominus, \quad \oplus \leftrightarrow \oplus, \quad \ominus \leftrightarrow \ominus. \quad (3.22)$$

In homonuclear dimers, there is the additional g/u symmetry. This combines with the \oplus/\ominus symmetry to designate rotational levels either symmetric (s) or antisymmetric (a) with the selection rules

$$s \leftrightarrow s, \quad a \leftrightarrow a, \quad s \leftrightarrow a. \quad (3.23)$$

The selection rule for the g/u symmetry is

$$g \leftrightarrow u, \quad g \leftrightarrow g, \quad u \leftrightarrow u. \quad (3.24)$$

There is a selection rule operative for the case of homonuclear dimers for transitions to states with either $\Lambda = 0$ or $\Omega = 0$ [Jon06]. A given rotational line in such a state can only be reached from either only odd or only even waves. The precise relationship whether odd goes to odd or odd goes to even depends on whether the nuclei are bosons or fermions and whether the state has g or u symmetry. For example, odd rotational lines in the vibrational levels of the $A^1\Sigma_u^+$ state of a dimer with fermionic nuclei can only be reached from even partial waves. In photoassociation spectroscopy, this helps to explain the strength of the individual lines.

When the initial state does not have definite g/u symmetry, such as in ultracold ground state collisions, transitions to both g and u states become allowed [Jon06].

Hund's case a selection rules

Selection Rules for Electronic Wave Functions For Hund's case a coupling, the symmetry of the dipole operator implies the following rules:

$$\Sigma^+ \leftrightarrow \Sigma^+, \quad \Sigma^- \leftrightarrow \Sigma^-, \quad \Sigma^+ \leftrightarrow \Sigma^- \quad (3.25)$$

$$\Delta\Lambda = 0, \pm 1 \quad (3.26)$$

$$\Delta S = 0 \quad (3.27)$$

$$\Delta\Sigma = 0 \quad (3.28)$$

$$\Delta\Omega = 0, \pm 1 \quad \text{with the restriction } \Delta J \neq 0 \text{ when } \Omega = 0 \rightarrow \Omega = 0 \quad (3.29)$$

Selection rule 3.26 is modified for multiphoton processes involving N photons to $\Delta\Lambda = 0, \pm 1, \dots, \pm N$. The spin selection rule 3.27 stems from the fact that the electric

3 Molecular Structure

dipole moment does not contain spin variables. It is only strictly satisfied when the wave functions are pure, i.e. in the absence of spin-orbit interactions. Therefore, this selection rule is absent for case *c* coupling, see below. These transitions become allowed to a certain extent when states of different multiplicities are mixed by spin-orbit interaction.

According to the review article by Jones and coworkers [Jon06], there are still restrictions even when the initial state has mixed *g/u* and spin character as in ultracold collision experiments. Since the initial state in the collision of two ground state alkali atoms is a mixture of $^1\Sigma_g^+$ and $^3\Sigma_u^+$, transitions to $^1\Pi_g$ or $^3\Sigma_u^+$ are forbidden. This is in contrast with the experiments by Nikolov and coworkers [Nik00] who assign a photoassociation resonance to a $^1\Pi_g$ state, as illustrated in figure 6.4.

Selection Rules for Rotational Wave Functions

$$\Delta J = 0, \pm 1 \quad (3.30)$$

$$\Delta J = 0 \text{ is forbidden for } J'' = 0 \leftrightarrow J' = 0 \text{ and } \Omega'' = 0 \leftrightarrow \Omega' = 0$$

$\Delta J = 0$ is only possible when the electronic orbital angular momentum is changed during the transition, i.e. $\Delta\Lambda = \pm 1$. This implies that for transitions between Σ states $\Sigma \leftrightarrow \Sigma$ the rotational selection rule is $\Delta J = \pm 1$ whereas for transitions between a Σ state and a Π state $\Sigma \leftrightarrow \Pi$ the rule is $\Delta J = 0, \pm 1$.

Selection Rules for Vibrational Wave Functions There are no strict selection rules for the case of a transition between different electronic states. For transitions between different electronic states, the Franck-Condon principle states that the transition probability is proportional to the FC factor which is the squared overlap of the vibrational wave functions of the involved states.

Hund's Case *b* Selection Rules

$$\Delta\Lambda = 0, \pm 1 \quad (3.31)$$

$$\Sigma^+ \leftrightarrow \Sigma^+, \Sigma^- \leftrightarrow \Sigma^-, \Sigma^+ \leftrightarrow \Sigma^- \quad (3.32)$$

$$\Delta S = 0 \quad (3.33)$$

$$\Delta N = 0, \pm 1 \quad \text{with the restriction } \Delta N \neq 0 \text{ when } \Sigma = 0 \rightarrow \Sigma = 0 \quad (3.34)$$

Hund's Case *c* Selection Rules

$$\Delta\Omega = 0, \pm 1 \quad (3.35)$$

The analogous rule to 3.25 in Hund's case *c* is

$$0^+ \leftrightarrow 0^+, \quad 0^- \leftrightarrow 0^-, \quad 0^+ \leftrightarrow 0^-. \quad (3.36)$$

Hund's Case *d* Selection Rules

$$\Delta N = 0, \pm 1 \quad (3.37)$$

$$\Delta L = 0, \pm 1 \quad (3.38)$$

$$\Delta\ell = 0 \quad (3.39)$$

3.3.3 Optical Transitions near 1550 nm

The spectroscopy laser operative in the present study has a tuning range from 1510 nm to 1580 nm, corresponding to 6623 cm^{-1} and 6329 cm^{-1} , respectively. In figure 3.3 the horizontal line labeled 1550 nm indicates which potentials can be reached with this laser from the loosely bound Feshbach molecules whose energy roughly corresponds to the (6S+6S) asymptote.

Only four potentials lie within the wavelength range of this laser: $0_u^-(P_{1/2})$, $0_u^+(P_{1/2})$, $0_u^+(P_{3/2})$, and $1_u(P_{1/2})$.

A transition to 0_u^- is dipole forbidden. This can be seen by taking into account that the two 0_u^- states arise from the ${}^3\Pi_u$ and ${}^3\Sigma_u^+$ states as indicated in figure 3.1. The lowest triplet state $a^3\Sigma_u^+$ cannot couple to these states due to the $u \leftrightarrow u$ selection rule and the singlet ground state $X^1\Sigma_g^+$ cannot couple due to the $\Delta S = 0$ selection rule. The figure also indicates that loosely bound electronic ground state levels correspond to 0_g^+ , 0_u^- and 1_u , none of which can couple to 0_u^- .

All the potential curves that reach this far down exhibit *ungerade* Symmetry. From the selection rule in bound-bound spectroscopy that a photon couples a *g* state to a *u* state and vice versa, one can see that these states can only be reached from the singlet ground state ${}^1\Sigma_g^+$. As discussed above, Feshbach molecules do not have definite *g/u* symmetry, so they can be assumed to have a *g* component. If a statistical mixture of singlet and triplet states is assumed, the singlet component would be 25%. In reality, the singlet component of the Feshbach molecules is state dependent and also *R* dependent and must be calculated from a coupled channels calculation. Such calculations are currently under way, as discussed in sections 5.3.1 and 6.1.1.

The $1_u(P_{1/2})$ state arises from the $B^1\Pi_u$, the $2^3\Sigma_u^+$ and the $b^3\Pi_u$ states. These states exhibit ungerade symmetry and can therefore be reached from the singlet ground state

3 Molecular Structure

which has gerade symmetry or from the 0_g^+ component of the ground state wave function. However, only the $B^1\Pi_u$ component fulfills the electron spin selection rule 3.27. This constitutes a transition with $\Delta\Lambda = 1$. Therefore, it can be reached with σ -polarized light. However, the excited state region reached with the $1.55\ \mu\text{m}$ laser is far below the bottom of the $B^1\Pi_u$ well in a region where it is more adequate for the 1_u state to consider the Born-Oppenheimer Potentials instead of the relativistic potentials, see section 6.2.2. Moreover, in order to exploit this state for a transfer to the absolute ground state, the singlet component afforded by the B state is required.

The 0_u^+ states arise from spin-orbit coupling between the $A^1\Sigma_u^+$ and $b^3\Pi_u$ states as discussed in detail in section 3.2.2. Excitation can only occur via the $A^1\Sigma_u^+$ component because the singlet ground state can only couple to the singlet excited state. This means that the transition effectively corresponds to a $\Sigma \leftrightarrow \Sigma$ transition which requires π polarized light. The contribution from the $A^1\Sigma_u^+$ state varies between 35% and 80% in the range of vibrational levels that can be reached with our laser [Bou06]. Perturbation effects present in these states were discussed in section 3.2.2. Our collaborators in Orsay have calculated the energies of the vibrational states in the 0_u^+ potentials based on ab initio potential curves. This gives a good estimate of the spacing between the individual levels but leaves some uncertainty in the absolute energy of the states which is comparable to the spacing between individual vibrational levels [Koc06a]. The lowest vibrational level in the $0_u^+(P_{3/2})$ state can be shifted to the spectroscopic value of Vergès and Amiot [Ver87] who analyzed the $A^1\Sigma_u^+$ state by Fourier transform spectroscopy. Currently, the theoretical potential curves are being adjusted to the available experimental data [Dul06]. In order to circumvent the uncertainty in the theoretical calculations, we decided to do a coarse scan of a wavelength region that spans more than the expected spacing between individual excited state vibrational levels. In the $1.52\ \mu\text{m}$ wavelength region, individual states are separated by up to $\sim 7\ \text{nm}$ in the 0_u^+ potentials.

CHAPTER 4

Experimental Setup

This chapter gives a description of the laser system for optical spectroscopy of ultracold Cs-dimers. We are interested in spectroscopy of ultracold Cs₂ Feshbach molecules in the wavelength region around 1.55 μm in order to explore a possible route for the production of a stable molecular ground state BEC by means of coherent population transfer to the rovibrational ground state in a two-photon process. The spectroscopy laser is a commercial tunable external cavity diode laser with a tuning range from 1510 nm to 1580 nm. As detailed in this chapter, control over the wavelength of the spectroscopy laser was implemented in the present work at various levels of accuracy.

In order to enable coarse searching for optical transitions with reproducible wavelength settings, a stabilization to the output of a wavemeter was implemented as detailed in section 4.1.4. Obviously, the accuracy of such a “lock” is limited by the resolution of the wavemeter.

For precise stabilization and frequency control of the spectroscopy laser, a locking scheme was developed with the aim to reach a reproducibility of the frequency settings in the sub-MHz range while maintaining full tunability of the laser. The scheme relies on a scanning optical resonator. The position of the transmission resonances of the spectroscopy laser are determined relative to the resonances of a reference laser that is stabilized to an atomic Cs transition. The spectroscopy laser is prestabilized with a second optical resonator by the Pound-Drever-Hall method. Feedback from the frequency measurement via the scanning resonator is on the piezoelectric actuator of the prestabilization resonator. The stabilization scheme is discussed in section 4.2.

Ultracold Cs atoms are prepared in a series of optical cooling and trapping steps in the Cs-BEC machine or LevT, as we like to call it for historical reasons. Ultracold molecules are created by means of a magnetic field ramp across a magnetically tunable Feshbach resonance, as discussed in section 2.2.3. Sample preparation and the integration of the spectroscopy setup into the Cs-BEC experiment are discussed in chapters 5.1 and 5.2, respectively. The Feshbach molecules are trapped in a quasi-electrostatic optical trap formed by CO₂ lasers. The trapped molecules are then exposed to the spectroscopy laser light and loss of Feshbach molecules as a function of spectroscopy laser frequency is monitored by destructive absorption imaging. The spectroscopy laser frequency is kept constant during the interaction time and then stepped with each experimental run. This is in contrast to many conventional spectroscopic experiments, where the laser frequency can be scanned continuously. One experimental run takes on the order of 30 seconds. Figure 4.1 shows the main part of the optical spectroscopy

4 Experimental Setup

setup. The CS-BEC experiment is depicted in figure 5.2.

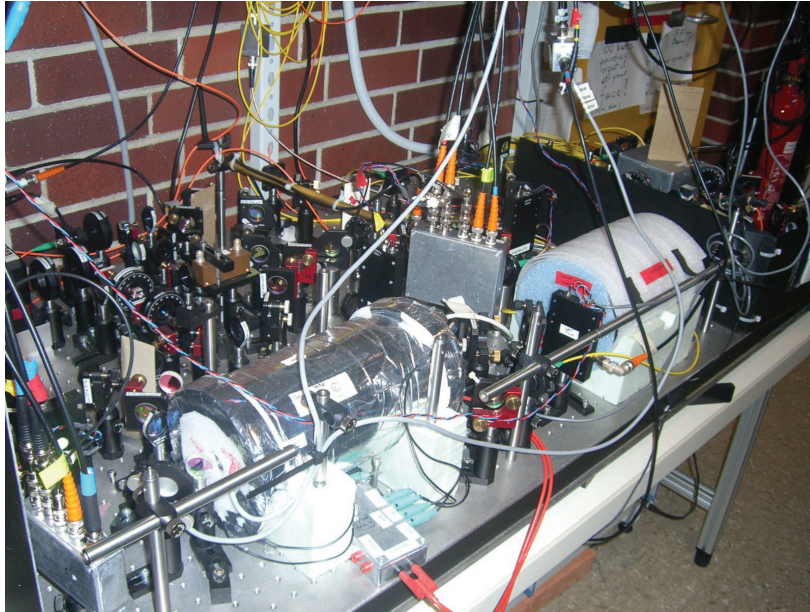


Figure 4.1: Optical setup: In the foreground, the casings of the two optical resonators that are operative in the stabilization scheme can be seen. The spectroscopy laser is situated in the background on the left. The reference laser for the stabilization scheme and for the wavemeter is situated on the far right side behind the black shielding. The wavemeter is not shown.

4.1 The Spectroscopy Setup

A schematic representation of the spectroscopy setup is given in figure 4.2. A wavemeter is used to measure the wavelength of the spectroscopy laser. Part of the spectroscopy laser's light is coupled into two different optical resonators, often referred to as optical cavities, that are used for the tunable frequency stabilization scheme and provide much finer control of the laser wavelength than would be achievable with the wavemeter alone. The spectroscopy light is delivered to the Cs-BEC experiment via a single mode optical fiber. A second laser operating at a precisely known wavelength near 852 nm is used as a wavelength reference both for the wavemeter and for the resonator-based stabilization scheme. The reference light is -160 MHz detuned to the red from the $F = 4 \rightarrow F' = 5$ atomic hyperfine transition of the Cs-D₂-line. For adjustment of the spectroscopy beam in the Cs-BEC experiment as detailed in section 5.2.1, resonant light is coupled into the optical fiber that delivers the light to the Cs-BEC experiment in addition to the spectroscopy light.

The individual components will be discussed in the subsequent sections.

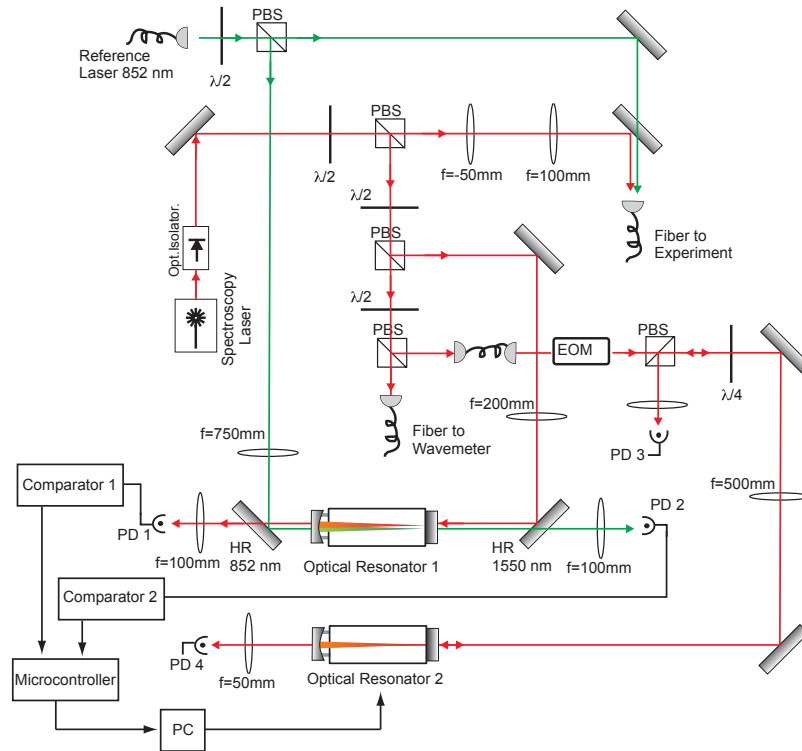


Figure 4.2: Optical stabilization setup: After passing through an optical isolator, the spectroscopy laser light is coupled into an optical fiber to the Cs-BEC experiment. A small fraction of the light is launched into a fiber to the wavemeter. Resonator 2 serves as prestabilization resonator by means of a Pound-Drever-Hall lock. Resonator 1 is used for the "Scanlock" described in section 4.2.3 and receives reference light from a 852 nm laser stabilized to an atomic hyperfine transition in Cs. The spectroscopy laser and reference laser transmission signals of Resonator 1 are fed into a microcontroller-based feedback circuit that acts on the prestabilization resonator. Polarizing beamsplitter cubes (*PBS*) in combination with $\lambda/2$ -plates are used to adjust beam powers. *HR*: high reflectivity dielectric mirrors, *PD*: photodiode, *PC*: control computer.

4.1.1 Spectroscopy Laser

For optical spectroscopy of our Cs₂-Feshbach Molecules, we chose the wavelength region around 1550 nm for the reasons outlined in the introduction. One practical advantage of this wavelength band is the availability of commercial, widely tunable, highly stable laser systems for the telecommunications industry. In the present study a Velocity tunable laser system from New Focus (San Jose, CA, USA), Model 6328 was used. This is a Littman-type external cavity diode laser system [Lit78b, Lit78a, Kiu81, Lit84, Day93] that offers a mode-hop free tuning range from ~ 1510 nm to 1580 nm at output powers around 20 mW. The laser is specified to a linewidth of < 300 kHz at 50 msec and < 5 MHz at 5 sec.

4 Experimental Setup

The laser can be conveniently controlled by a controller unit that supports manual front panel control as well as external control of all laser parameters. External control is via analog inputs or from a personal computer via RS232 or GPIB.

The laser wavelength can be addressed in several ways. A DC-motor offers a tuning resolution of 0,02 nm. Fine tuning can be done by means of a piezoelectric transducer that offers a tuning range of 30 GHz (0,24 nm). Both of these act on the position of the feedback mirror of the Littman extended cavity design. One “slow” and one “fast” current modulation input enable locking of the laser to an external reference such as an optical resonator.

A Labview Program was written that allows for convenient control of all laser parameters via RS232.

An optical isolator (Model #I-15-LM-SD-1.4-4, Isowave, NJ, USA, 60 dB optical isolation at 1550 nm) prevents optical feedback from backreflections into the laser.

4.1.2 Reference Laser

A reference laser with precisely known wavelength is used as a wavelength reference both for the wavemeter and for the stabilization of the spectroscopy laser. The reference laser is stabilized to the master laser of the LevT experiment. This master laser is locked to the $F = 4 \rightarrow F' = 5$ hyperfine transition of the Cs D_2 -line by modulation-transfer saturation spectroscopy [Raj79, Ber01] with a frequency aberration of less than 100 kHz. This hyperfine transition corresponds to a vacuum wavelength of 852.35638271 nm [Ste03]. The actual operation frequency of the master laser is -160.000 MHz red detuned from the atomic hyperfine transition due to a frequency shifting by a double-pass acousto-optical modulator, resulting in a reference wavelength of 852.3567677 nm. The reference laser used in this work is a home built diode laser (laser diode: JDSU SDL-5420) stabilized to the master laser using the “injection lock” technique [Sie86, Ger99]. Figure 4.3 shows the optical setup. After collimation and polarization rotation the beam is shaped by an anamorphic prism pair. It then passes through an optical isolator (Isowave, Model I-80-T4-H, 40 dB isolation). The optical isolator is equipped with exit ports for each of the two polarizers. This is used for injection-locking as described below. The polarizing beamsplitter cube directly after the optical isolator delivers a small amount of light to a simple saturation spectroscopy setup on a Cs-vapor cell that is used to monitor the performance of the lock. The main part of the output power is coupled into two polarization maintaining single-mode optical fibers (PM780-HP, Nufern, CT, USA) delivering reference light to the wavemeter and to the stabilization setup for the spectroscopy laser.

The output power of the reference laser is up to 150 mW. It is usually operated at 110 mW.

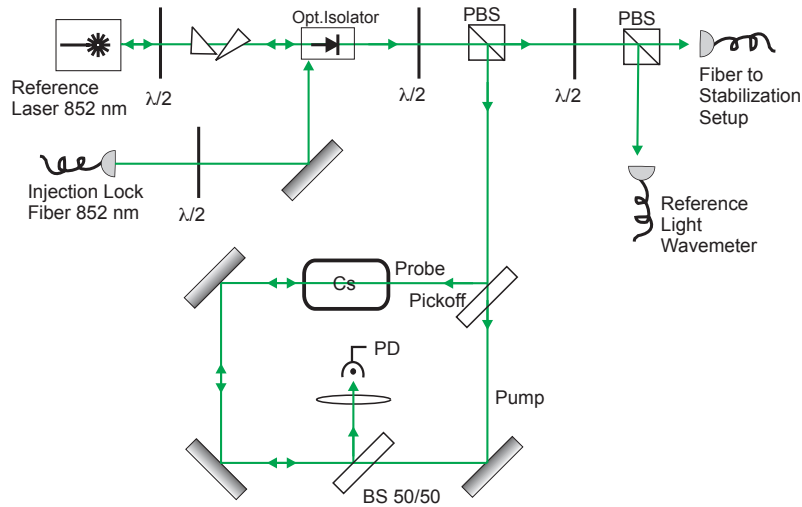


Figure 4.3: Optical setup for reference laser: The reference laser is operated as a slave laser which is injection locked to the maser laser of the LevT experiment. The locking light is delivered by an optical fiber labeled *Injection Lock Fiber* and enters through the distal exit port of the optical isolator. In the master laser setup there is a polarizing beamsplitter cube set to maximum transmission right before the injection lock fiber (not shown in the figure). Optimization of the $\lambda/2$ -plate shown after the injection lock fiber, i.e. of the polarization of the locking light, is straightforward by optimizing for maximum transmission of the slave laser light through that polarizing beamsplitter cube. The reference laser is monitored by standard saturation spectroscopy. The reference light serves for the wavemeter and the spectroscopy laser stabilization setup. *PBS*: Polarizing beam splitter cube, *BS 50/50*: beamsplitter plate.

Injection Lock

For injection locking the laser diode is brought close to the desired wavelength by tuning the temperature stabilization of the laser and by adjusting the laser diode current. A small amount of "locking light" (typically a few hundred μW) is then coupled into the laser diode through one of the exit ports of the optical isolator. This leads to stimulated emission at the frequency of the locking light and forces the laser to adopt the spectral properties of the master laser [Ger99]. The locking light is delivered to the setup through a single mode polarization maintaining optical fiber (PM 780-HP, Nufern, CT, USA). The fiber delivers roughly 1.5 mW of optical power, which makes alignment and mode matching rather uncritical, since much less optical power is actually needed to lock the laser. Mode matching is achieved by first overlaying the master laser beam with the output from the optical isolator's distal exit port. The slave laser beam is then coupled into the optical fiber that provides the master laser light. A $\lambda/2$ -plate is introduced between the optical isolator exit port and the optical fiber in order to align the direction of polarization of the locking light with the inherent direction of polarization of the slave diode.

4.1.3 The Wavemeter

The wavemeter, also known as lambdameter or wavelength meter, used in this study is a Michelson interferometer with varying path length in both arms of the interferometer [Hal76, Kow78], as illustrated in figure 4.4. This device is standard in our laboratories as described in reference [Bla00]. Normally, a helium-neon (He-Ne) laser serves as reference laser. It is stabilized to its gain profile by polarization stabilization where the laser resonator length is kept constant by comparing the intensity of two neighboring laser modes that are operative at the the same time and have orthogonal polarization. The reference beam is divided on a beamsplitter, providing the two arms of the interferometer. In both arms, there is a corner-cube retroreflector that is mounted on a cart moving back and forth at roughly constant velocity on an air-rail. The beams are reflected about one centimeter below the incoming beam and recombined again on the beamsplitter. This generates a temporal interference signal in the 100 kHz range. The signal is detected on photodiodes and the number of zero crossings per unit time is determined by a microcontroller.

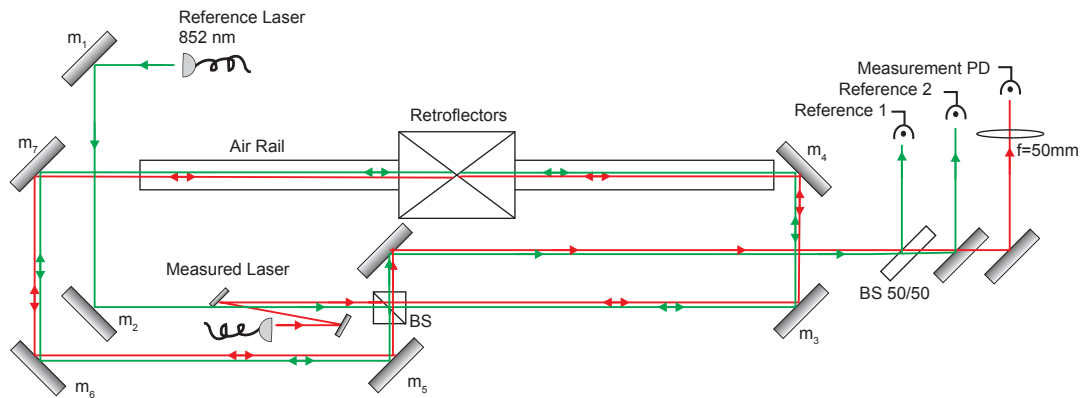


Figure 4.4: Optical setup wavemeter: Details are given in the text. The back-to-back corner-cube retroreflectors move back and forth along the air rail at roughly constant velocity driven by an electromagnet on one side of the rail. $m_1 - m_7$: mirrors. BS : broadband nonpolarizing beamsplitter cube. $BS\ 50/50$: beamsplitter plate.

The laser whose wavelength is to be measured is coupled into the wavemeter through a single-mode optical fiber and travels the same optical path but in the reverse direction. Therefore, the output beam of the measured light exits above the reference output and can conveniently be detected on a separate photodiode. The wavelength λ_x of the measured laser can be calculated from the relation

$$\lambda_x = \frac{N_{Ref}}{N_x} \lambda_{Ref} \quad (4.1)$$

where N_{Ref} is the number of zero crossings of the reference laser signal and N_x is the number of zero crossings of the measured laser for a certain measurement time. The

uncertainty in the counting procedure is reduced by the Vernier coincidence counting method where the starting and stopping of a counting period is only triggered if zero crossings from both the reference and the measured laser coincide within a time period of $\sim 1/100$ the period of the reference laser interference signal, reducing the relative error of this comparative measurement by a factor of 100. This device normally reaches a relative uncertainty of 10^{-7} .

Alignment instructions are given in appendix C.

Limitations

Several factors limit the accuracy of the Michelson Lambdameter.

For absolute wavelength measurements it has to be calibrated by measuring laser light of precisely known wavelength. A systematic error is introduced if the reference light and the light whose wavelength is to be measured are not exactly aligned but intersect at a finite angle. This leads to different optical path differences for the reference laser and the measured laser when the cart is moving. This error can be eliminated by calibration measurements.

The reference laser in the standard device is a He-Ne laser that has about 3 MHz rms short term stability on a time scale of seconds. The long-term drift is around 10^{-8} per year in the optimal case.

The device is operated in air. Dispersion effects introduce a systematic error, especially in our case where the reference wavelength and the measured wavelengths differ widely. In addition, day-to-day variations in ambient temperature, humidity and pressure can make a prominent contribution to the dispersion error exceeding the stated uncertainty of 10^{-7} .

If the device is not set up in an optimal way, further technical contributions to the error such as vibration of the cart near the turning points can compromise measured values.

There is a (small) phase error due to the curvature of the wavefronts of Gaussian beams that can be reduced by using large beams.

Modifications with Respect to Standard Wavemeters

The following modifications to our standard wavemeter design were made for the present project:

- The He-Ne reference laser was replaced by the 852 nm reference laser described in section 4.1.2. In contrast to the He-Ne laser, the wavelength of the 852 nm reference laser is precisely known. Its long-term stability is 100 kHz, which is superior to the estimated 10 MHz long-term stability of the He-Ne laser.
- The existing LabView Program that reads out the wavemeter data via RS232 was modified to account for the change from the He-Ne reference to the 852 nm laser and to compensate for the systematic error introduced by the dispersion of

4 Experimental Setup

air. The quantity $\frac{N_{Ref}}{N_x}$ from equation 4.1 is determined in air by the wavemeter. The wavelength of the spectroscopy laser in ambient air is calculated by multiplying $\frac{N_{Ref}}{N_x}$ with the wavelength of the reference laser in air calculated from its known vacuum wavelength and the corresponding refractive index of air. Temperature, air pressure and humidity in the laboratory are continuously monitored and transmitted to the control computer (WS444PC, Conrad Electronics, Germany). The refractive indices of air both for the reference laser and for the spectroscopy laser are calculated from these measured values and the actual wavelength readings. The equation used for this calculation is a modified Edlén equation [Edl66, Bir94] as used in the NIST “Engineering Metrology Toolbox” [Sto06]. It provides a sufficient level of accuracy and is simpler than the Ciddor equation [Cid96]. The refractive index is then used to calculate the vacuum wavelength of the spectroscopy laser.

- The reference light is coupled into the wavemeter through a polarization maintaining single-mode optical fiber (Nufern PM780-HP). Light of the spectroscopy laser is delivered through a polarization maintaining single mode fiber (Nufern PM1550-HP). The fiber termination is 8° angled at the connector where the spectroscopy laser is launched into the fiber (FC/APC) and straight on the wavemeter side. The straight fiber connector minimizes wavelength-dependent beam deviations that would cause systematic errors in the wavelength measurement. An achromatic outcoupling lens is used (ACH-NIR6x12 NIR-II, Edmund Optics, Karlsruhe, Germany). The wavemeter optics are adjusted to the wavelength region around 1.55 μm in order to minimize the amount of spectroscopy laser light that has to be allocated to the wavemeter. A broadband nonpolarizing beamsplitter cube (BS015, Thorlabs, N.J., USA) for 1100 nm - 1600 nm is used.

The accuracy is currently limited by non-ideal mechanical motion of the cart which causes dips in the wavelength reading near the turning points of the cart of ~ 50 MHz amplitude. These can either be corrected for by optimizing the mechanical setup, by averaging over several measurements or by excluding these regions of the air rail by additional light barriers.

Comparison Measurements with Commercial Wavelength Meter

We have not yet performed reference measurements in the 1.55 μm region as discussed in section 6.1.2 because at the current stage of the experiments we can tolerate a systematic offset in the wavelength measurements as long as they are reproducible. A comparison measurement with a commercial wavelength meter (WS6IR, HighFinesse, Tuebingen, Germany) was performed. This device is specified to an absolute accuracy of 500 MHz. Measured wavelengths agreed within this tolerance.

4.1.4 Lock to the Wavemeter

The spacing between individual vibrational states in the excited state region reached with the 1.55 μm spectroscopy laser is between 1 nm (125 GHz) and 7 nm (875 GHz). Our collaborators in Orsay [Bou06] have calculated the expected binding energy of the vibrational levels in the coupled 0_u^+ potentials based on ab initio potential curves calculated by Spiess and Meyer. The energy of the lowest vibrational level in the $A^1\Sigma_u^+$ state (see section 3.2.2) is adjusted to the spectroscopic knowledge from classical laser spectroscopy [Ver87] but the shape of the potentials is not adjusted to the spectroscopic data. Consequently, even though the spacing between individual vibrational levels is fairly well known from the calculations, the absolute energy of the levels can be regarded only as an estimate. Accordingly, a region larger than the expected spacing between consecutive levels must be scanned when looking for a molecular transition. Each experimental run takes on the order of 30 seconds. When searching for a molecular transition it is not manageable to step the spectroscopy frequency through such a wide range with MHz resolution as would be possible with the stabilization scheme discussed in section 4.2. For coarse searching for optical transitions, a computer-based “lock” to the wavemeter was implemented. This merely serves to make the wavelength settings reproducible during coarse searching since the laser’s inherent wavelength reproducibility is only on the order of 0.1 nm. The wavemeter lock has a resolution of 10^{-7} and relies on feedback to the stepping motor and the piezoelectric actuator (PZT) of the Littman mirror in the laser head. The wavemeter yields a wavelength measurement every few hundred msec, so it is clear that this “lock” can only enhance reproducibility and the laser displays its free-running time averaged spectral width of a few MHz.

The stepping motor is addressed by computer control via RS232 and the piezo by the analog frequency modulation input of the laser. The program is implemented in LabView, analog voltages are generated using a PCI-6221 device from National Instruments (TX, USA) that enables analog output with 16 bit resolution.

The program receives the setpoint from the main control computer of the LevT experiment via UDP and reads out the vacuum wavelength of the spectroscopy laser. For large detunings, a digital PID controller acting on the stepping motor is used. Once the wavelength is within the range manageable by the Littman-PZT (30 GHz), the laser enters a more stable mode of operation (local mode) and a second digital PID controller acting on the PZT becomes operative. Feedforward on two levels is implemented: If a new wavelength setpoint differs from the actual wavelength value by more than a certain amount, the laser is set to that wavelength and the PID output is suppressed until the laser is close to the desired wavelength. This is advantageous because the wavemeter produces large spurious “spikes” in the wavelength reading if the wavelength of the measured laser is changed rapidly. A second level of feedforward is used for the finer PZT-based servo component: When the piezo integrator is close to its maximum allowed level, the integrator is reset and the stepping motor is driven to a new value compensating for the piezo step. Again, the PID output is suppressed

4 Experimental Setup

during that time.

All relevant parameters are saved in a wavemeter log file. Data is stored during the time when the spectroscopy light is actually switched on including some additional margin before and after. This margin is usually set to two seconds before opening of the shutter until 2 seconds after closing the shutter, which gives 6 or 7 datapoints. Data storage is triggered by one of the Adwin timer cards controlling the Cs-BEC experiment

An online analysis calculates the mean and the standard deviation of these wavelength measurements and combines the mean wavelength for a given experimental run with the particle number measured by absorption imaging.

Modulation of the Laser for Coarse Searching

The spectroscopy laser is specified to a linewidth of 5 MHz within 5 seconds. When doing a coarse search for optical transitions, it is convenient to artificially increase this linewidth by sweeping the laser by a small amount while the spectroscopy beam is irradiating the molecules. The idea is to scan the laser wavelength on the order of the wavelength step size from one experimental run to the next in order to avoid “gaps” of wavelengths that are not sampled during the coarse search. The drawback of this method is that the effective spectral intensity of the spectroscopy laser is reduced by a factor given by the ratio of the linewidth of the excited state divided by the scanning interval.

A simple analog circuit sums the PID output of the wavemeter lock and the output of a function generator that provides a linear voltage ramp. The function generator is triggered when the spectroscopy light is turned on. The available optical resonators with known free spectral range can be used to calibrate the amplitude of the wavelength sweep. The sweep amplitude is chosen to be somewhat larger than the wavelength steps between individual experimental runs in order to assure some overlap between consecutive measurements. Typically, the sweep amplitude is chosen to be 700 MHz, whereas the wavelength stepsize is 500 MHz.

The output of the PID controller can be kept constant during the sweep in order to avoid wavelength steps.

4.2 Stabilization Scheme

The requirements for the spectroscopy laser stabilization scheme can be stated as follows: Each run of the Cs-BEC experiment evaluates one spectroscopic frequency that should be automatically programmable from the main control computer with a reproducibility that lies in the sub-MHz range. The full tuning range of the spectroscopy laser should be maintained. While the ultracold molecular sample is prepared, the controller has about 20 seconds to reach the setpoint. Then the spectroscopy beam is turned on for a certain amount of time during which the laser frequency has to remain

stable on a sub-MHz scale.

The implemented locking scheme relies on a combination of the classical Pound-

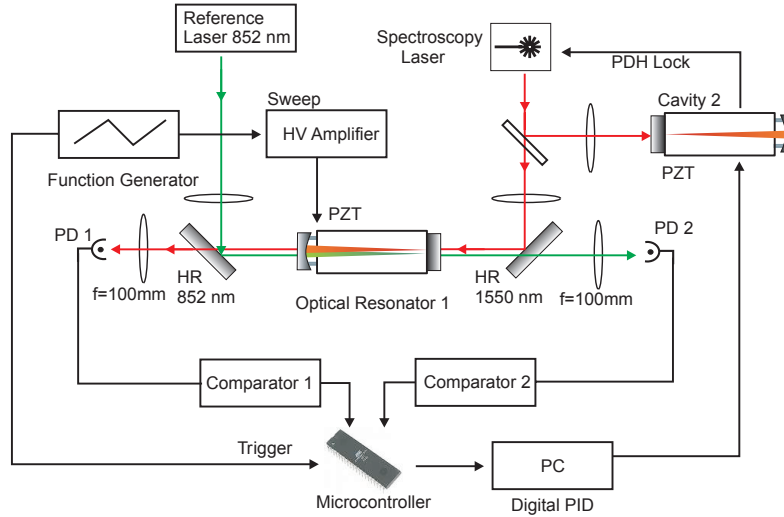


Figure 4.5: Scanlock setup: Both the reference laser and the spectroscopy laser are coupled into optical resonator 1. The function generator produces a linear voltage sweep that drives a high voltage amplifier that acts on one of the piezoactuators of optical resonator 1. A microcontroller then measures the time from the beginning of the sweep to the laser transmission peaks. A digital PID regulator acts on one of the piezoactuators of the prestabilization resonator (cavity 2) in order to regulate the position of the spectroscopy laser transmission peak with respect to the reference laser peaks.

Drever-Hall (PDH) lock to an optical resonator and a feedback circuit that acts on PZT of this prestabilization resonator.

The spectroscopy laser is prestabilized to an optical resonator (cavity 2 in figure 4.5) by the PDH technique as described in section 4.2.2. One of the mirrors of this prestabilization resonator is mounted on a piezoelectric transducer that changes the length of the optical resonator when voltage is applied to it. Therefore, the resonator's resonance frequencies can be shifted at will. The frequency of a laser locked to one of the modes of the optical resonator follows such a shift of the resonator modes. Since piezoelectric transducers show some degree of hysteresis, there is no strict correlation between the voltage applied to the resonator PZT and the mirror position. In addition, long term drifts of the optical resonator can shift the resonance frequencies.

In order to be able to precisely control the frequency of the prestabilized laser, a feedback scheme was developed that can be termed “scan lock scheme” as described in detail in section 4.2.3. In brief, both the spectroscopy laser and the 852 nm reference laser are coupled into a scanning optical resonator (resonator 1 in figure 4.5). The length of this resonator is modulated continuously by means of a piezoelectric transducer. Since the applied voltage ramp is linear, the voltage applied to the piezo is

4 Experimental Setup

linearly correlated with the time elapsed from the beginning of the sweep. The time intervals from the beginning of the sweep to the appearance of two resonances of the reference laser and of one resonance of the spectroscopy laser are measured by a microcontroller. The position of the spectroscopy laser resonance relative to the position of the two reference laser resonances is stabilized by applying feedback to the piezo-electric transducer of the prestabilization resonator.

4.2.1 Optical Resonators

Two largely identical optical resonators or “cavities” are operative in the stabilization scheme. A primer on resonator optics can be found in appendix B. There the concepts of free spectral range (FSR, ν_F) and finesse are discussed and a simple stability criterion for the design of an optical resonator is given. The position of higher, non-Gaussian modes has to be considered in order to avoid spectral overlap between the Gaussian (0,0)- mode and the higher transverse modes. Higher modes are equally spaced in frequency, see appendix B and table 4.2. This can be used to linearize the piezo motion in our scan lock scheme. The following section should give practical guidance for building an optical resonator.

Resonator Construction Details

We use optical resonators that consist of one curved and one flat mirror mounted on a spacer of 100 mm length that assures a stable distance between the mirrors. One of the mirrors can be moved along the axis of the resonator by means of piezoelectric transducers. The free spectral range is 1.5 GHz and the finesse is slightly below 1000 depending on the wavelength. The measured full-width-half-maximum resonance width at 852 nm is 1.894 ± 0.023 MHz. The optical characteristics of the resonators used in the present study are summarized in table 4.1.

Table 4.2 gives the frequency shifts of the first few transverse modes (l, m, q) for given q relative to the frequency of the (0, 0, q)-Gaussian mode (see appendix B). Here, q indicates the longitudinal mode number whereas the labels l, m refer to the transverse modes. The values given are specific for the optical resonators in the present setup, units are in terms of the free spectral range. It can be seen that none of the higher modes lies close to the Gaussian (0,0)-mode.

The mirrors were custom coated by Layertec GmbH, Mellingen, Germany. The coating is specified to a reflectivity of 99.7% for the 852 nm reference laser and for the spectroscopy laser in the range from 1510 nm to 1580 nm. From measured mirror transmission it can be inferred that reflectivity is slightly lower, decreasing the calculated finesse to 800-1000, depending on the actual wavelength. The mirrors are 30° wedged and anti-reflection coated on the back surface. Surface quality is specified to $\lambda/10$ for the flat surfaces and to $\lambda/4$ for the curved surfaces.

To keep the mirrors at a precisely determined distance they are mounted on a spacer. The spacer was purchased from Hellma Optik (Jena, Germany). It has a length of 100

length	100 mm
FSR ν_F	1,5 GHz
mirror 1 curvature radius	-250 mm
mirror 2 curvature radius	∞
Wavelength region	852 nm and 1480 nm - 1670 nm
mirror reflectivity	99.6 – 99.7%
finesse (calculated)	800 – 1000
waist 852 nm flat mirror	0.182 mm
waist 1550 nm flat mirror	0.246 mm
waist 852 nm curved mirror	0.235 mm
waist 1550 nm curved mirror	0.317 mm

Table 4.1: **Optical resonator parameters:** Optical characteristics of the resonators used in the present study. The wavelength range is taken from the measured transmission of the mirrors where the transmission stays below 0.4%. The finesse stated is calculated from the transmission of the mirrors measured in the tuning range of the spectroscopy laser. Mirror transmission is 0.3% at 852 nm, corresponding to a calculated finesse of 1000.

$l + m$	$(\nu_{l,m,q} - \nu_q)/\nu_F$	$l + m$	$(\nu_{l,m,q} - \nu_q)/\nu_F$
1	0.218	4	0.872
2	0.436	5	1.09
3	0.65	6	1.308

Table 4.2: **Higher resonator modes:** Frequency shift of the transverse modes for given q relative to the frequency ν_q of the $(0, 0, q)$ -Gaussian mode in units of the FSR for the resonators used here ($d=100$ mm, one flat mirror, one concave mirror with 250 mm radius of curvature). The frequency of the $(1, 0, q)$ mode is $\nu_{1,0,q} = \nu_q + 0,218 \cdot \nu_F$.

mm and a quadratic cross section of 30 mm x 30 mm with a central bore of 10 mm. A hole on the side connects the bore with the outside in order to allow for pressure equilibration. One of the end faces features a hollow of 20 mm diameter that is 5 mm deep for the inner ceramic ring of the piezo construction discussed below.

Zerodur (Schott AG, Mainz, Germany) was chosen as spacer material because it features a nominal thermal expansion coefficient of zero. Expansion class 0 has the tightest tolerances and is specified to a thermal expansion coefficient of $0 \pm 0.002 \cdot 10^{-6} K^{-1}$. A viable alternative to Zerodur is ULE (“ultra low expansion”) material from Corning (NY, USA). Zerodur has the disadvantage of showing some residual material relaxation, which ULE does not. In the present stabilization scheme such a long term drift can be corrected for and consequently Zerodur was chosen because of its lower price. The flat mirror is glued directly to the spacer with ultraviolet light (UV)-curing glue (OP-66 LS, Dymax, Frankfurt, Germany) that features low contraction during curing. Care was taken not to introduce glue between the mirror and the spacer, glue was applied on the side of the mirror in several individual spots. This assured that the axis of

4 Experimental Setup

the resonator is defined by the parallelism of the spacer's end faces and that the superior thermal characteristics of the spacer material were not counteracted by a layer of glue.

The concave mirror is mounted on an assembly of two piezoelectric actuators. Both piezos are tubes made from Pz27 (Ferroperm, Kvistgaard, Denmark). An outer tube (outer diameter: 24 mm, inner diameter: 22.4 mm, length: 4 mm) is glued directly to the end face of the resonator. This piezo holds a ceramic ring custom made in our workshop from macor ceramic material (RS components, Austria). A smaller inner piezo ring (outer diameter: 18.3 mm, inner diameter: 16.7 mm, length: 4 mm) rests on this outer ceramic ring and holds a small inner ceramic ring. This in turn holds the curved mirror whose reflecting surface is thus flush with the end face of the spacer. Again, UV curing glue was applied as individual spots without introducing glue between the parts to be bonded. The thermal expansion coefficient of the piezoelectric material is much worse than the expansion coefficient of the spacer material. This nested construction assures that length drifts due to thermal expansion of the two piezos cancel each other out in first order. The macor rings do not contribute to thermal drifts in first order since they only bridge between the piezos or between the inner piezo and the mirror. This construction has been used in our group previously, a technical drawing can be found in reference [Kin05]. Figure 4.6 shows the piezo construction and the spacer.



Figure 4.6: Optical resonator piezos: *left:* Nested piezo construction before gluing the outer piezo ring to the spacer. The large ceramic ring is attached to the outer piezo and supports the inner piezo. This in turn holds the smaller ceramic ring that the mirror is attached to. *right:* Zerodur spacer with piezos attached.

The piezos were electrically contacted by soldering. The wall thickness of the piezos is 0.8 mm. Since the resonators are operated in air and high voltage discharges in air can be expected at an electric field of roughly 1 kV/mm, the voltage across the piezoelectric transducers should remain below 800 V.

For the 852 nm reference laser, one free spectral range of 1.5 GHz corresponds to 426 nm length change of the piezo actuator which is covered by applying roughly 250 V to the piezo. Similarly, for the spectroscopy laser, one free spectral range corresponds to approximately 450 V.

Pressure-tight Housing and Temperature Stabilization

Both optical resonators are contained in an air-tight housing that consists of a vacuum tube with inner diameter of 68 mm for resonator 1 and 60 mm for resonator 2 and length 126 mm. The tube is closed with CF blind flanges on both sides. Optical access is provided by a 1 inch diameter glass window in each of the flanges that is anti-reflection coated for 852 nm and tilted against the axis of the tube by 10 degrees on one resonator and 7 degrees on the other to avoid back reflections and etalon effects. The optical resonators are held in the vacuum tube by stable plastic mounts fixed by rubber rings made in our workshop, as shown in figure 4.7.

One of the flanges features two airtight voltage feed-throughs (HGP.0S.302.CLLPV, Lemo Elektronik) for the piezoelectric transducers.

The vacuum tubes of both resonators are actively temperature stabilized. The stabilization constantly heats the vacuum tube by means of resistive wire wound around it. The regulation thus keeps the vacuum tubes at constant temperature a few degrees above room temperature. Both vacuum tubes are passively isolated and placed in external metal containers. Figure 4.7 shows one of the optical resonators mounted inside the vacuum tube and the vacuum tube after closing with the temperature measurement circuitry attached and a first layer of passive isolation over the heating wire. For the

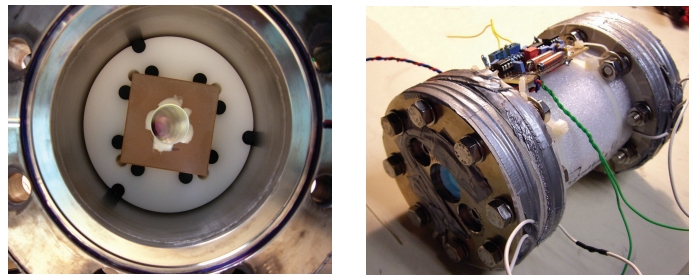


Figure 4.7: Optical resonator housing: *left:* View of the optical resonator inside the vacuum tube held by plastic mounts. *right:* Vacuum tube with temperature measurement circuitry. The flange in the foreground features a window and voltage feed-throughs. The heating wire is underneath the adhesive tape and the white isolation material.

scan lock resonator, there is a single active stabilization of the vacuum tube. For the prestabilization resonator, there is a dual active temperature stabilization, one servo loop acting on the vacuum tube and a further one keeping the additional outer metal container at constant temperature somewhat below the temperature of the vacuum tube. Both servo loops measure the temperature with independent measurement bridges.

Temperature sensing is done with a 100 k Ω NTC (B57891M104J, Epcos) glued to the respective metal parts with heat conducting glue (TBS, Electrolube). A second independent NTC on the vacuum tube can be used to monitor the temperature. A circuit diagram for the temperature measurement circuitry can be found in the appendix, see section D.1. By selecting appropriate resistors in the temperature measurement bridge,

4 Experimental Setup

the temperature set points are chosen to be $\sim 32^\circ\text{C}$ for the vacuum tubes and $\sim 28.4^\circ\text{C}$ for the outer casing of the prestabilization resonator. The bridge features a trimmer potentiometer that allows for adjustment of the temperature set point by roughly $\pm 1^\circ\text{C}$. The temperature PID regulator is based on a standard electronic design used in our group. The standard output power stage was replaced with the circuit shown in figure D.2 which is more convenient than the standard amplifier. The heating wire used (RD100/0.6, Block, Germany) has a resistance of $1.73\ \Omega/\text{meter}$ and was applied both to the vacuum tubing and to the flanges over a layer of electrically isolating heat resistant glass fiber tape (3M). Total resistance was $\sim 22\ \Omega$ for each temperature stabilization. Judging from the amplitude of the error signal, the temperature stabilization is stable to within 1 mK during an observation time of 10 hours.

We measured the drift of the prestabilization resonator by locking the spectroscopy laser to it and measuring its drift with the scanning resonator whose center position was stabilized to the reference laser as will be explained in section 4.2.3. We obtained a drift rate of $\sim 15\ \text{MHz}$ per hour for the prestabilization resonator. Resonance positions are reproducible on a day-to-day basis on this scale. The scan lock described below does not use this stability of the resonators as a reference but relies on the stability of the reference laser which has a frequency aberration of less than 100 kHz.

4.2.2 Pound-Drever-Hall Prestabilization

As outlined above, the locking scheme requires prestabilization of the laser to an optical resonator whose resonance frequencies can be tuned by means of a piezoelectric actuator. The standard method for locking a laser to an optical resonator is the Pound-Drever-Hall sideband locking scheme [Dre83]. Sidebands are modulated on the laser light. Essentially, the amplitude and phase of the different frequency components reflected from the resonator depend on their frequency difference with the resonance frequency, which results in an error signal.

The reflected beam is detected on a photodiode. The photodiode signal is then mixed by a phase detector with a local oscillator signal that. The modulation signal and the local oscillator signal have the same frequency and a fixed phase relation. This multiplication in the time domain yields the component of the photodiode signal at the frequency ω of the modulation signal. A low pass filter after the phase detector is used to suppress the signal at 2ω . The shape of the error signal as a function of detuning from the resonance frequency is dependent on the relative phase between the modulation signal and the local oscillator. One big advantage of the radiofrequency-sideband lock is that the detection process is shifted to high frequencies where the typical technical $1/f$ noise is suppressed. Note that the bandwidth of the lock is not limited by the photon storage time in the resonator, enabling high bandwidths even when locking to very high finesse resonators that have a long photon storage time.

The lock was implemented in such a way that the laser can be maintained in lock while the cavity's resonance frequencies are shifted by more than a free spectral range. This assures tunability of the lock. Figure 4.8 shows the optical setup of the PDH lock.

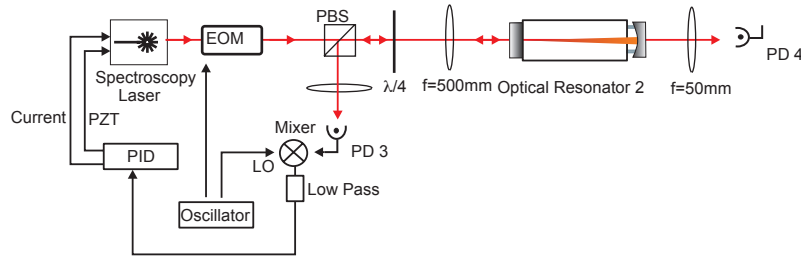


Figure 4.8: Optical setup of the PDH lock: The spectroscopy laser reaches this part of the setup through a single-mode optical fiber. The laser light is phase modulated in the EOM, reflected from the resonator and detected on a fast photodiode (PD3). A phase detector receives both the photodiode signal and a local oscillator signal and, in combination with a low pass filter, provides the error signal. Feedback is put on the laser diode current and laser piezo voltage.

The laser reaches this part of the spectroscopy setup through a polarization maintaining single mode optical fiber (PM 1550-HP, Nufern, collimator lens: Thorlabs C220-TM-C, $f=11\text{ mm}$). This assures that the beam has a Gaussian intensity distribution. Mode matching between the Gaussian beam and the optical resonator is achieved with a $f = 500\text{ mm}$ lens. The fiber's polarization axis is aligned in such a way as to provide maximum modulation in the electro-optic modulator (EOM). The EOM is directly driven at 30 MHz by a RF amplifier at a power of 25 dBm. The sidebands have a measured height of $\sim 3\%$ of the carrier. The polarizing beamsplitter cube in combination with the $\lambda/4$ -plate serves to separate the beam reflected by the cavity from the incoming beam. The reflected beam is detected on a photodiode. The photodiode has a bandwidth of 125 MHz and is DC coupled. In order to prevent saturation of the radio frequency (RF) mixer, a capacitor in series with the photodiode signal is used to cut off the DC component of the signal. The phase detector (MiniCircuits ZRPD-1) receives 7 dBm of local oscillator power. The low pass filter (MiniCircuits BLP-1.9) has a 3 dB rolloff at 1.9 MHz. The parameters are such that the amplitude of the error signal is limited by the laser intensity incident on the cavity. Typically, the peak-to-peak amplitude of the error signal is set to 800 mV.

The “laser PID” circuit is a standard electronic design in our lab and has a fast and a slow branch. The fast branch is a PI controller and modulates the laser diode current. The slow branch is a PID controller and acts on the piezoelectric transducer in the laser head. In order to enable the large tuning range of 2 GHz of this lock, the circuit was modified in the following way: The output of the fast PI branch was fed into the slow branch as input via a unity gain buffer operational amplifier with an optional low-pass filter. Therefore, the value of the fast integrator determines the output of the slow branch.

4 Experimental Setup

Problems Locking the Spectroscopy Laser

Several problems arose when locking the spectroscopy laser:

1. The gain of the analog frequency modulation input of the laser is too large for convenient locking to an external reference. This input acts on the PZT of the Littman setup. A voltage of ± 3 V corresponds to a frequency shift of 30 GHz. A 50 Hz voltage ripple of 2 mV due to ground loops already leads to a deviation of 10 MHz and suffices to drive the laser out of lock, since the frequency modulation range attainable by current modulation is on the order of 20 MHz. This problem was solved by inserting the voltage divider circuit shown in figure 4.9 between the laser PID controller and the frequency modulation input of the laser. The laser PID operates at its full ± 13.5 V range and the circuit combines a voltage divider with a low pass filter. The grounds of the PID circuit and the New Focus laser are decoupled by a $5\text{ k}\Omega$ resistor.

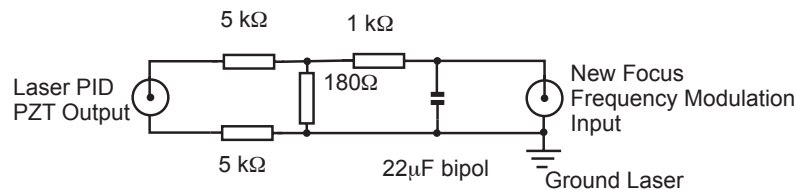


Figure 4.9: PDH lock voltage divider and low pass filter: Circuit that conditions the output of the laser locking PID circuit to account for the high gain of the laser's frequency modulation input.

2. When analyzing the frequency characteristics of the laser with the optical resonator, it was discovered that there are series of spikes on the resonator transmission signal. These were interpreted as short frequency spikes. A typical pattern is shown in figure 4.10. In between these series intervals of several msec without such spikes are present. The picture shows an oscilloscope trace of the resonator transmission signal with the free running laser tuned to the side of the cavity resonance peak. This problem is known for this particular type of laser and has been observed by other research groups as well, for example in the Ye group at JILA, Colorado [Ye06a]. The problem apparently arises from bad circuit layout with some crosstalk between the digital and the analog circuitry in the laser control unit. It is estimated that the amplitude of these frequency fluctuations is ~ 1 MHz. This poses a limitation for precision spectroscopy and would compromise coherent population transfer schemes.
3. The New Focus laser is specified to work single mode and without mode hops over the entire tuning range. However, we observe sudden transitions to multi-

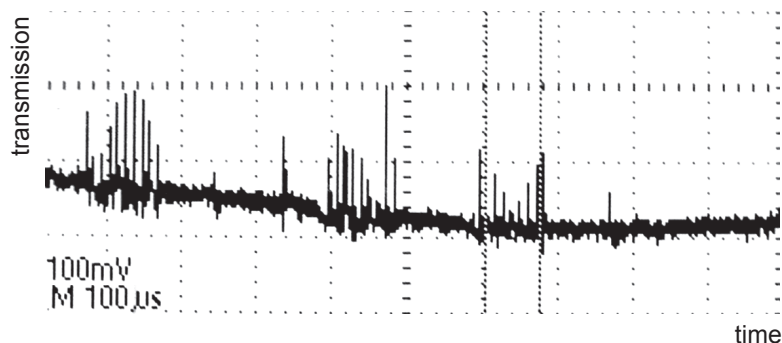


Figure 4.10: Frequency spikes of the New Focus laser: Trains of repetitive spikes when the free running laser is tuned to the side of the resonator transmission.

mode operation evidenced by a smeared-out transmission pattern when sweeping an optical resonator and disappearance of the temporal interference signal in the Michelson type wavelength meter. This can normally be corrected by changing the current or frequency settings. However, during periods of multimode operation, spectroscopy is not possible. This is especially inconvenient because the whole setup can normally be run in a completely automated way.

4.2.3 Scanlock

Setup

The basic idea of this locking scheme was already introduced on page 81. The setup is depicted in figure 4.5. Both the prestabilized spectroscopy laser and the 852 nm reference laser are coupled into an optical resonator. A function generator (Agilent 33220A) produces a linear voltage ramp that is amplified by a high voltage amplifier (PA-94, Apex, Tucson, AZ, USA) to an amplitude of ± 300 V. This is applied to one electrode of the piezoelectric actuator while the other electrode is biased to 300 V in order to keep the voltage across the piezo positive at all times. The voltage ramp translates into a length change of the optical resonator of approximately 800 nm. Such a sweep covers almost two free spectral ranges (FSR) for the reference laser and little more than one FSR for the spectroscopy laser, implying that two transmission resonances can be observed for the reference laser and one resonance for the spectroscopy laser.

The transmission signals for 852 nm and for 1550 nm are detected on separate photodiodes. Separation of the two wavelengths is achieved by means of the dielectric mirrors specific for the respective wavelength. Each of these photodiodes feeds one comparator circuit that converts the transmission peaks to square pulses of defined amplitude whose width is dependent on the magnitude of the reference voltage and on the slope of the voltage ramp. Circuit diagrams for the comparators are given in the appendix,

4 Experimental Setup

see section D.2.

A microcontroller measures the time intervals from the beginning of the resonator sweep to the appearance of each of the transmission peaks. The resonator sweep frequency is 50 Hz. This is described more fully on page 90 and depicted schematically in figure 4.11.

It is important to note that the frequency of the reference laser is fixed whereas the frequencies ν_q of the optical resonator modes can be adjusted by means of the temperature stabilization and the bias voltage across the resonator's piezoelectric transducers. Through active feedback the reference modes are maintained at a fixed position with respect to the resonator sweep, as described on page 92. The position of the spectroscopy laser transmission peak with respect to the resonator sweep depends on the "position" of the prestabilization resonator as determined by its temperature settings and the voltage applied to its piezos.

A digital PID regulator is used to stabilize the position of the spectroscopy laser peak relative to the position of the two reference laser peaks. The PID loop uses one of the piezoelectric transducers of the prestabilization cavity as actuator. The second PZT of the prestabilization cavity serves to place the modes of the prestabilization cavity at a convenient position relative to the modes of the scanning resonator (resonator 1 in figures 4.5 and 4.2).

The position of the spectroscopy laser transmission peak relative to the center between the first and the second reference laser transmission peak (C_{Ref} in figure 4.11) is largely independent of the sweep amplitude and period if the position is measured in units of the time that elapses between the first and the second reference laser transmission peak ($T_{FSR Ref}$) which is equivalent to one free spectral range.

Microcontroller

A microcontroller measures the time intervals from the beginning of the resonator sweep to the appearance of two reference laser transmissions and one spectroscopy laser transmission. The atmega162 microcontroller from Atmel Corp. is an 8-bit RISC processor and was chosen because it features two 16-bit counters with input capture units, external interrupts, more than sufficient RAM for an application like this and a convenient serial interface. The microcontroller is clocked by an external crystal at 16 MHz, yielding a time resolution of $0.0625 \mu\text{sec}$, which is not limiting the accuracy of the lock. To save development time, the microcontroller is operated on a slightly modified STK 500 board from Atmel with the inputs being decoupled by digital optocouplers (H11L1).

The development platform AVRstudio offers convenient simulation and debugging functionalities. The microcontroller program was written in assembler code in order to assure maximum control over each step of execution.

The commented assembler program can be found in the appendix, see section A. Figure 4.11 is a schematic representation of the stabilization and gives an overview of the time intervals measured by the microcontroller.

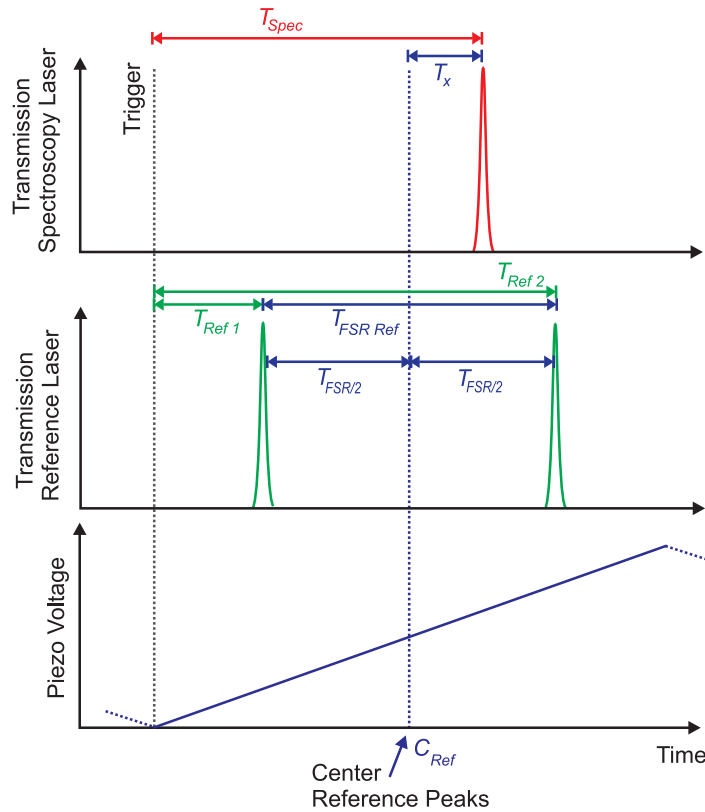


Figure 4.11: Scanlock schematic: Optical resonator transmission signal during one sweep of the scan lock resonator with definition of the timer values and time intervals as discussed in the text. The bottom panel shows the piezo voltage ramp that sweeps the resonator length. The top panel shows the transmission signal for the spectroscopy laser with one resonance peak. The center panel shows the transmission signal for the reference laser. The wavelength of the reference laser (852 nm) is much shorter than the wavelength of the spectroscopy laser (1550 nm), therefore two transmission peaks show up whereas for the spectroscopy laser only one resonance is present. The function generator provides a trigger signal at the beginning of the sweep. The microcontroller measures the time intervals T_{Spec} , $T_{Ref 1}$ and $T_{Ref 2}$. The center between the two reference laser peaks defines the reference point C_{Ref} for the stabilization. The stabilization scheme locks the position of the spectroscopy laser transmission relative to C_{Ref} . The setpoint is given in relative units $\frac{T_x}{T_{FSR Ref}}$, which makes the regulation largely insensitive to the amplitude and frequency of the resonator sweep. The mean resonator length is actively stabilized such that the C_{Ref} coincides with the middle of the resonator sweep.

Here, a summary of the program structure is given that should make it easy to understand the program. First, register names are defined and all required functionalities like stack pointer, external interrupts, the two 16-bit timers including their input capture units, and serial communication are initialized. One of the timers is used to measure time intervals for to the spectroscopy laser (T_{Spec} in figure 4.11), the other

4 Experimental Setup

timer those pertaining to the reference laser (T_{Ref1} and T_{Ref2} in figure 4.11). The processor then waits in a loop for the synchronization trigger that marks the beginning of the resonator sweep. This event is handled by an interrupt routine that sets the pointers that address the RAM to the memory addresses where the timer values are stored, erases all counter values from the previous run from the RAM and starts the timers. For each peak, the rising and the falling edge are measured in order to make a more accurate measurement of the peak position and in order to make the system more fail-proof. The events for the reference laser and the spectroscopy laser are handled by separate interrupt routines. These read out the input capture registers that contain the timer value for the input capture event. After detection of all peaks, the microcontroller exits the waiting loop and converts the measured binary timer values to ASCII-coded hex digits that are sent to the control computer over the RS 232 interface.

PID

The microcontroller transmits a string that contains the timer values for the rising and the falling edges of two reference laser peaks and one spectroscopy laser peak to the spectroscopy control computer every 20 msec via RS232.

A program implemented in LabView uses this data to regulate the position of the spectroscopy laser relative to the position of the reference laser transmissions. First, the individual timer values are extracted from the transmitted string. The timer values are given in units of the reciprocal processor frequency (16 MHz) stabilized by an external crystal. These counter values are then transformed into milliseconds. For each transmission peak, the center of the peak is calculated, which makes the peak position measurements less sensitive to the setting of the reference voltage of the comparators. Due to the hysteresis of the Schmitt-triggers, there is a small systematic shift in the direction of increasing times which is similar for all detected peaks.

From the two reference laser peaks (T_{Ref1} and T_{Ref2} in figure 4.11), the center between these two peaks C_{Ref} and the time interval T_{FSRRef} between them is calculated. The former serves as the reference point for the position of the spectroscopy laser peak while the latter defines relative units for the position of the spectroscopy laser transmission that are independent of the resonator sweep amplitude and period.

Regulation of the Resonator Center Position A first digital PID controller stabilizes the center (C_{Ref} in figure 4.11) between reference peak 1 (T_{Ref1}) and reference peak 2 (T_{Ref2}) to the middle of the sweep (e.g. to 5 msec for a sweep frequency of 20 Hz). This makes it easier to mathematically compensate for nonlinearities of the resonator sweep due to piezo hysteresis because it makes the system more reproducible. The regulation acts on the outer piezoelectric ring of the scan-lock resonator, whereas the inner piezoelectric ring is used for sweeping. An offset generated by a high voltage amplifier (PA-95, Apex) is applied to the positive electrode of the piezo ring. The output of the digital PID is applied to the negative electrode of the piezo ring by means

of a PCI-6221 analog I/O device from National Instruments.

This regulation compensates for the very slow drifts the optical resonator suffers.

Regulation of the Spectroscopy Laser Frequency A second digital PID regulator stabilizes the position of the spectroscopy laser transmission (T_X in figure 4.11) relative to the center C_{Ref} of the reference laser transmissions by acting on one of the piezoelectric transducers of the prestabilization resonator. The regulation receives its setpoint from the main control computer of the Cs-BEC experiment via UDP. Assuming a linear sweep of the resonator length, the setpoint is set in units of MHz shift relative to C_{Ref} according to the relation

$$\Delta\nu_{S_{pec}} = -\frac{\lambda_{S_{pec}}}{\lambda_{Ref}} * \frac{T_X}{T_{FSR_{Ref}}} * FSR \quad (4.2)$$

where $\Delta\nu_{S_{pec}}$ is the frequency shift of the spectroscopy laser, λ_{Ref} and $\lambda_{S_{pec}}$ are the wavelengths of the reference laser and of the spectroscopy laser, respectively. FSR is the free spectral range of 1.5 GHz while $T_{FSR_{Ref}}$ is the time interval between peak 1 and peak 2 of the reference laser.

The digital PID regulation is programmed according to the following relation:

$$PID_n = K_P * \left(\frac{T_{x_n}}{T_{FSR_{Ref}}} - S \right) + K_I * \sum_{k=1}^n \left(\frac{T_{x_k}}{T_{FSR_{Ref}}} - S \right) * dt + \frac{K_D}{dt} * \left(\frac{T_{x_n}}{T_{FSR_{Ref}}} - \frac{T_{x_{n-1}}}{T_{FSR_{Ref}}} \right) + K_S * S \quad (4.3)$$

where PID_n is the PID output, K_P , K_I , K_D and K_S are constants, T_{x_k} is the measured value in the k -th iteration and S is the setpoint. The last term constitutes some feed-forward which is not important.

Two filter routines are implemented in order to avoid erroneous activity of the servo in case a resonator transmission peak is not smooth and leads to more than one TTL pulse from the comparator circuit or in case transmission errors occur between the microcontroller and the control computer:

- A small subroutine tests the received RS232 string for the correct length and replaces it with the string from the last iteration if the length is not correct.
- For each of the transmission peaks a digital filter calculates a moving average of a selectable number of measurements. For each new measured value, the routine computes the deviation from this average. A threshold can be set for the deviation above which a certain measurement is discarded. This filters out spikes due to repetitive firing of the comparators.

Both mechanisms occur rarely during measurements if the settings for the electronics are correct.

One subroutine displays whether the laser is out of the PDH-prestabilization lock. The program indicates when the laser has reached the setpoint within a certain tolerance.

4 Experimental Setup

These two values together with the setpoint for the regulation are transmitted to the wavemeter program that saves this information together with the wavemeter data. In this way the wavemeter indicates which mode of the scan lock is operative whereas the microcontroller-based stabilization sets the laser frequency modulo the free spectral range of the scan lock resonator on a much finer scale than could be achieved with the wavemeter alone.

If the sweep of the scan lock cavity covers less than a free spectral range of the spectroscopy laser, the regulation could drive the spectroscopy laser out of the region that is covered by the scan. In this situation the microcontroller does not receive the expected interrupts and does not transmit data to the control computer. This constellation is detected by a watchdog timer in the program and corrected for by programmatically forcing the setpoint to zero. Similarly, if a setpoint is entered that drives the mode to be stabilized out of the scanned region and the next mode enters at the other end of the scan, a situation of positive feedback arises. Such a situation is also detected and corrected for. The PID output is converted to an analog voltage by an analog/digital I/O device (PCI-6221, National Instruments) with 16-bit resolution. Since the DC-DC converter (Hamamatsu C4900-50, Shizuoka-Ken, Japan) used to drive the piezoelectric transducer of the prestabilization resonator accepts 0-5 V at the programming input, the signal generated by the PCI-6221 device is conditioned with a voltage divider and by external addition of an analog offset in order to be able to take full advantage of the resolution of the digital-to-analog converters. Circuit diagrams can be found in the appendix, see section D.3.

Compensation of Piezo Nonlinearity Piezoelectric actuators do not display a linear dependence of the length change on the driving voltage. The hysteresis of the piezos can be accounted for by a calibration measurement of the position of the higher resonator modes. These are spaced by identical frequency intervals. The frequencies of the transverse modes relative to the (0,0) Gaussian mode are given in table 4.2.

Limitations

One of the major limitations of the scan lock setup is the fact that it operates at very low detection frequencies. Consider for example the Pound-Drever-Hall method for laser stabilization: Some of its beauty stems from the fact that the error signal is a component of the photodiode signal at the modulation frequency, in the MHz range. This implies that it is largely immune to much of the technical noise whose magnitude typically scales with the inverse of the frequency. The scan lock operates at 50 Hz, making it vulnerable to technical noise from photodiodes, high-voltage amplifiers that drive the piezos and so on. The time measurements of the microcontroller depend on the reproducibility of the high-voltage ramp for the piezoelectric transducers as well as on the comparator response that contribute to the technical noise.

The fact that the scan lock resonator is operated in air and not in vacuum induces

additional noise, which is probably the main contribution to the total jitter in the stabilization.

With respect to absolute frequency accuracy, the scheme relies on a strict correlation between the time from the beginning of the piezo sweep, piezo voltage, and piezo position. The amplitude of the piezo response is normalized by taking the time interval between two reference laser peaks, that is the time interval that corresponds to one free spectral range, as a reference. The nonlinearity of the piezo response can be accounted for, but such a procedure is only valid for one particular sweep amplitude and sweep frequency and should therefore be repeated regularly.

Alternative Schemes

As an alternative to the current implementation of the spectroscopy laser stabilization, namely the “scan lock” scheme, a scheme based on Pound-Drever-Hall locking the spectroscopy laser to a reference cavity in a tunable way could be used. The idea is to modulate sidebands on the carrier that can be tuned in frequency from 0 to some value above half the free spectral range of the resonator. The laser would then be locked to these tunable sidebands by additional sidebands that are modulated onto the tunable sidebands. This would require a broadband RF amplifier and a broadband EOM and a tunable RF source that could be modulated at a few MHz as required for the PDH lock. As suggested by Ye [Ye06a], a frequency mixing scheme would be advantageous: A synthesizer frequency could be added with a voltage controlled oscillator (VCO) frequency via a double balanced mixer. A bandpass filter can pick the sum or difference frequency. The synthesizer could be used for the frequency scan, while the modulation for the PDH lock could be done via the VCO.

Still another approach would be to shift the laser frequency with a double-pass acousto-optical modulator (AOM) and lock the shifted light to a reference cavity with the PDH method. Tunability would be achieved by varying the driving frequency of the AOM. This scheme requires a broadband AOM and the lock to the resonator would probably suffer from beam pointing issues when tuning the driving frequency of the AOM over a wide range. Therefore, the frequency mixing sideband scheme suggested above would probably be the more viable alternative.

CHAPTER 5

Optical Molecular Spectroscopy of Feshbach Molecules

5.1 Sample Preparation

A pure sample of trapped ultracold Cs Feshbach molecules is prepared by a series of laser cooling techniques applied to ^{133}Cs atoms and final association by means of a magnetic field ramp over a Feshbach resonance. Feshbach resonances are discussed in section 2.2.3 and the particular properties of weakly bound cesium dimers are examined in section 3.2.3.

Here a brief overview of the Cs BEC experiment or “LevT” experiment, as we like to call it for historical reasons, where the spectroscopic measurements are carried out is given. The name “LevT” or “levitated trap” stems from the fact that this setup relied on a combination of optical dipole traps and a magnetic field gradient that levitates the Cs atoms against gravity for the realization of the first Bose-Einstein condensate of cesium in 2002 [Web03b]. The focus of the experiment has since then shifted from ultracold atoms to ultracold molecules and few-body physics, as evidenced by the production of a pure molecular quantum gas in 2003 [Her03] and the recent experimental observation of Efimov quantum states [Kra06b].

The Cs BEC machine is described in detail in the doctoral theses by Tino Weber [Web03a], Jens Herbig [Her05], and Tobias Kraemer [Kra06a] and in the diploma thesis by Michael Mark [Mar03]. The production of ultracold Feshbach molecules in our experiment is detailed in references [Her03, Mar05, Kra04, Mar07]. Background on laser cooling techniques can be found in the classic book by Metcalf and van der Straten [Met99]. Optical dipole traps are discussed in the review article by Grimm, Weidemüller and Ovchinnikov [Gri00].

A beam of ^{133}Cs atoms is produced in an oven and then slowed by a Zeeman slower. A magneto-optical trap (MOT) is loaded for a time of typically 6 s. Subsequently, the sample is cooled and polarized in the lowest hyperfine state $|F = 3, m_F = 3\rangle$ by Raman-sideband cooling. We typically obtain $2 \cdot 10^7$ atoms after this step.

The sample is adiabatically released from the Raman lattice into a large volume dipole trap. This so-called reservoir trap presently consists of one CO_2 laser beam with a wavelength of $10.6 \mu\text{m}$ and one Yb high power fiber laser beam with a wavelength of 1070 nm. The beam waists are $600 \mu\text{m}$ for the CO_2 laser and $700 \mu\text{m}$ for the Yb fiber laser. Both lasers can deliver up to 100 W but are normally operated at lower power. With these parameters, the resulting trapping potential is too shallow to hold

5 Optical Molecular Spectroscopy of Feshbach Molecules

the atoms against gravity. Therefore we apply a magnetic gradient field $\nabla B \simeq 31$ G/cm that couples to the magnetic moment μ of the atoms and exerts a force $F_z = -\mu\nabla B_z$ on the atoms and levitates them. The resulting effective trap depth is around $7 \mu\text{K}$. After release from the Raman lattice into the reservoir trap, the sample is allowed to thermalize during a period of plain evaporation that lasts 2 seconds, as shown in panel A of figure 5.1. We obtain around $4 \cdot 10^6$ atoms at a temperature of $T \simeq 1\mu\text{K}$.

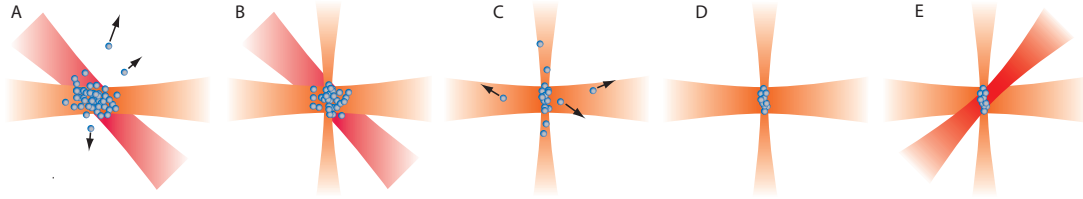


Figure 5.1: Evaporation scheme for ultracold molecule production: The figure shows the current evaporation scheme for ultracold molecule production. *A*: Plain evaporation in a crossed dipole “reservoir” trap, consisting of one CO₂ laser beam and one 1070 nm Ytterbium fiber laser beam. *B*: Collisional loading of the CO₂ dimple beam. *C*: Forced evaporative cooling in the dimple beam. *D*: Final trap configuration. The dimple beam is able to hold the atoms against gravity without the need for magnetic levitation. The CO₂ reservoir beam assures inclusion in the dimple’s longitudinal direction. Molecule formation by means of a Feshbach resonance is done in this final trap that is suited to trap molecules as well as atoms. The laser beams for the dipole traps lie in the horizontal plane, the magnetic bias field is applied in the vertical direction. *E*: The spectroscopy laser beam (diagonal) lies in the same plane as the trapping beams.

In the next stage, the trapping potential is modified by a “dimple” beam [Gri00] that consists of a more tightly focused CO₂ laser beam. The dimple creates a much stiffer optical trap, as illustrated in panel *B* of figure 5.1. The phase space density is increased during dimple loading because the density increases whereas the temperature stays constant. This is due to thermal contact with the reservoir and depends on elastic collisions. The 1064 nm beam is then switched off and the final trap consists of the crossed CO₂ dimple and CO₂ reservoir beams. In this crossed CO₂ trap we typically measure $1 \cdot 10^6$ atoms at a temperature of $T \simeq 1\mu\text{K}$.

In the next step forced evaporative cooling is implemented as shown in panel *C*. The power of the CO₂ dimple is first slightly lowered within 2 seconds yielding a trap depth of $\sim 8 \mu\text{K}$. Then the magnetic field gradient is turned off in an exponential way during 4.2 seconds leading to one-dimensional evaporative cooling of the atomic sample. The magnetic bias field and therefore the scattering properties of the atoms are set to appropriate values for each step of the experiment to optimize the evaporation efficiency. Finally, we obtain $\sim 5 \cdot 10^5$ atoms at a temperature of $T \simeq 250$ nK.

Note that this trap setup consisting of the CO₂ dimple and the CO₂ reservoir beam, see panel *D* in figure 5.1, is suited to trap molecules as well as atoms. Turning off the 1070 nm light has the distinct advantage that radiative molecule losses caused by

the broadband 1070 nm light can be avoided. The 1070 nm laser can drive molecular optical transitions whereas the CO₂ lasers cannot. In fact, we find that the high-power 1070 nm laser we are using is not suited to trap molecules because it inevitably drives molecular transitions due to its broad spectral profile of ~ 2 nm width. We observe rapid molecular loss when illuminating the sample with this laser, as discussed in more detail on page 107. As an alternative to the CO₂ traps we are currently using, trapping of molecules would be possible with a narrow-band single frequency laser in combination with a fiber amplifier. The absence of a magnetic field gradient for levitation enables a much more precise control of the magnetic field and therefore of the molecular properties. For molecule production, we use one of the Feshbach resonances indicated in figure 3.7, namely the 19.8 G, the 47.9 G or 53.4 G Feshbach resonances. After association by adiabatically ramping over the resonance position, we ramp the magnetic field to a value that corresponds to a molecular binding energy of roughly 5 MHz. Since the molecules would rapidly be lost due to atom-dimer collisions, it is imperative to clean the molecular sample from the atoms remaining after the association step. This is done with a “blast” beam resonant with an atomic transition, similar to reference [Xu03]. The blast light is the same as the imaging light described in the next section. The molecular binding energy of 5 MHz during this procedure assures that molecular losses due to the blast light can be kept small. However, the the blast procedure increases the temperature of the molecular sample to $T \simeq 400$ nK.

As detailed in a recent paper [Mar07], we use the 19.8 G resonance to populate the $4g(4)$ state, where the labeling is according to the quantum numbers $f\ell(m_f)$, as shown in figure 3.7. The 48 G resonance is due to an avoided crossing of a $4d$ state and a $6s$ state right below threshold with the upper branch of the crossing intersecting the threshold (see inset in figure 3.7). Therefore, when we use this Feshbach resonance for molecule formation, we initially populate the $6s$ state. The 53 G Feshbach resonance is associated with a $2g$ state.

By adiabatically following avoided crossings between different molecular states or nonadiabatically jumping the crossings, we have populated any given weakly bound molecular state up to l -wave states (binding energies up to 10 MHz below the $(F = 3, m_F = 3) \times (F = 3, m_F = 3)$ scattering threshold) in the region of low magnetic fields (up to 50 G) [Mar07].

When the Feshbach molecules reside in the final crossed CO₂ trap, they are exposed to the spectroscopy light, see panel *E* of figure 5.1. Both the spectroscopy laser beam and the dipole trap beams lie in the horizontal plane. The magnetic bias field is in the vertical direction. The spectroscopy light is switched on for a given amount of time while the molecules reside in the final trap. One cycle of the experiment takes on the order of 30 seconds. On the one hand, this cyclic experimental procedure bears the great advantage that also weak absorption lines can be detected by increasing the time the spectroscopy light interacts with the molecular sample, which is only limited by the collisional lifetime of the sample. On the other hand, the discontinuous character of the spectroscopy severely limits the frequency range that is practicable to scan. De-

tection of the molecules remaining in the original Feshbach state after interaction with the spectroscopy light is by dissociation of the molecules at the respective Feshbach resonance and standard absorption imaging, as detailed in section 5.2.2.

5.2 Integration of the Spectroscopy Setup into the LevT Experiment

5.2.1 Coupling the Spectroscopy Beam into the Experiment

The spectroscopy light reaches the optical table of the Cs-BEC experiment through a polarization-maintaining single-mode optical fiber (PM1550HP, Nufern). Figure 5.2 shows part of the LevT experiment with the optics for the spectroscopy beam in the foreground. The beam is collimated (C220TM-C, Thorlabs, $f=11$ mm, beam waist 1.04 mm), passes a mechanical shutter and a $\lambda/2$ waveplate and is then expanded by a telescope ($f=-30$ mm and $f=300$ mm), again yielding a collimated beam. A 2" gold mirror mounted on a piezo driven mirror holder allows for fine adjustment. The beam is then focused by a $f=400$ mm lens which creates a focus of waist $w_0 = 21.3 \pm 0.5 \mu\text{m}$ at a distance of 412.5 mm from the $f=400$ mm lens at a wavelength of 1550 nm. At 1510 nm, the focus is at 411 mm with a waist of $20.3 \pm 0.6 \mu\text{m}$, at 1580 nm the focus is at 413 mm with a waist of $22 \pm 0.4 \mu\text{m}$. The Rayleigh range is on the order of 1 mm.

The power after the optical fiber is 16 mW at 1550 nm when the spectroscopy laser is operated at full power. Transmission through the vacuum chamber viewport is $\sim 85\%$. Together with losses from two silver mirrors, one gold mirror and the lenses, a maximum power of ~ 12 mW can be delivered to the molecules. During experiments, the laser is not operated at full power in order to assure single mode operation and a small fraction of the light is used for the stabilization scheme, decreasing the power delivered to the molecules to 9 – 10 mW, depending on the power and wavelength settings of the laser.

Alignment with Near Resonant Light

The spectroscopy beam was first aligned geometrically relative to the position of the laser beams used for Raman sideband cooling.

In a second step, light of the 852 nm reference laser that runs -160 MHz red detuned from the $F = 4 \rightarrow F' = 5$ hyperfine transition of the Cs D_2 -line was used to further optimize beam pointing by monitoring the atom number in the dimple trap and optimizing for maximum loss from the trap induced by the near resonant light. Even though beam pointing is not perfectly identical for the reference light and the spectroscopy light due to dispersion effects, the spectroscopy beam is enclosed by the reference beam ($\sim 200 \mu\text{m}$ waist) at the position of the molecules. Therefore, this adjustment gives a

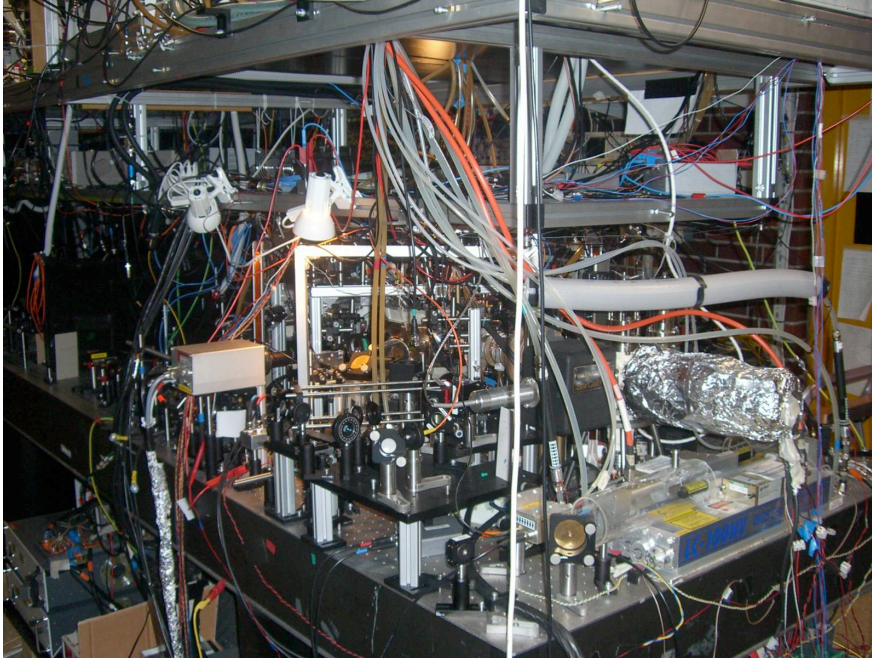


Figure 5.2: LevT experiment with spectroscopy beam: Part of the experimental setup of the LevT experiment is shown. The main vacuum chamber is in the center and can hardly be discerned. On the right hand side, elevated above the optical table, the Cs oven can be seen. Below are the two CO₂-lasers. The little elevated platform in the foreground supports the optics for the spectroscopy beam. Left of it there is the CCD camera used to image the atomic cloud.

very good starting point for the last step of adjustment, namely for the implementation of an optical dipole trap with the spectroscopy light.

Optical Dipole Trap with Spectroscopy Light

In order to see a direct effect of the spectroscopy laser beam on the atomic and molecular Cs clouds, an optical dipole trap was implemented using the spectroscopy light.

In an optical dipole trap for neutral atoms or molecules, the laser light induces a dipole moment in the particle that in turn interacts with the laser light. For a detailed discussion, see the review article by Grimm *et al.* [Gri00]. For large detuning from the atomic resonance frequency ω_0 , the interaction potential $U_{dip}(\vec{r})$ between the induced dipole moment of an atom modeled as a two-level system and the light field can be written as

$$U_{dip}(\vec{r}) = -\frac{3\pi c^2}{2\omega_0^3} \left(\frac{\Gamma}{\omega_0 - \omega} + \frac{\Gamma}{\omega_0 + \omega} \right) I(\vec{r}), \quad (5.1)$$

where Γ is the natural linewidth of the atomic transition and $I(\vec{r})$ is the intensity distribution of the laser light.

A discussion related to the 1064 nm traps and CO₂ traps that we use for cesium in our

5 Optical Molecular Spectroscopy of Feshbach Molecules



Figure 5.3: Optical dipole trap with spectroscopy laser: The image on the left shows a time-of-flight picture of an atomic cloud after release from the CO₂ dimple beam with the spectroscopy laser switched off. The CO₂ reservoir beam is greatly reduced in intensity to provide only very weak inclusion along the axis of the dimple beam. The picture on the right is taken with the spectroscopy laser turned on while the sample resides in the dimple beam. It shows an additional feature on the right hand side of the cloud induced by the spectroscopy light, as indicated by the dashed circle. The two images correspond to the same region of interest. They are viewed at the same magnification. The arrows indicate the position of the focus of the CO₂ dimple beam. During experiments the additional CO₂ reservoir beam that provides inclusion along the axis of the dimple beam shifts the cloud to the position of the dashed circle. The total number of atoms in the dimple is increased when the spectroscopy light is switched on as evidenced by the more prominent central feature in the right panel (arrows). This is due to better longitudinal inclusion of the atomic cloud.

experiment can be found in reference [Mar03]. Taking into account both the D_1 - and the D_2 -line of cesium, the dipole potential can be calculated from

$$U_{dip}(\vec{r}) = -\pi c^2 \left[\frac{\Gamma_1}{2\omega_1^3} \left(\frac{1}{\omega_1 - \omega} + \frac{1}{\omega_1 + \omega} \right) + \frac{\Gamma_2}{\omega_2^3} \left(\frac{1}{\omega_2 - \omega} + \frac{1}{\omega_2 + \omega} \right) \right] \cdot I(\vec{r}), \quad (5.2)$$

where the indices 1 and 2 pertain to the Cs D_1 - and D_2 -lines, respectively. Note that the D_1 -line and D_2 -line have been weighted by a factor of 1/3 and 2/3, respectively, when comparing with the two-level model, in order to account for the different line strengths. The line widths are $\Gamma_1 = 2\pi \cdot 4.56$ MHz and $\Gamma_2 = 2\pi \cdot 5.22$ MHz, the atomic transition frequencies are $\omega_1 = 2\pi \cdot 335.116 \cdot 10^{12}$ Hz and $\omega_2 = 2\pi \cdot 351.7257 \cdot 10^{12}$ Hz.

It is convenient to express the potential depth as a temperature by rescaling with the inverse of the Boltzmann constant k_B . With these parameters and a laser power of 10 mW, a beam waist of 22 μm at the focus and a wavelength of 1510 nm, one obtains a trap depth of 1.7 μK , which should be observable experimentally for a sample that has a temperature of 200 – 250 nK.

We prepared a sample in the final trap of the LevT experiment that consists of the CO₂-dimple beam and the large CO₂-reservoir beam that provides inclusion along the axis of the dimple beam. We then lowered the intensity of the reservoir beam in order to make the trap very shallow along the axis of the dimple beam. The spectroscopy laser light was used to provide inclusion of the atomic or molecular cloud along the axis of the dimple beam. This could be observed as a slight shift of the samples position

in comparison to the dimple beam alone. The position of the cloud with the spectroscopy light trap corresponds to the position of the trap used in the spectroscopic experiments consisting of the CO₂ dimple and the CO₂ reservoir beam. In addition, an increase in particle number can be observed. Figure 5.3 shows this change in the shape of the cloud with and without the spectroscopy light, which we take as evidence for hitting the sample with the spectroscopy light. This procedure was done both for the atomic sample and for the molecular sample after Feshbach association, yielding largely identical patterns.

5.2.2 Detection of the Spectroscopy Signal

For detection, the molecular sample is dissociated by ramping the magnetic field 1 to 2 G above the respective Feshbach resonance. Then the resulting atomic cloud is imaged by standard absorption imaging. The imaging light is resonant with the $F = 4, m_F = 4 \rightarrow F' = 5, m_{F'} = 5$ atomic transition and preceded by a repumping beam. The frequency of the imaging light is adjusted to the magnetic field at which imaging takes place to account for the differential Zeeman shift of the transition. Temperature measurements are done by fitting the size of the atomic cloud in a time-of-flight series.

When the spectroscopy laser coincides with a molecular transition, molecules in the first electronically excited state are produced. If these decay to the continuum of two free atoms and yield two hot atoms, they are immediately lost from the trap because the dipole trap is too shallow to trap them. On the other hand, the excited molecules can decay to ground state molecules that are more deeply bound than the original Feshbach molecules due to good Franck-Condon overlap with lower lying states. When the Feshbach molecules are dissociated by a magnetic field ramp across the respective Feshbach resonance and imaged by absorption imaging, these more deeply bound molecules are not going to be dissociated to free atoms and remain invisible to our imaging laser. Therefore, both mechanisms, trap loss and production of more deeply bound molecules, lead to a decrease in the absorption imaging signal. With each experimental run, the molecules are prepared in the same way and the spectroscopy light is switched on for a given constant time. A stable baseline molecule count of approximately 20.000 molecules was obtained.

5.3 Spectroscopic Measurements

Ultracold molecules were prepared according to the procedure described above. As detailed in section 4.2.3, a stabilization scheme was developed that allows for control of the spectroscopy laser frequency with sub-MHz precision. Since it is not practical to search for a molecular transition at such high resolution, we resorted to a coarse searching procedure as discussed in section 4.1.4. We “locked” the spectroscopy laser to the output of a wavemeter. During each individual experimental cycle, the laser wavelength was swept over a certain range. The sweep was triggered when the spec-

5 Optical Molecular Spectroscopy of Feshbach Molecules

troscopy light was switched on. The sweep duration was equal to the duration of the spectroscopy pulse. Typical values for the step size in laser frequency from one run of the experiment to the next were 500 MHz with a sweep amplitude of 700 MHz to allow for some overlap between the individual data points. We chose a duration of 500 msec for the spectroscopy pulse. This is a tradeoff between the longest possible observation times in order to increase the contrast for very weak molecular lines on the one side and limited molecular lifetime due to inelastic collisions on the other side. We would be able to increase molecular lifetime by decreasing trap frequencies and consequently molecular density.

For the spectroscopic experiments performed thus far we have chosen $4g(4)$ molecules produced at the 19.8 G Feshbach resonance, see figure 3.7. At the moment, detailed calculations of the singlet and triplet component of different Feshbach molecular states at different magnetic fields are under way in Innsbruck, where Peter van der Straten has been using the NIST code provided by Paul Julienne. Olivier Dulieu, Nadia Bouloufa and Anne Crubellier are currently setting up ground state hyperfine calculations to obtain accurate ground state wave functions that can be used to calculate Franck-Condon Factors with the excited state.

5.3.1 Expected Transition Rates

It is important to have an orientation about what photon scatter rates can be expected for a given transition. A basic introduction to optical transitions is given in section 3.3. As discussed in chapter 2.4 of reference [Met99], the photon scatter rate γ_p of a two-level system can be calculated from

$$\gamma_p = \frac{s_0\gamma/2}{1 + s_0 + (2\delta/\gamma)^2}, \quad (5.3)$$

where s_0 is the on-resonance saturation parameter

$$s_0 = \frac{2|\Omega|^2}{\gamma^2} = \frac{I}{I_s}. \quad (5.4)$$

Here, γ is the decay rate of the excited state population, δ is the laser detuning from the resonance frequency and Ω is the Rabi frequency. I_s is the saturation intensity for the transition and depends on the dipole matrix element between the upper and the lower state. For Cs atoms, the saturation intensity $I_s^{at} = 1.09$ mW/cm² and the excited state decay rate is $\gamma^{at} = 2\pi \cdot 5.2$ MHz. Optical transition rates of molecules depend on the electronic matrix element as well as on the FC factor. One can assume in first approximation that the electronic part of the dipole matrix element and the linewidth of the molecular excited state are similar to the values known for atoms. If we take the width of the excited molecular level γ^{mol} to be twice the width of the atomic excited state γ^{at} , use the atomic saturation intensity I_s^{at} and take the Franck-Condon factors

(FC) for the vibrational wave function overlap into account, we reach the following relation for the Rabi frequency of an optical transition

$$|\Omega^{mol}| \approx \gamma^{at} \sqrt{\frac{I}{I_s^{at}} \cdot FC} \quad (5.5)$$

The photon scatter rate from the initial state for Rabi frequencies much smaller than the excited state linewidth is

$$\gamma_p^{mol} \approx \frac{|\Omega^{mol}|^2}{\gamma^{mol}} \approx \frac{1}{2} \gamma^{at} \cdot \frac{I}{I_s^{at}} \cdot FC. \quad (5.6)$$

Nadia Bouloufa and Olivier Dulieu from Orsay have calculated Franck-Condon factors for transitions between weakly bound ground state levels and vibrational levels in the coupled $0_u^+(P_{1/2})$ and $0_u^+(P_{3/2})$ excited state potentials. They have been using pure $X^1\Sigma_g^+$ singlet ground state potentials without taking the hyperfine interaction, i.e. the coupling between the singlet and triplet ground states into account. More accurate calculations for the ground state using wave functions that take the ground state hyperfine interaction into account are under way, see also section 6.1.1. For the electronically excited state, wave functions were calculated from ab initio relativistic potentials that take spin-orbit coupling into account, see figure 3.3. As stated above, potentials with 0_u^+ symmetry were chosen. Since these potentials are not adjusted to the spectroscopic knowledge gained by Vergès and Amiot [Ver87] they can reliably predict “typical” wave functions but cannot give accurate estimates for transition wavelengths. In the wavelength region from 1510 nm - 1520 nm they obtain FC factors on the order of 10^{-12} taking the last bound vibrational level ($v = 155$) of the singlet ground state.

Assuming that $P = 10$ mW of spectroscopy laser power are delivered to the atoms with a beam waist w_0 of $22 \mu\text{m}$, we obtain a peak intensity of $I_0 = \frac{2P}{w_0^2\pi} = 1.3 \text{ kW/cm}^2$. Taking typical values for the atomic excited state decay rate $\gamma^{at} = 2\pi \cdot 5.2 \text{ MHz}$ and for the atomic saturation intensity $I_s^{at} = 1 \text{ mW/cm}^2$, one obtains a photon scatter rate of $\gamma_p = 20/\text{second}$ which corresponds to a molecule lifetime of $1/\gamma_p = 50 \text{ ms}$ and a Rabi frequency of $\Omega^{mol} \approx 2\pi \cdot 6 \text{ kHz}$.

In addition, it has to be taken into account that the g/u symmetry allows for transitions to the 0_u^+ excited state potentials only from ground states with g symmetry. Feshbach molecules have mixed g/u character due to hyperfine mixing of the $X^1\Sigma_g^+$ state and the $a^3\Sigma_u^+$ state. If we equate the magnitude of the g component in the Feshbach molecule’s wave function with the magnitude of the $X^1\Sigma_g^+$ contribution, we can adjust the expected transition rates. The magnitude of the singlet component varies depending on the state and magnetic field. Using the NIST code for the structure of Cs Feshbach molecules provided by courtesy of Paul Julienne, Peter van der Straten estimated the singlet component of different Feshbach states by calculating the expectation value for the spin operator. A value of 1 corresponds to a pure triplet state and

5 Optical Molecular Spectroscopy of Feshbach Molecules

a value of 0 corresponds to a pure singlet state. Typical values were on the order of 20% singlet component in terms of probability, which reduces the photon scatter rate to 4/s. This does not take into account the R -dependence of the singlet/triplet mixing in the ground state. It is mainly the singlet component at the inner turning point of the ground state potential that is important for the transition, because there the turning points of the excited and the ground state potentials nearly coincide, as required by the Franck-Condon principle, see section 3.3.1. Due to the much weaker slope of the potential at long range, the probability distribution has a much greater magnitude at large internuclear separation. As the interatomic “spring” is very soft at large separations, the atoms spend most of their time at large internuclear distance. The outer turning points of the ground and excited state potentials are situated at widely different interatomic separation R due to the long-range nature of the Feshbach molecules and the tight binding of the excited state levels addressed with a $1.55 \mu\text{m}$ laser.

Franck-Condon factors increase by one order of magnitude when going to states that are bound by a value comparable to the atomic hyperfine splitting [Bou06], e.g. the singlet vibrational level $\nu = 151$, bringing up the photon scatter rate to 40/s. The $6s$ state that arises from coupling between the $33(6, -1)$ and the $44(6, -7)$ states described in section 3.2.3 for example can be viewed to be bound by twice the atomic hyperfine splitting with respect to the $(4, 4) \times (4, 4)$ atomic scattering threshold at magnetic fields below 15 G. There it mainly consists of the $44(6, -7)$ state, justifying the assumption of such increased FC factors. The singlet component at the inner turning point of the potential is a factor of 3 larger for this state at a magnetic field of 15 G as compared to 20 G [Str07], where it has predominantly $33(6, -1)$ character. Similar calculations have been performed for the s , d and g wave Feshbach states (see figure 3.7) that lie within the range of accessible magnetic fields for our experiment. Individual states differ by a factor of 10 with respect to the magnitude of the singlet probability distribution near the inner turning point of the potential. This indicates that the choice of initial state and magnetic field can influence the transition probabilities considerably, see figures 5.4 and 5.5.

In the coarse search for molecular resonances, we scanned the laser over a range of 700 MHz during each experimental run. The scanning technique leads to a reduction of the effective spectral intensity. If we again assume the linewidth of molecular transitions to be twice the atomic transition linewidth, such a scanning reduces the effective intensity by a factor of almost $\sim 10^{-2}$, leaving us with a photon scatter rate on the order of 1/s. We use trapped molecules and therefore the interaction time between the light field and a given molecule is only limited by the lifetime of the molecules, allowing very long interaction times of 500 msec. This is in contrast to the short interaction times for molecular beam experiments. Thus, even though the photon scatter rates are extremely low, one could hope to see an effect of the spectroscopy light due to the long interaction times. These calculations only give a rough estimate of transition rates and constitute a crude approximation but they clearly show the difficulty driving these transitions.

5.3 Spectroscopic Measurements

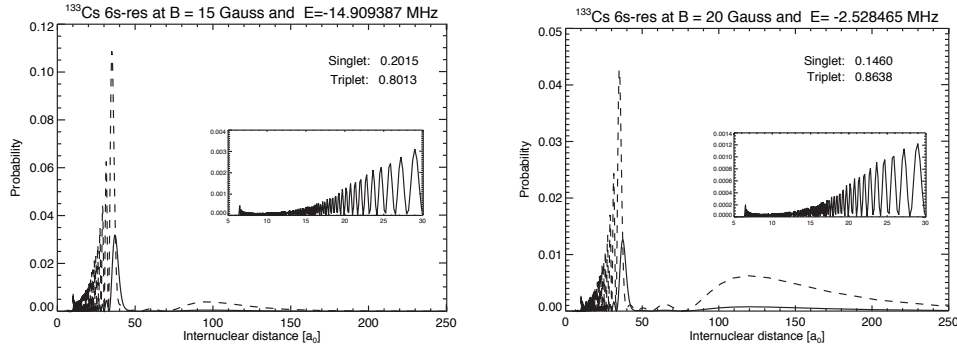


Figure 5.4: Ground state 6s wave functions: The absolute square of the singlet and triplet component of the Feshbach molecules' wave function is shown. The figure illustrates how the choice of magnetic bias field can influence the magnitude of the singlet and triplet components near the inner turning points of the potentials which is the region that is most relevant for optical transitions in the $1.55 \mu\text{m}$ wavelength region. The inset shows an enlarged view of the singlet component in the region of small nuclear separation. For transitions to the excited 0_u^+ states, only the singlet component is relevant. It can be clearly seen that the singlet component near the inner turning point is much larger at a magnetic field of 15 G than at 20 G. Details are given in the text. Binding energy is with respect to the (3,3)x(3,3) scattering threshold. Figure courtesy of Peter van der Straten.

We illuminated a molecular sample trapped in the crossed CO_2 -trap with a 1070 nm Ytterbium fiber lasers and a single-frequency Nd:YAG-laser to find out whether we could use these lasers to trap molecules. With the narrow linewidth, single-frequency Mephisto laser, we did not observe a reduced lifetime of the molecular sample. In contrast, when we used the very broadband Yb fiber laser at an intensity of $10\text{W}/\text{cm}^2$, we observed rapid molecular loss decreasing the lifetime of the molecular sample from 5 seconds to 200 msec, indicating that we were driving optical transitions with the broadband 1070 nm laser light.

This observation led us to change the trap setup from our previous crossed dipole trap [Her03, Mar03] that involved a combination of CO_2 -laser light and broadband 1070 nm light to the current setup described in section 5.1. In our current trap setup, the final trap consists of two crossed CO_2 -laser beams that do not drive any molecular transitions and are therefore well suited to trap molecules as well as atoms.

It is instructive to compare the parameters for the current spectroscopy laser setup with the observations involving the broadband 1070 nm light. The spectral width $\gamma_{1070\text{nm}}$ of the 1070 nm laser is approximately 2 nm, corresponding to 520 GHz. Therefore, assuming a smooth spectrum of the laser, the intensity available for driving a transition with a width γ of a few MHz is the total laser intensity I_{tot} scaled by a factor of $\frac{\gamma}{\gamma_{1070\text{nm}}}$ which is on the order of 10^{-5} . The Franck-Condon factors between highly excited singlet ground state wave functions and vibrational levels of the 0_u^+ potentials

5 Optical Molecular Spectroscopy of Feshbach Molecules

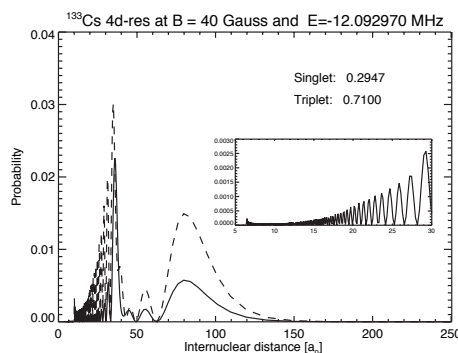


Figure 5.5: Ground state 4d wave functions: Similar to figure 5.4, squared singlet and triplet wave functions are shown for the 4d Feshbach state that causes the Feshbach resonance at 48 G. This illustrates that the particular choice of Feshbach state also influences the magnitude of the singlet contribution near the inner turning point. Figure courtesy of Peter van der Straten.

in the range accessible to the 1070 nm laser are on the order of 10^{-5} to 10^{-4} , again considering a pure singlet vibrational level ($v=151$) in the ground state bound by the same value as above [Bou06]. With these parameters, taking a FC factor of 10^{-5} , equation 5.6 yields a photon scatter rate $\gamma_{p,1070nm}=30/s$ for the 1070 nm laser. Rescaling this again for the singlet component of the ground state wave function, we obtain a value on the order of 6/s just as before with the 1.55 μm spectroscopy laser. We observed a molecular lifetime of 200 msec. Assuming that every molecule that absorbs a photon is lost from the trap, this is consistent with the calculated photon scatter rate given the large uncertainty of such a simplistic estimation.

These results should be interpreted with care, however. First, we do not know the spectral profile of our 1070 nm laser. It is conceivable that on the scale of the width of the molecular resonances, the spectral intensity shows great variations and the simple ratio between the spectral width of the molecular resonance and the spectral width of the laser underestimates the spectral intensity driving the molecular transition at 1070 nm. We plan to use an optical spectrum analyzer to investigate the spectral properties of the 1070 nm laser. Second, this comparison assumes that only transitions involving the 0_u^+ potentials are involved. Looking at figure 3.3, one can see that the 1070 nm laser reaches the excited state manifold in a region where further potentials become available in addition to the potentials reached by the 1.55 μm laser. They can be accessed from the lowest lying triplet state $a^3\Sigma_u^+$ that contributes the main component to the wave function of our Feshbach molecules. These are the $1g(P_{1/2})$, the $0_g^+(P_{1/2})$ and the $0_g^-(P_{1/2})$ potentials. The $1_u(P_{1/2})$ potential can be reached from the singlet ground electronic state. We do not know the Franck-Condon factors for these potentials and therefore the above estimate could be misleading. If the FC factors for these potentials were much larger than for the 0_u^+ potentials we would be erroneously led to believe that we would be able to drive transitions with the 1.55 μm laser. In addition, the

1070 nm laser is spectrally broad enough to drive several molecular transitions at the same time. Their rates would then add up, again leading us to believe that we would be able to drive the transitions. The spacing between individual 0_u^+ vibrational levels is $\sim 1 - 2$ nm in the region addressed by the 1070 nm laser, while the laser's spectral width is 2 nm. The laser could also drive transitions to potentials of different symmetry simultaneously.

With the caution warranted by these considerations, the extremely small Franck-Condon factors for transitions driven by the 1550 nm laser appear to be compensated for by its higher spectral intensity if one only contemplates transitions involving the 0_u^+ potentials. From this comparison it should be possible to drive molecular transitions with the 1.55 μm spectroscopy laser similarly to the 1070 nm laser.

5.3.2 Preliminary Results

We identified a series of wavelengths that were associated with a decrease of the molecule count by more than 2 standard deviations from the mean of the previous 25 experimental cycles in the region from 1510 nm to 1522 nm. The laser was “locked” to the wavelength meter during this coarse searching procedure. According to theoretical calculations of the bound levels in the two Cs_2 0_u^+ potentials, this range covers more than the expected spacing between two consecutive vibrational levels [Bou06] in this region which is up to 7 nm. These “candidate frequencies” represent the starting point for fine scanning by means of the stabilization scheme discussed in section 4.2.3. Most of these lines will turn out to reflect instability of the molecule count due to technical variations of the Cs-BEC experiment not associated with molecular loss due to the spectroscopy laser. Some of these “candidate lines” have been checked with the scan lock stabilization scheme demonstrating that the locking scheme can be operative over several hours in an automated way. A thorough remeasurement of the individual candidate lines with the scan lock stabilization scheme is needed in order to make a statement about whether we can drive molecular transitions with the current setup.

CHAPTER 6

Outlook

Future efforts concerning the optical spectroscopy project fall into two broad categories. Those dedicated to the optical spectroscopy of the Cs_2 Feshbach molecules *per se*, as outlined in section 6.1, and those dedicated to the production of ultracold molecules in their rovibrational ground state, discussed in section 6.2.

6.1 Optical Spectroscopy

The most immediate task is clearly the thorough evaluation of the “candidate frequencies” identified with the coarse searching procedure, as discussed in section 5.3.2. This evaluation will comprise remeasurement of the respective wavelength regions by means of the stabilization scheme described in section 4.2. This will clarify whether we can drive optical transitions of the Feshbach molecules in the $1.55 \mu\text{m}$ region with the current setup. We hope to get further guidance on expected transition wavelengths from theoretical calculations since the potential curves used for the computation of vibrational state energies are currently being adjusted to experimental data from classical spectroscopic experiments [Dul06]. In parallel, on the theoretical side, it is imperative to model the expected transition rates more accurately. On the experimental side, the current setup can be improved in two ways. First, an increase of the spectroscopy laser power can warrant higher transition rates. Second, the addition of a reference spectroscopy setup will increase the absolute wavelength accuracy of the setup.

6.1.1 Transition Rates

Theory

The FC factors for optical transitions to the 0_u^+ electronically excited potentials available so far are calculated with the wave functions of the last few bound vibrational levels of the pure $X^1\Sigma_g^+$ singlet ground state potential. The potentials reached with the $1.55 \mu\text{m}$ spectroscopy laser all have u symmetry and can therefore only be reached from the singlet ground state. These calculations have been carried out by Nadia Bouloufa and Olivier Dulieu from Orsay. The wave functions of the Feshbach molecules have mixed singlet/triplet character. Hyperfine coupling between the two potentials could modify the wave functions of the Feshbach molecules considerably. According to the Franck-

6 Outlook

Condon principle (see section 3.3.1), optical transitions are expected to take place near the inner turning points of the potentials, because these are well aligned. The wave function of the Feshbach molecules is peaked at very large nuclear distance but the magnitude of the singlet component of the wave function near the inner turning point is crucial for the transition probability. We have got two handles on the ground state wave function: the choice of initial Feshbach state (see section 3.2.3) and the magnetic bias field, i.e the binding energy (see figure 3.7). We have been using the NIST code for the structure of Cs Feshbach molecules in order to estimate the singlet and triplet components of the wave functions for different states and different magnetic fields. Figures 5.4 and 5.5 show a comparison of the wave functions of different Feshbach states and illustrate the effect of different magnetic fields. We will use such calculated ground state wave functions to optimize the overlap with the excited state wave functions (the FC factors) and the ground state singlet component by appropriately choosing the Feshbach state and magnetic field. This will also yield a better estimate of the transition rates.

The Orsay group, namely Olivier Dulieu, Nadia Bouloufa and Anne Crubellier, have been setting up ground state calculations including hyperfine structure in order to get a comprehensive model for the Feshbach molecules and in order to be able to calculate correct rates for the whole excitation process. Their results will guide the future experimental strategy. Thus far, they have calculated ground state wave functions at zero magnetic fields for levels that are somewhat more tightly bound than our Feshbach molecules. Figure 6.1 shows examples of a wave function that has predominantly singlet character and of a wave function with greater triplet component.

Experiment

There are two options in order to increase the transition rates in the spectroscopy experiment. The first option is to increase the power of the spectroscopy laser by means of a fiber amplifier, the second option is to choose a smaller detuning from the excited state asymptote. The photon scatter rate scales linearly with laser power as can be seen from equation 5.6. With the present parameters, the saturation parameter s_0 is on the order of 10^{-6} , see section 5.3.1. It is realistic to increase the laser power from the current 10 mW to 1-10 W, resulting in a saturation parameter of $\sim 10^{-4} - 10^{-3}$. Therefore, photon scatter rates could be increased considerably, but the saturation parameter will inevitably stay much smaller than one. Simply scaling up the photon scatter rate obtained in section 5.3.1 by a factor of e.g. 100 assuming that 1 W of laser power is delivered to the molecules would yield a rate of $10^4/s$ on resonance and $\sim 100/s$ for the case of the scanning procedure. There is a tradeoff however, because the Erbium-doped-fiber amplifiers used in this wavelength region start to operate only at wavelengths of 1520 nm and above and have their peak gain in the 1530 nm - 1570 nm region. FC factors are higher for the shortest wavelengths we can achieve with our laser, around 1510 nm. As mentioned in section 5.3.1, Feshbach molecules that

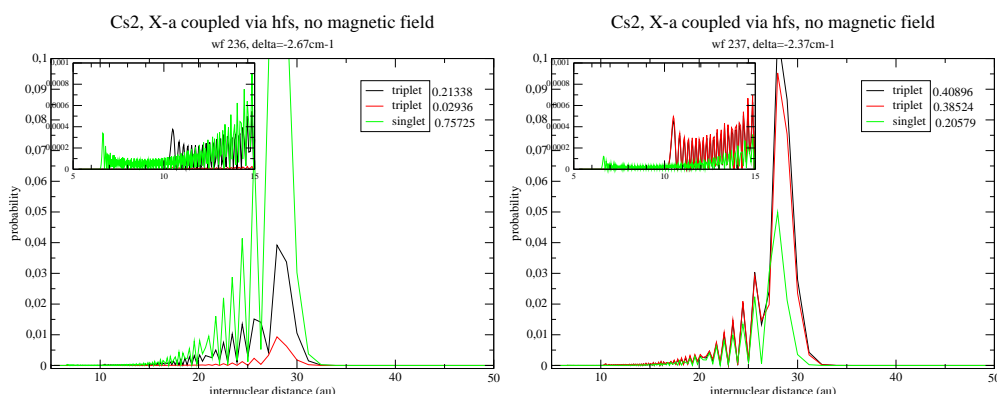


Figure 6.1: Ground state wave functions: Two different ground state wave functions calculated by the Orsay group are shown. They will be used to calculate FC factors with excited state 0_u^+ vibrational levels. The insets show an enlarged view of the region near the inner turning points of the potentials. The inner turning point of the $X^1\Sigma_g^+$ potential is located at smaller internuclear separation R than the turning point of the triplet $a^3\Sigma_u^+$ potential. This causes the double structure of the wave function at small R . It can be seen that the singlet component reaches in to internuclear distances of $\sim 6.5a_0$. It is larger in the left panel. Binding energies are 2.67 cm^{-1} and 2.73 cm^{-1} for the left and right panel, respectively. The present calculations do not include the magnetic field. Figure courtesy of Olivier Dulieu.

have predominantly contributions from the $(F = 4, m_F = 4) \times (F = 4, m_F = 4)$ channel can be viewed in first approximation to be bound by roughly twice the ground state atomic hyperfine splitting. The binding energy of the $X^1\Sigma_g^+$ ($v = 150$) level is 17 GHz and would correspond to such a state. FC factors for the $v=155$ ($v=150$) ground state singlet level and a 0_u^+ level at 1511 nm are $1.5 \cdot 10^{-12}$ ($6.6 \cdot 10^{-11}$), whereas at 1525 nm they are $2 \cdot 10^{-13}$ ($1 \cdot 10^{-11}$) and at 1532 nm, they are $8 \cdot 10^{-14}$ ($3.8 \cdot 10^{-12}$) [Bou06], which corresponds to a decrease by a factor of 8 and 20 in scattering rate, respectively. This diminishes the benefit from using an amplifier. Assuming a spectroscopy laser power of 5 W at the location of the molecules, the increase of scattering rate afforded by an amplifier would be a factor of 25-50. FC factors decrease rapidly with increasing wavelength so the lower cutoff in the amplifier gain is crucial and for commercial amplifiers often lies above the 1520 nm - 1530 nm assumed here, completely canceling the benefit from using an amplifier.

Franck-Condon factors increase dramatically when going to shorter wavelengths, i.e. smaller detunings from the excited state potential asymptotes. Again with calculations based on pure singlet wave functions for the ground state and 0_u^+ potentials in the excited state, FC factors increase to $5 \cdot 10^{-9}$ for the $v=155$ ground state level and $2 \cdot 10^{-7}$ for $v=150$ in the spectroscopy wavelength region around $1.4 \mu\text{m}$. Representative values for FC factors are given in table 6.1. Figure 6.2 gives an overview of the FC factors between the last bound vibrational level in the $X^1\Sigma_g^+$ state ($v = 155$) and 0_u^+

6 Outlook

excited state levels as a function of the spectroscopy laser wavelength. Also given is the FC overlap between the respective excited state level and the rovibrational ground state level of the $X^1\Sigma_g^+$ state which is relevant for transfer to the absolute ground state as discussed below.

Wavelength	$\nu = 155$	$\nu = 150$	$\nu = 0$
1.5 μm	$8 \cdot 10^{-12}$	$4 \cdot 10^{-10}$	$1 \cdot 10^{-3}$
1.4 μm	$4.6 \cdot 10^{-9}$	$2 \cdot 10^{-7}$	$1 \cdot 10^{-4}$
1.3 μm	$4 \cdot 10^{-9}$	$1.6 \cdot 10^{-7}$	$9 \cdot 10^{-9}$
1.2 μm	$2 \cdot 10^{-6}$	$8.6 \cdot 10^{-5}$	$2 \cdot 10^{-15}$

Table 6.1: **Franck Condon factors for 0_u^+ levels:** Representative values for FC factors based on unperturbed $X^1\Sigma_g^+$ states and ab initio calculations for the 0_u^+ vibrational wave functions. Excited levels are indicated by the approximate wavelength required for a transition from the $6s+6s$ asymptote, which corresponds approximately to the energy of the Feshbach molecules. FC factors for $X^1\Sigma_g^+$ levels with vibrational quantum numbers $\nu = 155$, $\nu = 150$ and $\nu = 0$ are given. The FC factors given are for particular excited state levels that lie within a few nanometers of the indicated wavelength. FC factors for the $\nu = 0$ state are relevant for the transition to the vibrational ground state as discussed below. Calculations done by our collaborators in Orsay [Bou06].

Between 1.4 μm and 1.3 μm they show a plateau and then increase rapidly at still shorter wavelengths. The useful range of wavelengths for the spectroscopy is given by the overlap of the intermediate state with the vibrational ground state of the $X^1\Sigma_g^+$ state given in the last column of table 6.1. It is largest for deeply bound excited state levels, i.e. long pump wavelengths. Already at 1.3 μm , this overlap becomes small. Going to wavelengths around 1.4 μm where FC factors for both the pump and the Stokes transition are acceptable is hampered by the rather poor availability of lasers for the wavelength region between 1.1 μm and 1.5 μm .

6.1.2 Reference Spectroscopy

Currently, the absolute wavelength accuracy of the 1.55 μm spectroscopy rests on the accuracy of the wavemeter, see section 4.1.3. The reproducibility of spectroscopy frequencies is set by the stabilization scheme (section 4.2). The wavemeter measurements agree with the measurements of a commercial wavemeter within the commercial wavemeter's stated absolute frequency accuracy of 500 MHz.

The most convenient way to calibrate the setup more accurately would be by means of a reference spectroscopy. Alternatively, one could frequency-double the spectroscopy light and perform iodine spectroscopy with the frequency doubled light. The most established reference method in the 1.55 μm region involves acetylene ($\text{H-C}\equiv\text{C-H}$, C_2H_2) spectroscopy. In the wavelength region from 1510-1540 nm, $^{12}\text{C}_2\text{H}_2$ has more than 50 strong absorption lines. Hydrogen cyanide (HCN) covers the region

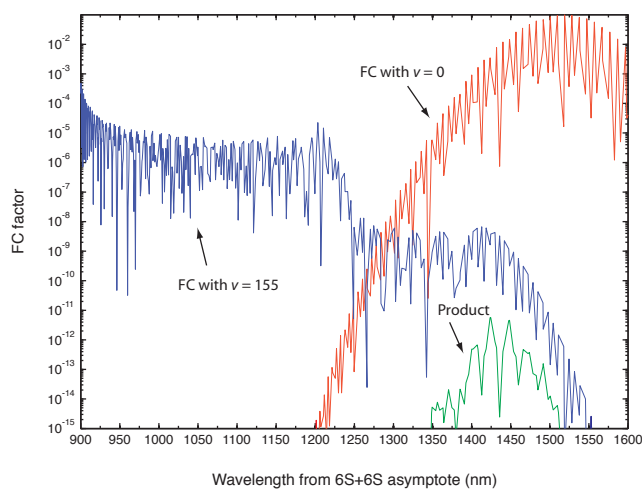


Figure 6.2: Franck Condon factors as a function of pump laser wavelength: The squared overlap between the $X^1\Sigma_g^+$ $v = 155$ vibrational wave function and 0_u^+ excited state vibrational wave functions as a function of spectroscopy or pump laser wavelength is labeled *FC with $v = 155$* . The squared overlap between a level reached by the spectroscopy laser and the rovibrational ground state of the X state is labeled *FC with $v = 0$* . Also indicated is the product of these two FC factors. Data provided by Nadia Bouloufa and Olivier Dulieu [Bou06].

from 1530-1565 nm. The isotopic variant $^{13}\text{C}_2\text{H}_2$ covers the range 1520 nm - 1550 nm. The tuning range of our laser is 1510 nm-1580 nm. The region from 1510 nm -1540 nm is most important for us because there the Franck-Condon factors for transitions from Feshbach states to the first electronically excited states in Cs_2 are higher than in the longer wavelength region. Therefore, $^{12}\text{C}_2\text{H}_2$ would be a good choice. The simplest setup involves absorption spectroscopy with a 50 Torr (1 Torr $\hat{=}$ 133.3 Pa) standard acetylene reference cell. These cells are widely available because they are used for calibration purposes in the telecommunications industry. The main limitations for the accuracy of such simple absorption spectroscopy are the pressure-dependent collisional line shifts and pressure broadening as well as the Doppler broadening of the resonances, yielding a width of 450 MHz. Pressure-induced shifts have been measured [Swa00] and stated reference wavelengths have been adjusted, yielding an absolute wavelength accuracy specified to 0.1 pm - 1pm [Gil01]. One pm is equivalent to a frequency of 130 MHz at a wavelength of 1520 nm. The accuracy limit for a simple transmission apparatus is 0.01 pm.

If higher accuracy is required, a more sophisticated setup has to be implemented. Much narrower spectroscopy features can be obtained with Doppler-free spectroscopy. Pressure shifts can be avoided by using very low acetylene pressure, e.g. 4 Pa (0.03 Torr). Saturation features can be produced with a width of 2 MHz and selected transition frequencies have been measured to an uncertainty of 2 kHz [Edw04, Mad06]. Most groups interested in high accuracy frequency standards in this region have used

a build-up cavity [Lab94] to reach the rather high saturation intensities. The absorption cell is placed within an optical resonator that increases the absorption path by an amount determined by the finesse of the resonator. Losses are kept low by means of Brewster-angled windows on the absorption cell. Here, low pressures are imperative not only in order to avoid pressure shifts but also because absorption would be too strong with a standard 50 Torr cell. Others have used an erbium doped fiber amplifier [Ona97]. Balling and colleagues [Bal05] used a very simple setup for saturation spectroscopy without a build-up cavity. They used a 50 cm long cell with 2 Pa pressure and a laser intensity of 25 W/cm^2 .

There is also the alternative to use high frequency FM spectroscopy with a standard high pressure cell.

6.1.3 Optical Dipole Traps with $1.55 \mu\text{m}$ Light

We are currently trapping ultracold molecules with CO_2 laser light. As pointed out in the introduction it is attractive to be able to trap molecules at a shorter wavelength, especially when implementing optical lattice potentials. There is the option of using near-resonant light to generate an optical lattice. This has the disadvantage of off-resonant scattering losses. Far off-resonant lasers of sufficient power are available in the 1070 nm region and in the $1.55 \mu\text{m}$ region. The $1.55 \mu\text{m}$ region is especially attractive for trapping purposes because the number of molecular potentials that are reached is very limited, whereas at 1070 nm several additional potentials are addressed, see figure 3.3. Using a narrow band laser source in combination with an optical amplifier and tuning the laser frequency far from any molecular transitions, one could conveniently trap molecules at $1.55 \mu\text{m}$. 0_u^+ states are a mixture of $^1\Sigma_u^+$ and $^3\Pi_u$ states. At still longer wavelengths, below the $^1\Sigma_u^+$ minimum, in principle transitions to the $^3\Pi_u$ state and therefore transitions to the $0_u^+(P_{1/2})$ state should be forbidden from both the lowest singlet and the lowest triplet state. However, there is a small $^1\Sigma_u^+$ admixture even below its potential minimum and Feshbach molecules do not have definite g/u symmetry and therefore these transitions become allowed. The vibrational level spacing is sufficiently large in the $1.55 \mu\text{m}$ region that it should definitely not pose a problem to set the trapping laser to a wavelength far from any molecular resonance.

6.2 Transfer of Ultracold Cs Molecules to the Absolute Ground State

The ultimate goal of the present project is the efficient transfer of molecules from the vibrationally highly excited Feshbach states to the lowest rovibrational level ($v=0$, $J=0$) of the $X^1\Sigma_g^+$ ground state and the production of a stable molecular BEC.

We plan to employ a Λ -like two-photon coupling scheme, as illustrated in figure

6.2 Transfer of Ultracold Cs Molecules to the Absolute Ground State

1.1. To this end, both the Feshbach state we start from and the intermediate state have to be chosen appropriately, as discussed in section 6.2.1. Then an appropriate transfer scheme has to be set up, see section 6.2.2. In order to prevent collisional losses of the Feshbach molecules during the transfer procedure, the addition of an optical lattice to prepare precisely one molecule per lattice site is advantageous. An analogous transfer scheme is applicable to the case of heteronuclear dimers. We are most interested in ultracold Rb-Cs mixtures and the production of heteronuclear RbCs molecules, as sketched in section 6.2.4.

6.2.1 Choice of Initial and Intermediate State

Initial Feshbach State

The choice of initial Feshbach state for transfer to the absolute molecular ground state is guided by the same criteria as for the spectroscopy, discussed in sections 5.3.1 and 6.1.1. Qualitatively spoken, we would like to achieve the largest possible magnitude of the singlet component of the Feshbach molecule wave function near the inner turning point of the potential. For a quantitative analysis we have to optimize the magnitude of the dipole matrix elements reflected by the FC overlap between the ground and excited state wave functions.

It is advantageous to start from low angular momentum states, i.e. s states ($\ell = 0$) or d states ($\ell = 2$) because in a two-photon process the dipole selection rules are such that the angular momentum can change by no more than two units. Therefore, when trying to reach $J = 0$ of the $\nu = 0$ ground state level, higher ℓ states are not favorable. Due to the bosonic nature of ^{133}Cs , we only ever deal with even ℓ states.

A further option would be to increase the FC overlap by first transferring the molecules to a somewhat more tightly bound state by means of microwave transitions. Ongoing calculations will show whether this approach holds promise.

Intermediate State

We are restricted to very large detunings from the excited state asymptotes by the tuning range of the present spectroscopy laser. FC factors are higher for shorter wavelengths, which means that we want to go to the shortest wavelengths possible with our system. The intermediate rovibrational level is characterized by the vibrational and rotational quantum numbers ν'_i and J'_i , respectively. For the intermediate state, J is a good quantum number. Odd J'_i levels contain a combination of even partial waves, e.g. $J'_i = 1$ contains $\ell = 0$ and $\ell = 2$ components. For the Feshbach molecules, ℓ is a good quantum number. Intermediate levels with $J'_i = 1$ can be accessed from s ($\ell = 0$) and d ($\ell = 2$) states. The singlet component of the 0_u^+ levels in our range of interest is between 40% and 75%.

6.2.2 Transfer Scheme

Franck-Condon factors for the “second step”, i.e. for the Stokes or dump laser transition that couples the intermediate level to the $\nu = 0$ level of the $X^1\Sigma_g^+$ state are many orders of magnitude larger than for the the pump laser transition we are evaluating with the current spectroscopic experiments. They are on the order of 0.1-0.001 in the excited state region we are most interested in [Bou06]. Therefore, it would be easy to saturate the Stokes transition.

Assuming that we can drive the pump step, it is worth taking a look at the full scenario that arises. Let us assume a transition wavelength of 1515 nm (6600 cm^{-1}) for the pump step starting from the Feshbach molecules. The $X^1\Sigma_g^+ \nu = 0$ level lies $G(\nu = 0) = 20.981 \text{ cm}^{-1}$ above the potential minimum. The ground state dissociation energy of Cs_2 is $D_e(X^1\Sigma_g^+) = 3649.88 \text{ cm}^{-1}$. Therefore, the transition from the intermediate level to the $X^1\Sigma_g^+ \nu = 0$ level corresponds to a laser energy of $6600 \text{ cm}^{-1} + D_e(X^1\Sigma_g^+) - G(\nu = 0) = 10229 \text{ cm}^{-1}$. This is equivalent to a wavelength of 978 nm. The tuning range of the present spectroscopy laser from 1510 nm to 1580 nm corresponds to Stokes wavelengths of 975 nm (10253 cm^{-1}) to 1005 nm (9947 cm^{-1}). The detuning of the intermediate state from the $6S + 6P_{1/2}$ asymptote is approximately 4580 cm^{-1} .

“Parasitic” coupling of the Feshbach state to unspecified rovibrational levels in the excited state manifold by the Stokes laser as illustrated in figure 6.3 is not desirable. It opens up additional loss channels because these excited state levels spontaneously decay into free atoms or ground state levels other than $\nu = 0$. Therefore, a large level spacing in the excited state region reached by the Stokes laser from the Feshbach molecules is convenient. In the 0_u^+ potentials, level spacing is on the order of 0.3 - 1.7 nm ($1 \text{ nm} \approx 310 \text{ GHz}$) in the 980 nm region, which serves to illustrate that the level spacing is large. Naturally, all the other potentials reached in this wavelength region have to be taken into account as well but it should not be difficult to find an intermediate state such that the Stokes laser is tuned far away from any parasitic resonances. FC factors for such transitions are on the order of 10^{-6} . This has to be compared to the FC factors for the Stokes transition which are on the order of 10^{-3} , which implies that the Stokes laser intensity can be very low. Both the large level spacing and the small FC factors for parasitic transitions in comparison to the desired Stokes transition help to suppress such transitions in addition to the detuning from the parasitic resonances.

Similarly, the pump laser should not deplete the $\nu = 0$ level of the $X^1\Sigma_g^+$ state by coupling it to excited states. This requirement is easily fulfilled since the lowest rovibrational state of the $0_u^+(P_{1/2})$ state is located 8020 cm^{-1} (1247 nm) above the lowest vibrational level of the X state, which is much higher than what could be reached by the spectroscopy laser. The spacing between tightly bound excited state levels is very large and therefore it is expected that even when choosing shorter wavelengths for the pump laser, parasitic excitation from the ground state $\nu = 0$ level would not be an issue.

6.2 Transfer of Ultracold Cs Molecules to the Absolute Ground State

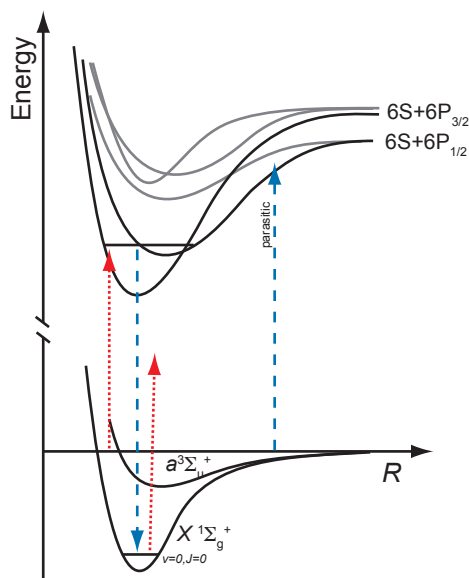


Figure 6.3: Molecular loss due to coupling to unspecified excited states: The ground state potentials and several of the electronically excited potentials are shown schematically. Two-photon transfer to the rovibrational ground state involves a pump and a Stokes laser. The Stokes laser can in principle drive optical transitions to unspecified excited state levels. The pump laser with its wavelength around $1.55 \mu\text{m}$ cannot drive any parasitic transitions from the rovibrational ground state of the $X^1\Sigma_g^+$ state because its energy is too low to reach any of the excited state potentials.

In order to increase the very small FC factors, one could choose shorter wavelengths for both the pump and the Stokes laser, resulting in smaller detuning from the excited state asymptotes. FC factors for the pump laser increase with decreasing detuning from the molecular asymptote (decreasing wavelength) whereas FC factors for the Stokes laser decrease, as illustrated in figure 6.2. In the calculations by the Orsay group [Bou06] again based on unperturbed singlet wave functions for the Feshbach molecules and coupled ab initio 0_u^+ states, FC factors for both transitions become of comparable magnitude at a pump laser wavelength of 1300 nm. There, they are around 10^{-8} . At a pump wavelength of $1.4 \mu\text{m}$, the FC factor for the pump transition is still 10^{-8} whereas the FC factor for the Stokes laser is to $\sim 10^{-4}$. Therefore, for a regime involving a single two-photon transition to the ground state, the wavelength region around $1.4 \mu\text{m} - 1.45 \mu\text{m}$ would be advantageous. A significant increase of FC factors for the pump step is predicted below 1250 nm. However, in this region, the FC factors for the Stokes laser decrease dramatically.

In addition to the 0_u^+ potentials, also the 1_u potentials have the u symmetry required for transitions to the $X^1\Sigma_g^+$ state (transitions to the 0_u^- states are forbidden). Near the potential asymptotes, the 1_u potentials arise from spin-orbit mixing of the $B^1\Pi_u$, the

6 Outlook

$2^3\Sigma_u^+$ and the $b^3\Pi_u$ states. Looking at the potential curves in figure 3.3, one can see that these potentials span a large range of internuclear distances. The inner turning point of the $1_u(P_{3/2})$ potential provides favorable FC overlap with the $X^1\Sigma_g^+(v = 0)$ level, whereas the outer turning point of the $1_u(P_{1/2})$ potential provides the overlap required for transitions from the Feshbach molecules. This effect was exploited by Sage and coworkers [Sag05] for the production of a sample of ultracold RbCs molecules by means of a two-photon transition, starting from loosely bound $a^3\Sigma^+$ molecules. Their production and detection scheme is illustrated in figure 6.4. Clearly, for a quantitative analysis, we would need the FC factors for the cesium dimer. In Cs_2 , the potential well of the $B^1\Pi_u$ state is located $13\,043.88\text{ cm}^{-1}$ above the minimum of the singlet ground state potential, i.e. at 9394 cm^{-1} above the ground state potential asymptote [NIS07]. The $B^1\Pi_u$ component is needed for coupling to the $X^1\Sigma_g^+$ state. In analogy to the case of RbCs [Ber04], vibrational levels belonging to the 1_u potentials below the $B^1\Pi_u$ potential minimum probably have some small singlet contribution. In the RbCs experiment cited above, this admixture was exploited for transfer to the ground state but for Cs_2 this hypothesis has to be checked by theoretical calculations.

Stimulated Emission Pumping

Stimulated emission pumping (SEP), see section 2.1.2, is a popular method for population transfer that does not depend on the coherence properties of the radiation field. If both the pump and the Stokes transitions can be saturated, population transfer can be 25%. If both lasers are applied at the same time, this can be increased to 1/3. SEP relies on population transfer first to the intermediate state and then to the ground state. In their study involving the transfer of RbCs molecules to the vibrational ground state, Sage and coworkers [Sag05] observed coupling of the intermediate state to unspecified higher lying states by the Stokes laser.

Although it should be easy for us to saturate the Stokes transition, we cannot hope to saturate a pump transition in the wavelength region accessible to our spectroscopy laser. The timescale for excitation from the Feshbach molecules to the intermediate state is much longer than the spontaneous emission lifetime of the intermediate state.

STIRAP

The principles of the STIRAP two-photon technique have been discussed in section 2.1.2. Its distinguishing feature is population transfer in a three-level system in such a way that the intermediate state is never actually populated. Therefore, in an ideal case no losses due to spontaneous decay of the intermediate level out of the three-level system can occur and transfer efficiency can reach unity. The transfer process can take place on a time scale much longer than the spontaneous lifetime of the intermediate state.

Population transfer is achieved by means of two temporally overlapping laser

6.2 Transfer of Ultracold Cs Molecules to the Absolute Ground State

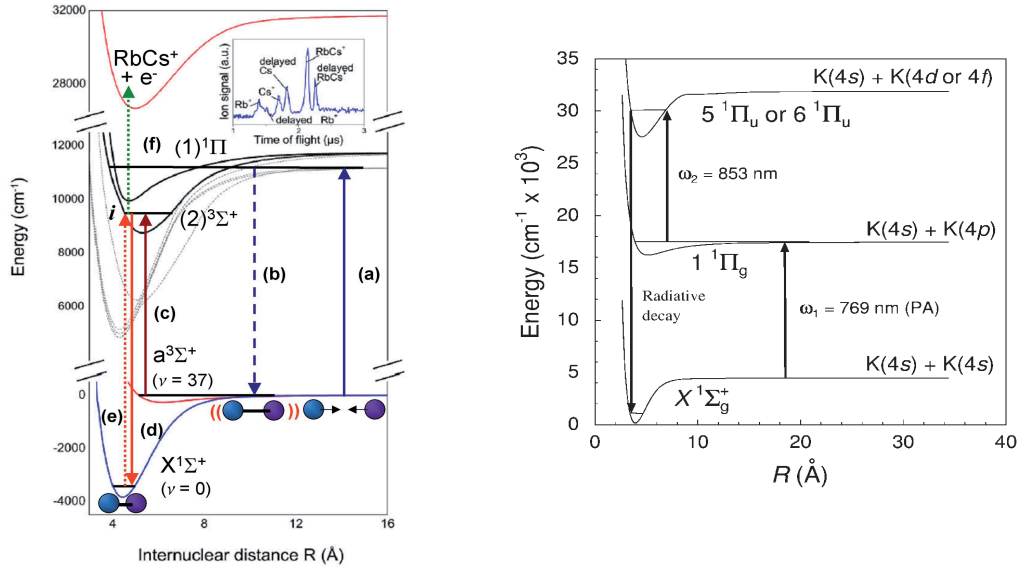


Figure 6.4: Experimental production schemes for ($\nu = 0$) ground state molecules: *left:* Production of ultracold RbCs molecules starting from loosely bound triplet molecules with a mixed $B^1\Pi_1/c^3\Sigma_1^+/b^3\Pi_1$ intermediate level as explained in section 6.2.4. Figure taken from reference [Sag05]. *right:* Three step process for the production of low lying ground vibrational states in the work by Nikolov et al. [Nik00] in the case of K_2 .

pulses with the peculiarity that the Stokes pulse is applied *before* the pump pulse. The Stokes pulse is associated with the Rabi frequency $\Omega_S(t)$ and the pump pulse with the Rabi frequency $\Omega_P(t)$. These are slowly varying functions of time according to the evolution of the pulse envelope. If the coupling is insufficient, i.e. if the Rabi frequencies are too small, some population will reach the intermediate state. From there it will spontaneously decay to states other than the initial and the desired final state [Ber98]. Population transfer via a decaying state is discussed in section 2.1.2 and in reference [Vit97]. As discussed in section 2.1.2 we performed numerical simulations of a three-level system with a “leaky” intermediate state and obtained an empirical criterion for efficient population transfer given in equation 2.6. Basically, for a given intermediate state decay rate Γ , either the Rabi frequencies must be large or the pulses must be long in order to ensure adiabaticity. If we evaluate equation 2.6 with the value of $2\pi \cdot 6$ kHz for the Rabi frequencies we obtained in section 5.3.1 and again use an intermediate state decay rate of twice the atomic value, we obtain a timescale for the STIRAP process that is on the order of 2 seconds. This is orders of magnitude longer than the spontaneous lifetime of the intermediate level and also considerably longer than the pulse durations used in a recent experiment in our group [Win06b]. Clearly, on such long time scales the phase stability of the lasers used in the STIRAP process becomes an issue. Laser phase and frequency fluctuations of the pump and Stokes

6 Outlook

laser are normally uncorrelated and lead to a detuning from the two-photon resonance required for STIRAP. Such fluctuations lead to losses due to nonadiabatic coupling [Ber98] and could be significant on such long time scales. Phase coupling between the pump and the Stokes laser by means of a frequency comb could probably alleviate this problem. On shorter time scales it is sufficient to use two independent lasers or to Pound-Drever-Hall lock two different lasers to the same optical resonator.

Optical Lattice

Feshbach molecules are inherently unstable against two-body collisions. Therefore, for efficient transfer of the whole sample to a different quantum state, the addition of an optical lattice is advantageous. The optical lattice can be prepared in such a way that lattice sites are either not occupied or occupied by precisely one molecule. The molecules are then completely shielded from inelastic collisions. Two of the experiments in our group are employing optical lattices, namely the Rb project and the Cs III experiment. In the Rb experiment, coherent transfer to a different, albeit still highly vibrationally excited, molecular vibrational level by STIRAP with $\sim 85\%$ efficiency has already been demonstrated [Win06b]. The difference in binding energy between the initial and the final state was only on the order of $600 \text{ MHz}\cdot h$ whereas for transfer to the rovibrational ground state this difference in binding energy is on the order of $100 \text{ THz}\cdot h$.

Frequency Comb

An optical frequency comb could be used to increase coherence between the pump and the Stokes laser. Probably the most convenient option would be to set up a fiber ring laser [Nel97] and then lock both the pump and the Stokes lasers to different modes of the comb. Commercially available femtosecond frequency comb systems are able to generate a spectrum that covers a region from $1050 \text{ nm} - 2100 \text{ nm}$.

6.2.3 Alternative Transfer Schemes

One alternative to population transfer by a single two-photon transition as we are currently pursuing it is a scheme consisting of two or three Λ -like two-photon transitions as suggested by Zoller and coworkers [Jak02] and illustrated in figure 6.5. For the case of Rb_2 , they discuss a process that involves two-color photoassociation in an optical lattice to produce vibrationally highly excited ground state molecules followed by two consecutive Λ -like two-photon transitions between the $X^1\Sigma_g^+$ state and the $A^1\Sigma_u^+$ state to finally reach the rovibrational ground state.

When Tiemann and coworkers studied the near-threshold structure of sodium dimers by molecular spectroscopy [Sam00, Elb99], they started from $v = 0$ ground state molecules and used two consecutive Λ -like two-photon transitions to address the molecular spectrum near the ground-state threshold.

6.2 Transfer of Ultracold Cs Molecules to the Absolute Ground State

Nikolov and colleagues [Nik00] produce tightly bound ground state molecules by a completely different scheme. First they form excited state molecules by one-color photoassociation and then transfer the molecules to a molecular Rydberg state with a second laser, see figure 6.4. The inner turning point of the latter state has significant FC overlap with low lying ground state levels which are reached by radiative decay.

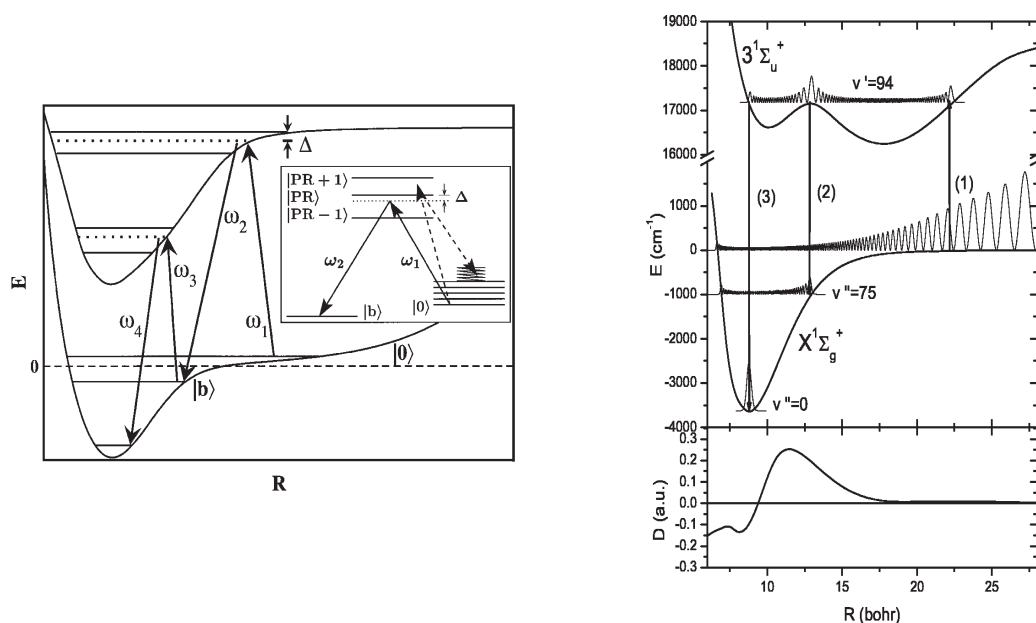


Figure 6.5: Proposed production schemes for ($v = 0$) ground state molecules: *left:* Three step process proposed by Jaksch and coworkers [Jak02]. First atoms are photoassociated inside an optical lattice. Then two consecutive two-photon transitions are applied to reach the rovibrational ground state (in the figure only two transitions are shown). *right:* Scheme proposed by Pichler and colleagues [Pic04]. Transfer from large to small internuclear distances is proposed in a single two-photon transition exploiting the double well structure of the $3^1\Sigma_u^+$ state. The lower panel gives the transition dipole function extrapolated to the case of Cs_2 from Li_2 data.

Pichler and coworkers [Pic04] propose the formation of low vibrational ground state cesium molecules by exploiting the $3^1\Sigma_u^+$ double minimum excited state, see figure 6.5. Based on ab initio potential curves calculated by Spies and Meyer and an extrapolation of transition dipole functions from the case of Li_2 , they consider the probability of photoassociation near the outer turning point of the outer well of the potential and spontaneous emission to the $v = 0$ level of the $X^1\Sigma_g^+$ ground state near the inner turning point of the inner well. They conclude that a vibrational level just above the potential barrier in the excited state ($v = 94$) is best suited for such a transition. Similar to the other schemes discussed in this section, we would use Feshbach molecu-

les as a starting point instead of free atoms. It has been observed experimentally in our group that transition rates for bound-bound transitions involving Feshbach molecules are orders of magnitude stronger than the corresponding photoassociation transitions [Win06a]. This would enhance the ground state molecule production rate. Pichler and colleagues state that driving a two-photon Raman process would be advantageous but they do not discuss the issue of the two lasers involved in such a transition coupling to other unspecified molecular levels which would introduce an additional loss channel. They calculate a photoassociation - or in our case - pump wavelength of ~ 582 nm ($17\,182$ cm^{-1}) to reach the $\nu = 94$ level of the $3^1\Sigma_u^+$ state. This corresponds roughly to a dump wavelength of 480 nm ($20\,812$ cm^{-1}) to reach the lowest vibrational level in the singlet electronic ground state. It is not clarified which states would be reached with the dump laser from the Feshbach molecules and whether the pump laser would excite the $\nu = 0$ ground state molecules.

6.2.4 Extension to Heteronuclear Systems

Heteronuclear molecules have lately received a lot of attention in the field of ultracold quantum gases. Due to their permanent electric dipole moment, they are interesting for example as qubits for quantum computing [DeM02] and in search for the electron electric dipole moment [Hud02]. One of our experiments, the GOST project, is currently pushing towards the creation of ultracold Rb-Cs mixtures and the formation of ultracold RbCs molecules. Combining this with the effort to transfer ultracold molecules to the rovibrational ground state would give us the opportunity to create a stable heteronuclear molecular BEC with a series of interesting properties.

It should be noted that the excited state potential curves for homonuclear dimers depend on the internuclear distance as $-1/R^3$ whereas for heteronuclear dimers, this dependence is $-1/R^6$. Consequently, excited state potentials are more long-range in character in homonuclear molecules. Franck-Condon factors will differ but in principle, for the low lying states, our spectroscopy and transfer scheme could easily be adapted to RbCs Feshbach molecules.

Stwalley discusses the prospects for the transfer of heteronuclear Feshbach molecules to the rovibrational ground state of the electronic ground state $X^1\Sigma^+$ [Stw04] via an intermediate state of mixed $A^1\Sigma^+/b^3\Pi$ character. Feshbach molecules have mixed $X^1\Sigma^+/a^3\Sigma^+$ character, with the a state contribution being more prominent. The author points out that due to the coincidence of the inner turning point of the $a^3\Sigma^+$ lowest triplet potential curve and the outer turning point of the $b^3\Pi$ state, FC factors should be favorable for excitation from the a triplet state. The inner turning point of the A state almost coincides with the minimum of the X state providing the necessary FC overlap for the dump step. To summarize, in this scheme, excitation occurs from the triplet ground state, then singlet/triplet mixing is exploited in the excited state and deexcitation is to the ($\nu = 0, J = 0$) level of the singlet ground state.

The potential curves given in figure 6.6 illustrate that the region around 6500 cm^{-1}

6.2 Transfer of Ultracold Cs Molecules to the Absolute Ground State

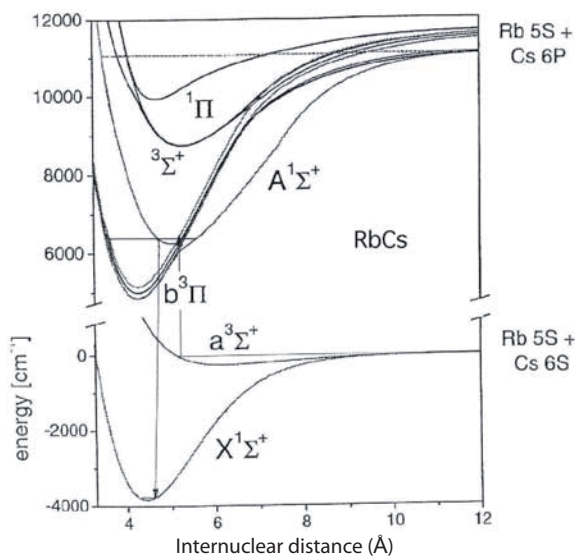


Figure 6.6: Transfer of RbCs molecules to the absolute ground state: In the transfer scheme proposed by Stwalley, excitation occurs at the inner turning point of the triplet ground state potential $a^3\Sigma^+$. Singlet/triplet mixing between the A and b electronically excited states provides the singlet character necessary for coupling to the X state. The inner turning point of the A state nearly coincides with the minimum of the X state providing favorable FC overlap with the $\nu = 0$ ground state. Figure adapted from [Stw04].

is best suited for transfer to the rovibrational ground state via a mixed $A^1\Sigma^+/b^3\Pi$ excited state level in RbCs molecules. Note that this region coincides with the region addressed by the spectroscopy laser used in the present project.

This scenario is different from the situation with homonuclear dimers. In homonuclears, the g/u symmetry precludes that these levels be accessed from the $a^3\Sigma_u^+$ triplet ground state because, just as the a state, they exhibit u symmetry and $u \rightarrow u$ transitions are dipole forbidden. The $X^1\Sigma_g^+$ state we want to populate finally has g symmetry. Selection rules require that the intermediate state has u symmetry and the initial state therefore g symmetry if we consider a single two-photon process. Feshbach molecules have mixed singlet/triplet character and mixed g/u character. For transitions to such an intermediate state, only the g component of the Feshbach molecules is relevant. The ongoing calculations by our collaborators in Orsay will clarify whether an analogous effect can be exploited in Cs_2 due to the hyperfine mixing of the X and a state. To conclude, extension of our transfer scheme to RbCs is straightforward and transfer via the mixed A/b states might be more promising in the case of heteronuclear molecules than in the case of homonuclear dimers.

Sage and colleagues [Sag05] have produced ultracold RbCs molecules in the $\nu = 0$ $X^1\Sigma^+$ state with a narrow rotational distribution and a translational temperature of

6 Outlook

$\sim 100 \mu\text{K}$ at a rate of ~ 500 molecules per second. This is clearly far away from the realization of a molecular BEC. Their stated goal is quantum computing with polar molecules. As mentioned above, they employed stimulated emission pumping for the transfer and reach a transfer efficiency of 6%. They used two-color photoassociation to produce RbCs molecules in high vibrational levels of the $a^3\Sigma^+$ state and transferred them to the lowest vibrational level of the $X^1\Sigma^+$ state in a single two-photon step. For both the pump and the dump beam they used pulsed lasers. This way, they were able to saturate transitions with FC factors down to 10^{-6} . Dipole selection rules normally prevent transitions from the triplet to the singlet manifold. They exploited mixed singlet/triplet character in the excited intermediate level. They chose a mixed $B^1\Pi_1/c^3\Sigma_1^+/b^3\Pi_1$ level detuned about 1370 cm^{-1} from the $\text{Rb}(5S_{1/2})+\text{Cs}(6P_{1/2})$ asymptote. The $c^3\Sigma_1^+$ component provides the triplet character for the pump transition (the b component, even though triplet as well, is not so important due to smaller FC factors) whereas the $B^1\Pi_1$ provides the coupling to the $X^1\Sigma^+$ state. As mentioned above, their intermediate state lies energetically below the minimum of the $B^1\Pi_1$ potential curve but still features a small $^1\Pi_1$ admixture.

APPENDIX A

Microcontroller Assembler Program

This section gives a commented version of the microcontroller assembler program for the digital laser stabilization described in section 4.2.3. A general description of the setup and of the program is given there. The device used is an atmega162 microcontroller from Atmel Corporation. The rising and the falling edge of two reference laser transmission peaks and of one spectroscopy laser transmission peak are detected in this program. The reference laser is referred to as “master”, the spectroscopy laser as “slave”. “Rising” and “falling” edge refers to the rising and falling edge of the transmission peaks as seen on the photodiodes. Due to the optocoupler at each input (H11L1) the edges are inverted in the program.

The two 16-bit timers of the microcontroller are started at the beginning of the resonator sweep by a TTL that is handled by the external interrupt 0 (INT0). The microcontroller then waits for the laser transmission peaks in a loop. When the rising or falling edge of a transmission peak occurs, it is detected by the input capture unit of that timer. The input capture units feature a digital noise canceler and save the actual timer value to the input capture registers. These registers are read out in the corresponding interrupt routines and saved to the RAM. The position of the x- and y-pointers are used to save the slave data and the master data, respectively. After saving one measured timer value, the pointers are incremented in order to point to the next free RAM address where the timer value for the next edge is stored. In the comments to the program, these timer values that do not account for any timer overflow events are referred to as “raw data”. Timer overflows are handled by a separate interrupt routine and accounted for later.

The simplest way to find out which peaks have already been detected is to query the address value the x-pointer and the y-pointer indicate. After detection of all four events for the master laser, the x-pointer points to an address 9 bytes higher than initially. The analogous is true for the slave laser. The pointer addresses are queried in order to decide whether all necessary peaks have been detected. In case all necessary values are detected and stored, the microcontroller exits the waiting loop and converts the saved timer values to ASCII-coded hexadecimal digits. To do so, timer overflows that occurred during the measurement period and that are handled by a separate interrupt routine are taken account of. Finally, the data is transmitted to the control computer through RS232. The transmitted string contains an “@” sign as attention sign, a single letter identifier before each timer value and a carriage return as termination character.

A.1 Program code

```
.include "m162def.inc" ;include definition file

.def vglm = r0 ;define register to query whether masterpeaks have been detected
.def vglsl = r1 ;define register to query whether slavepeaks have been detected
.def switchedge = r2 ;define register to quickly switch between detection of the rising
;or the falling edge of the transmission peaks using an XOR operation
.def temp1 = r16 ;define temporary working register
.def temp2 = r17 ;define temporary working register
.def temp3 = r18 ;define temporary working register
.def temp4 = r19 ;define temporary working register
.def trans1 = r20 ;define register used in serial transmission
.def umw1 = r23 ;define register used in ASCII conversion
.def umw2 = r24 ;define register used in ASCII conversion
.def overrun = r25 ;define register to handle timer overflows
.equ masterrise = 0x0100 ;SRAM address for timer value of the rising edge of first
;master peak
.equ masterfall = 0x0107 ;SRAM address for timer value of the falling edge of first
;master peak
.equ masterrise2 = 0x010E ;SRAM address for timer value of the rising edge of second
;master peak
.equ masterfall2 = 0x0115 ;SRAM address for timer value of the falling edge of sec-
ond ;master peak
.equ slaverise = 0x011C ;SRAM address for timer value of the rising edge of slave
;peak
.equ slavefall = 0x0123 ;SRAM address for timer value of the falling edge of slave
;peak
.equ masterdata = 0x012D ;SRAM address for raw data of master laser timer
.equ slavedata = 0x0142 ;SRAM address for raw data of slave laser timer
.equ CLOCK = 16000000 ;definition clock rate
.equ BAUD = 38400 ;definiton baud rate for serial transmission. the double speed
;option is set, so transmission rate is effectively 76800
.equ UBRRVAL = CLOCK/(BAUD*16)-1 ;compute value for UBRRH and UBRL
;registers

.cseg ;start of program code
.org 0x0000 ;write interrupt handler table to this location
jmp main ;reset handler
jmp int0_handler ;external interrupt 0 starts the two 16-bit timers
jmp EXT_INT1 ;not in use
jmp EXT_INT2 ;not in use
jmp PC_INT0 ;not in use
```

```

jmp PC_INT1 ;not in use
jmp TIM3_CAPT ; timer 3 input capture handler - slave laser
jmp TIM3_COMPA ;not in use
jmp TIM3_COMPB ;not in use
jmp TIM3_OVF ;timer3 overflow handler
jmp TIM2_COMP ;not in use
jmp TIM2_OVF ;not in use
jmp TIM1_CAPT ;timer1 input capture handler - master laser
jmp TIM1_COMPA ;not in use
jmp TIM1_COMPB ;not in use
jmp TIM1_OVF ;timer1 overflow handler
jmp TIM0_COMP ;not in use
jmp TIM0_OVF ;not in use
jmp SPI_STC ;not in use
jmp USART0_RXC ;not in use
jmp USART1_RXC ;not in use
jmp USART0_UDRE ;not in use
jmp USART1_UDRE ;not in use
jmp USART0_TXC ;not in use
jmp USART1_TXC ;not in use
jmp EE_RDY ;not in use
jmp ANA_COMP ;not in use
jmp SPM_RDY ;not in use

```

```

.....

```

```

main: ;start of main program
clr temp1 ;set registers to defined value
clr temp2
clr temp3

;the following sequence deletes all timeroverflows from the SRAM and is only ;rel-
;evant for the first run of the program after start up:
clr overrun ;clear register
ldi xh,high(masterrise) ;write zero to the location in the SRAM where timer overflows
;are saved
ldi xl,low(masterrise)
st x, overrun
ldi xh,high(masterfall)
ldi xl,low(masterfall)
st x, overrun
ldi xh,high(masterrise2)
ldi xl,low(masterrise2)

```

A Microcontroller Assembler Program

```
st x, overrun
ldi xh,high(masterfall2)
ldi xl,low(masterfall2)
st x, overrun
ldi xh,high(slaverise)
ldi xl,low(slaverise)
st x, overrun
ldi xh,high(slavefall)
ldi xl,low(slavefall)
st x, overrun
;
;
;set x- and y-pointer to the locations in the RAM where the raw measured data is stored
ldi xh, high(masterdata) ;x-pointer saves timer values for the master laser
ldi xl, low(masterdata)
ldi yh, high(slavedata) ;y-pointer saves timer values for the slave laser
ldi yl, low(slavedata)
;
;initialize stack pointer
ldi temp1, LOW(RAMEND) ;set stack to end of RAM
out SPL, temp1
ldi temp1, HIGH(RAMEND)
out SPH, temp1
;
;initialize serial interface (USART1)
clr temp1
ldi temp1, LOW(UBRRVAL) ;set transmission baud rate
out UBRR1L, temp1
ldi temp1, (1«URSEL)|(1«UCSZ1)|(1«UCSZ0); frame-format: 8 bit, double speed operation
out UCSR1C, temp1
clr temp1
ldi temp1, (1«TXEN1); activate transmission
out UCSR1B,temp1
in temp1,UCSR1A
ori temp1, 0b00000010
out UCSR1A, temp1
;
;initialize interrupt 0; starts timers at the beginning of the resonator sweep:
ldi temp1,0b00000010
out mcucr,temp1 ;set interrupt 0 to detection of falling edge - inverted logic due to digital optocoupler
ldi temp1,0b01000000
out gicr,temp1 ;activate INTO
```


A Microcontroller Assembler Program

```
st -x, temp1 ; ASCII 'n' for falling edge of first master peak
ldi xh,high(masterrise2)
ldi xl,low(masterrise2)
ldi temp1, 'o'
st -x, temp1 ; ASCII 'o' for rising edge of second master peak
ldi xh,high(masterfall2)
ldi xl,low(masterfall2)
ldi temp1, 'p'
st -x, temp1 ; ASCII 'p' for falling edge of second master peak
ldi xh,high(slaverise)
ldi xl,low(slaverise)
ldi temp1, 's'
st -x, temp1 ; ASCII 's' for rising edge of slave peak
ldi xh,high(slavefall)
ldi xl,low(slavefall)
ldi temp1, 't'
st -x, temp1 ; ASCII 't' for falling edge of slave peak
```

```
.....
;globally activate interrupts
sei
.....
```

```
loop: ;microcontroller waits for INTO and detection of the individual peaks in this
loop
cpse xl,vglm ;query position of x-pointer: all master peaks detected? if yes, then exit
loop
rjmp loop ;if master data is still missing, keep on waiting in the loop
cpse yl,vgl ;query position of y-pointer: slave peak completely detected? if yes, then
exit loop
rjmp loop; if slave data is still missing, stay in the loop
.....
;after completion of all measurements, continue here:
```

```
cli ;clear interrupts - no more data can be measured
.....
;switch off the timers:
in temp1, tccr1b
andi temp1, 0b11111110
out tccr1b, temp1 ;switch off timer1
lds temp1, tccr3b
andi temp1, 0b11111110
```

```

sts tccr3b, temp1 ;switch off timer3
in temp1,timsk ;bit 3 in TIMSK register to 0 disables input capture interrupt for
timer1
andi temp1, 0b11110111
out timsk, temp1
lds temp1,etimsk ;bit 5 in ETIMSK to 0 - disables input capture interrupt for timer3
andi temp1,0b11011111 ;write to registers
sts etimsk,temp1
;
ldi zh,high(masterrise) ;z-pointer is used zu fetch the overflow of the rising edge of the
first master peak and to save the ASCII coded hex digits
ldi zl,low(masterrise)
ldi xh, high(masterdata) ;x-pointer is used to fetch the saved timer values
ldi xl, low(masterdata)
rcall HexInASCII ;this subroutine fetches the overflow and the timer values and con-
verts it to a ASCII coded hex number; it expects the z-pointer to point to the overflow
and the x-pointer to the saved binary timer value, the x-pointer is then incremented
automatically, the z-pointer needs to be set to the desired address for each call
;
ldi zh,high(masterfall) ;set to address of overflow
ldi zl,low(masterfall)
rcall HexInASCII; do the conversion
ldi zh,high(masterrise2) ;set to address of overflow
ldi zl,low(masterrise2)
rcall HexInASCII
ldi zh,high(masterfall2) ;set to address of overflow
ldi zl,low(masterfall2)
rcall HexInASCII
ldi zh,high(slaverise) ;set to address of overflow
ldi zl,low(slaverise)
ldi xh, high(slavedata); set x pointer to RAM address where slave data is stored
ldi xl, low(slavedata)
rcall HexInASCII
ldi zh,high(slavefall) ;set to address of overflow
ldi zl,low(slavefall)
rcall HexInASCII
;
rcall senden ; jump to the subroutine that sends the data to the control computer over
RS232
;

```

A Microcontroller Assembler Program

```
sei; switch on the interrupts
rjmp loop; jump to loop and wait for start of resonator sweep (interrupt 0)
;.....

;-----
int0_handler: ;Starts time measurement when triggered by sync of the function gener-
ator that generates resonator sweep
in temp3, SREG ;save status register
cli; disable interrupts

ldi temp1,0b00000000 ;clear working register
out TCNT1H,temp1 ;set timer1 highbyte to 0
out TCNT1L,temp1 ;set timer1 lowbyte to 0
sts TCNT3H,temp1 ; can't use "out" here since timer3 control registers are located at
the extended I/O map
sts TCNT3L,temp1 ;set timer3 to 0

ldi temp1, 0b10000001 ;switch on noise canceller, set trigger to falling edge (inverted
logic due to optocouplers), clock without prescaler
out tccr1b, temp1 ;switch on timer1
sts tccr3b, temp1 ;switch on timer3

ldi temp2,0b00001000 ;bit 3 in TIMSK enables input capture interrupt for timer1
ldi temp1,0b00100100 ;bit 5 in ETIMSK enables input capture interrupt for timer3
out timsk,temp2 ;write to register
sts etimsk,temp1 ;write to register

ldi xh, high(masterdata) ;set x-pointer to RAM address for raw master timer values
ldi xl, low(masterdata)
clr temp1 ;clear working register
st x+,temp1 ;delete master laser data from previous run from RAM
st x+,temp1
ldi yh, high(slavedata) ;delete slave laser data from previous run from RAM
ldi yl, low(slavedata)
st y+,temp1
```

```

st y+,temp1
st y+,temp1
st y+,temp1

clr overrun ;delete timer overflows of the previous run from the RAM
ldi xh,high(masterrise)
ldi xl,low(masterrise)
st x, overrun ;clear the overflow for rising edge of the first master peak
ldi xh,high(masterfall)
ldi xl,low(masterfall)
st x, overrun
ldi xh,high(masterrise2)
ldi xl,low(masterrise2)
st x, overrun
ldi xh,high(masterfall2)
ldi xl,low(masterfall2)
st x, overrun
ldi xh,high(slaverise)
ldi xl,low(slaverise)
st x, overrun
ldi xh,high(slavefall)
ldi xl,low(slavefall)
st x, overrun
;.....;
;set the x-pointer to the RAM address for the raw master data and y-pointer to the ad-
dress for the raw slave data:
ldi xh, high(masterdata)
ldi xl, low(masterdata)
ldi yh, high(slavedata)
ldi yl, low(slavedata)
;.....;

lds temp1,etifr ;clear all interrupt flags for timer3
ori temp1,0b00111100
sts etifr,temp1
in temp1,tifr ;clear all interrupt flags for timer1
ori temp1,0b11101000
out tifr,temp1

out SREG, temp3 ;restore status register and therefore enable interrupts
reti ;return from interrupt routine
;_____

```

A Microcontroller Assembler Program

```
_____  
TIM3_CAPT: ;interrupt handler for detection of master laser peaks  
in temp3, SREG ;save status register  
cli ;clear interrupts  
lds temp1,icr3l ;read timestamp generated by input capture unit  
lds temp2,icr3h  
st x+,temp2; save to RAM: high byte before low byte  
st x+,temp1; increase x-pointer after saving for next master laser capture event  
:;switch the detection edge:  
lds temp4,tccr3b  
eor temp4,switchedge  
sts tccr3b,temp4  
:;out SREG, temp3; restore status register  
reti ;return from interrupt  
_____  
  
_____  
TIM3_OVF: ;this subroutine handles overflow events both for timer1 and timer3, it is  
executed each time there is an overflow for timer3. Since overflows for timer1 occur  
at the same time, these are handled together  
in temp3, SREG; save status register  
cli; clear interrupts  
inc overrun; increase register that counts number of overflow events  
cpi yl, 0b01000110 ;Is all slave laser data collected? Comparison of the low byte of  
the y-pointer with the low byte of the relevant RAM address  
breq masteroverflow; if the slave peak is already fully saved, then jump to the part  
handling only master overflows.  
:;if falling edge of slave has not been detected:  
cpi yl, 0b01000100 ;rising edge of slave detected?  
breq slavefallendoverflow ;if rising edge already detected, then overflow only for  
falling edge - jump there  
ldi zh, high(slaverise)  
ldi zl, low(slaverise)  
st z, overrun ;overflow for rising edge of slave peak  
slavefallendoverflow: ; overflow for falling edge of slave peak  
ldi zh, high(slavefall)  
ldi zl, low(slavefall)  
st z, overrun ;store overflow for falling slave edge
```

```

cpi xl, 0b00110101 ; both master peaks measured? if yes, skip routine for master over-
flows
breq endeoverrun
masteroverflow:
cpi xl, 0b00110001 ;true, if first master peak completely measured
breq only_peak2 ;if true, skip first master peak -> branch to second peak
cpi xl, 0b00101111 ;rising edge of first master peak detected?
breq fallingedge_peak1 ;if true, branch to falling edge of first master peak
rising_and_falling_edge_peak1:
ldi zh,high(masterrise)
ldi zl,low(masterrise)
st z, overrun; store overflow for rising edge of first master peak
fallingedge_peak1:
ldi zh,high(masterfall)
ldi zl,low(masterfall)
st z, overrun ;store overflow for falling edge of first master peak

only_peak2: ;saves overflow for second master peak
cpi xl, 0b00110011 ;rising edge of second master peak detected?
breq fallingedge_peak2 ;if rising edge already measured -> jump to falling edge
rising_and_falling_edge_peak2:
ldi zh,high(masterrise2)
ldi zl,low(masterrise2)
st z, overrun ;store overflow rising edge second master peak
fallingedge_peak2:
ldi zh,high(masterfall2)
ldi zl,low(masterfall2)
st z, overrun ;store overflow falling edge second master peak

endeoverrun:
out SREG,temp3 ;restore status register
reti ;return from interrupt
;-----
;-----
TIM1_CAPT: ;timer 1 capture interrupt: handles slave laser peak detection
in temp3, SREG ;save status register
cli ;disable interrupts
in temp1, icr1l ;read timestamp low byte
in temp2, icr1h ; read timestamp high byte
st y+, temp2 ;save timer value to RAM, highbyte before lowbyte
st y+, temp1
in temp4,tccr1b ;switch detection edge

```

A Microcontroller Assembler Program

```
eor temp4, switchege
out tccr1b, temp4
out SREG, temp3 ;restore status register and activate interrupts
reti ;return from interrupt

;-----
senden: ;subroutine that sends a string with the measured values to the control com-
puter over RS232 (USART)
in temp3, SREG ;save status register
cli ;disable interrupts
ldi xh,high(masterrise) ;set x-pointer to overflow of rising edge of first master peak
(beginning of saved data in the RAM)
ldi xl,low(masterrise)
ldi trans1,0x40 ;load '@' sign
rcall serout ; send @ via USART
ldi trans1,0x6D ; load ASCII 'm': indicates rising edge of masterpeak 1
rcall serout ; send 'm' via USART
;.....
senden2:
ld trans1,x+ ; start reading data from the RAM, increase pointer
cpi xl,0x2A ;compare pointer address with stop value
breq ende1 ;if stop value in RAM reached, branch to ende1
rcall serout ; send data from RAM as long the pointer is below the specified stop value
rjmp senden2 ;stay in sending loop
;.....
ende1:
ldi trans1, 0x0D
rcall serout ;sends carriage return via USART
;clear overflows from RAM:
clr overrun
ldi xh,high(masterrise)
ldi xl,low(masterrise)
st x, overrun
ldi xh,high(masterfall)
ldi xl,low(masterfall)
st x, overrun
ldi xh,high(masterrise2)
ldi xl,low(masterrise2)
st x, overrun
ldi xh,high(masterfall2)
ldi xl,low(masterfall2)
st x, overrun
ldi xh,high(slaverise)
```

```

ldi x1,low(slaverise)
st x, overrun
ldi xh,high(slavefall)
ldi x1,low(slavefall)
st x, overrun
out SREG, temp3 ;restore status register
ret ;return
;-----
serout: ;sends single bytes to the USART
sbis UCSR1A,UDRE1 ;wait until USART is ready for next byte
rjmp serout ;waiting loop
out UDR1, trans1 ;write to USART data register

ret ;return to calling routine

;-----
HexInASCII:
in temp3, SREG
cli
ld temp1,z ;overflow of the respective peak/edge
ld temp2,x+ ;highbyte of ICR
ld temp4,x+ ; lowbyte of ICR
rcall HexInASCIa ; adds ASCII offset to overflow
mov temp1,temp2
rcall HexInASCIa ; adds ASCII offset to both nibbles of high byte
mov temp1,temp4
rcall HexInASCIa ;adds ASCII offset to both nibbles of low byte
out SREG, temp3 ;restore status register
ret ;return to calling routine

HexInASCIa:
mov umw1,temp1 ;copy result to umw1
swap umw1 ;swap nipples
cbr umw1,$F0 ;delete higher half byte
subi umw1,-$30 ;add ASCII offset to number
cpi umw1,$3A ;ASCII-code > $39 ($39 = '9')?
brlo AH1 ;jump, if not
sbci umw1,-$07 ;add additional offset for letter
AH1:
mov umw2,temp1 ;copy character to umw2
cbr umw2,$F0
subi umw2,-$30
cpi umw2,$3A

```

A Microcontroller Assembler Program

```
brlo AH2
sbcu umw2,-$07
AH2:
st z+,umw1 ;save ASCII character to RAM and increase pointer (ASCII-codes of hex
number in umw1:umw2)
st z+,umw2
ret
;.....
```

```
EXT_INT1: reti ; IRQ1 Handler
EXT_INT2: reti ; IRQ2 Handler
PC_INT0: reti ; PCINT0 Handler
PC_INT1: reti ; PCINT1 Handler
TIM3_COMPA: reti ; Timer3 CompareA Handler
TIM3_COMPB: reti ; Timer3 CompareB Handler
TIM2_COMP: reti ; Timer2 Compare Handler
TIM2_OVF: reti ; Timer2 Overflow Handler
TIM1_COMPA: reti ; Timer1 CompareA Handler
TIM1_COMPB: reti ; Timer1 CompareB Handler
TIM1_OVF: reti ;not used, overflow handled by TIM3_OVF
TIM0_COMP: reti ; Timer0 Compare Handler
TIM0_OVF: reti ; Timer0 Overflow Handler
SPI_STC: reti ; SPI Transfer Complete Handler
USART0_RXC: reti ; USART0 RX Complete Handler
USART1_RXC: reti ; USART1 RX Complete Handler
USART0_UDRE: reti ; UDR0 Empty Handler
USART1_UDRE: reti ; UDR1 Empty Handler
USART0_TXC: reti ; USART0 TX Complete Handler
USART1_TXC: reti ; USART1 TX Complete Handler
EE_RDY: reti ; EEPROM Ready Handler
ANA_COMP: reti ; Analog Comparator Handler
SPM_RDY: reti ; Store Program Memory Ready Handler
```

APPENDIX B

Primer on Resonator Optics

In its simplest implementation, an optical resonator consists of two highly reflective mirrors facing each other. We use optical resonators that consist of one flat mirror and one curved mirror.

The condition for mode matching between a Gaussian beam and an optical resonator of given length and mirror curvature will be given in this section. There is a simple stability criterion that has to be obeyed when designing an optical resonator. The optical characteristics are determined by the finesse and the free spectral range. Finally, one has to consider the spectral position of unwanted non-Gaussian higher modes. These should not overlap spectrally with the Gaussian modes' line profile.

A very nice introduction to resonator optics is given in the book by Saleh and Teich [Sal91]. Light is coupled into the resonator through one of the mirrors and is then reflected back and forth between the two mirrors. During one resonator round trip the light acquires a certain phase depending on the distance between the mirrors. If the phase acquired during one round trip is a multiple of 2π , constructive interference can occur with each round trip and the intensity in the resonator builds up. The resonance condition means that the resonator length must be equal to an integer multiple of the half wavelength.

The resonators we use are composed of one flat and one curved mirror. Such a system can be analyzed most conveniently in the framework of Gaussian beam optics. A Gaussian beam is characterized by its Gaussian intensity distribution:

$$I(\rho, z) = I_0 \left[\frac{W_0}{W(z)} \right]^2 \exp \left[-\frac{2\rho^2}{W^2(z)} \right] \quad (\text{B.1})$$

where ρ is the radial distance from the axis of propagation and z is the coordinate along this axis with the focus defining the zero position. W_0 is the radius or waist of the Gaussian beam in the focus and $W(z)$ is the width as a function of the axial distance. $W(z)$ increases with distance from the focus on a scale set by the characteristic range, the Rayleigh range z_0 :

$$W(z) = W_0 \left[1 + \left(\frac{z}{z_0} \right)^2 \right]^{1/2}. \quad (\text{B.2})$$

The Rayleigh range is related to the beam waist radius by

$$z_0 = \pi \frac{W_0^2}{\lambda}. \quad (\text{B.3})$$

B Primer on Resonator Optics

In a Gaussian beam, the wavefronts are plane for $z = 0$, that is in the focus, which means that the radius of curvature is infinite. The radius of curvature of the wavefronts evolves with z according to the relation

$$R(z) = z + \frac{z_0^2}{z}. \quad (\text{B.4})$$

For spherical mirror resonators, equation B.4 is important because the idea is to match the curvature of the wavefronts to the curvatures R_1 and R_2 of the mirrors at positions z_1 and z_2 separated by a distance $d = |z_2 - z_1|$.

A short calculation yields the Gaussian beam's Rayleigh range required for mode matching between a given resonator and a Gaussian beam:

$$z_0^2 = \frac{-d(R_1 + d)(R_2 + d)(R_1 + R_2 + d)}{(R_1 + R_2 + 2d)^2}. \quad (\text{B.5})$$

For a given wavelength, the Rayleigh range fully characterizes the beam and the beam radii at the mirrors are

$$W_i = W_0 \left[1 + \left(\frac{z_i}{z_0} \right)^2 \right]^{1/2}, \quad i = 1, 2. \quad (\text{B.6})$$

In order for z_0 to be real as required for a confined solution that represents indeed a Gaussian beam, z_0^2 from equation B.5 must be greater than zero. This condition can be restated in order to give a useful expression for the confinement condition for an optical resonator:

$$0 \leq \left(1 + \frac{d}{R_1} \right) \left(1 + \frac{d}{R_2} \right) \leq 1. \quad (\text{B.7})$$

The quantity $\left(1 + \frac{d}{R_i} \right)$ is often abbreviated as g_i . The confinement condition then becomes $0 \leq g_1 g_2 \leq 1$.

The resonators used here consist of one spherical mirror with radius of curvature $R = -250$ mm, where the minus sign indicates concave curvature, and one flat mirror with $R = \infty$ at a distance of $d = 100$ mm. The value of the confinement parameter is therefore $g_1 g_2 = 0.6$.

An important quantity that characterizes an optical resonator is the finesse \mathfrak{F} . The finesse is a measure of contrast of the resonator. If the finesse is high, the resonances are sharp peaks. Put more quantitatively, the finesse is related to the round trip amplitude attenuation factor τ according to

$$\mathfrak{F} = \frac{\pi \tau^{1/2}}{1 - \tau} \quad (\text{B.8})$$

The amplitude attenuation factor τ stems from mirror reflectivity below 100% and from absorption in the medium. The intensity attenuation factor is τ^2 .

We are using mirrors with an intensity reflection coefficient of 99.7%. Reflection on

two mirrors yields a round trip intensity attenuation factor of 0.997^2 and correspondingly a round trip amplitude attenuation factor of 0.997. The calculated finesse \mathfrak{F} is therefore 1046. The finesse has important implications for the spectral width $\delta\nu$ of the cavity resonances:

$$\delta\nu \approx \frac{\nu_F}{\mathfrak{F}} \quad \text{for } \mathfrak{F} \gg 1. \quad (\text{B.9})$$

As will be discussed in the next section, ν_F is the spectral spacing between two adjacent resonances of the optical cavity. A high finesse assures spectrally narrow resonances. For $\nu_F = 1.5$ GHz as used in the present study a finesse of 1000 yields resonances with a full-width-half-maximum (FWHM) width of 1.5 MHz.

Resonator Modes

The phase of a Gaussian beam is

$$\varphi(\rho, z) = kz - \zeta(z) + \frac{k\rho^2}{2R(z)} \quad (\text{B.10})$$

where $\zeta(z) = \tan^{-1}(z/z_0)$. All points on a wavefront by definition share the same phase, and, due to the mode matching condition, at the position of the mirror the curvature of the wavefronts equals the curvature of the mirror. Therefore, all points on the mirror share the same phase. As the beam propagates from mirror 1 to mirror 2, the phase changes by

$$\Delta\varphi = kd - \Delta\zeta \quad (\text{B.11})$$

where $\Delta\zeta = \zeta(z_2) - \zeta(z_1)$, z_i indicating the position of mirror i . The condition that the beam must retrace itself for constructive interference with each roundtrip implies that the round-trip phase change must be equal to an integer multiple of 2π , i.e. $2kd - 2\Delta\zeta = 2\pi q$, $q = 0, \pm 1, \pm 2, \dots$

With $k = 2\pi\nu/c$ and $\nu_F = c/2d$, the condition for the resonance frequencies ν_q of the resonator becomes

$$\nu_q = q\nu_F + \frac{\Delta\zeta}{\pi}\nu_F. \quad (\text{B.12})$$

Adjacent modes are spaced by $\nu_F = c/2d$. Therefore, the quantity ν_F is called the “free spectral range”, often abbreviated as “FSR”. The free spectral range is an important characteristic of the resonator.

Similar to the Gaussian modes, there are further solutions to the equation that underlies beam optics, namely the paraxial Helmholtz equation, that retrace themselves after each round trip in the resonator. These are the Hermite-Gaussian modes with resonance frequencies $\nu_{l,m,q}$ according to

$$\nu_{l,m,q} = q\nu_F + (l + m + 1)\frac{\Delta\zeta}{\pi}\nu_F, \quad (\text{B.13})$$

where the integers (l, m) characterize the intensity distribution of these so-called *transverse* or *higher modes*. The $(0, 0)$ -mode is identical to the Gaussian mode discussed

B Primer on Resonator Optics

above. Different values for q designate different *longitudinal modes*.

The significance of equation B.13 for designing an optical resonator lies in the fact that none of the first few higher modes should coincide with the $(0, 0)$ -mode since this would result in a distortion of the $(0, 0)$ -resonance. A configuration where all the higher modes are brought into degeneracy with the Gaussian mode is called confocal resonator.

APPENDIX C

Alignment Instructions for Wavemeter

The following section gives quick and easy instructions to adjust a Michelson wavemeter of the type we use in the present study, see section 4.1.3. The setup is illustrated in figure 4.4. The aim is to have both arms of the interferometer adjusted in such a way that the beams travel exactly parallel to the rail, which means that the beams do not alter their direction when the slide is moving. In addition, both beams must be superimposed on the beamsplitter and the photodiodes. Mirrors are designated m_1 through m_7 as indicated in figure 4.4.

The reference beam is collimated with a C220 TM-B lens from Thorlabs with focal length $f = 11$ mm and 5.5 mm clear aperture. The resulting waist W_0 is ~ 1 mm, resulting in a Rayleigh range of $z_0 \simeq 3.7$ m. Mirrors m_1 and m_2 couple the reference laser into the interferometer. In a first step, they are adjusted so that the beam runs parallel to the base of the wavemeter and roughly parallel to the rail. The beam should hit the beamsplitter in its upper portion to leave enough room for the returning beam that travels 10 to 15 mm below. The beam transmitted through the beamsplitter hits mirrors m_3 , m_4 and the retroreflector. Mirrors m_3 and m_4 should be adjusted such that the beam hits the retroreflector slightly above the center and returns to these same mirrors and the beamsplitter below the original beam. With the air flow for the rail turned on, one can move the slide from one end of the rail to the other and adjust the mirrors in such a way that the beam does not change its position when the slide is moved. To accomplish this, it is useful to block the slide in one position and adjust one mirror, then move the slide to the other extreme of the rail and adjust the other mirror. When the slide is near m_4 , adjust m_3 ; when the slide is near m_7 , adjust m_4 . Once the beam does not move appreciably any more, the second arm of the interferometer can be adjusted. There is one additional mirror m_5 in this arm. The procedure is the same as for the first arm of the interferometer. When the slide is near m_7 , the two mirrors m_5 and m_6 should be adjusted, when the slide is near m_4 , mirror m_7 should be adjusted. With each iteration cycle, one can switch between m_5 and m_6 . After this coarse adjustment, a 4-quadrant-photodiode (4Q-PD) is helpful for the fine tuning. The X- and Y-outputs of such a photodiode reflect the deviation of the beam position from the center of the device and can be used conveniently to visualize the beam position on an oscilloscope. Place the 4Q-PD at the position of the lambda-meter's detection photodiodes and repeat the same procedure as outlined for the coarse tuning. Once the reference laser is adjusted in this way, the "reference" photodiodes of the wavemeter

C Alignment Instructions for Wavemeter

should give an interference signal of constant contrast along the whole length of the rail. If the contrast of the interference signal changes when the retroreflectors move, adjustment is not optimal. After adjustment of the reference beam, the beam to be measured is coupled into the wavemeter by coupling the reference laser into the fiber that delivers the spectroscopy light. The fiber collimator of this fiber is adjusted to give a collimated beam at the wavelength of the spectroscopy laser.

APPENDIX D

Circuit Diagrams

D.1 Temperature Stabilization of Optical Resonators

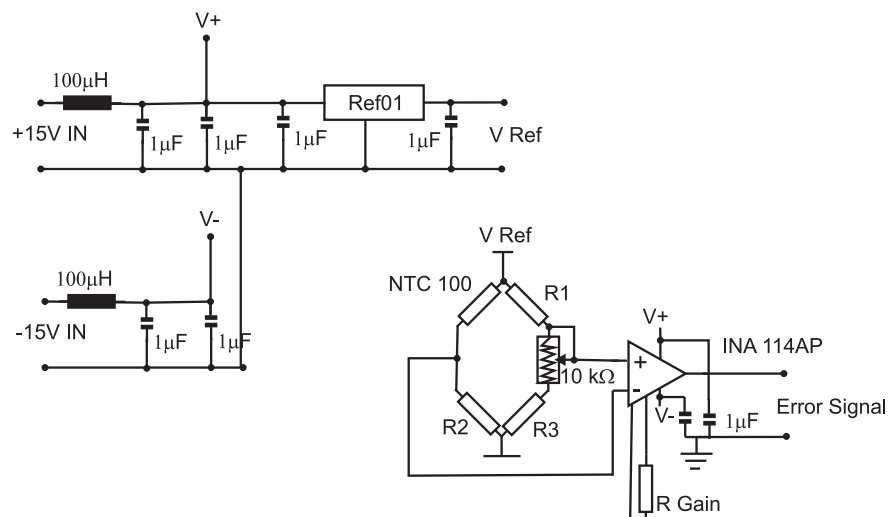


Figure D.1: Temperature measurement bridge: Prestabilization resonator, inner temperature stabilization: $R_1 = 80 \text{ K}\Omega \parallel 1 \text{ M}\Omega$, $R_2 = R_3 = 100 \text{ K}\Omega$, $R_{gain} = 100 \text{ }\Omega$, gain 500. Prestabilization resonator, outer temperature stabilization: $R_1 = 100 \text{ K}\Omega \parallel 1 \text{ M}\Omega$, $R_2 = R_3 = 100 \text{ K}\Omega$, $R_{gain} = 100 \text{ }\Omega$, gain 500. Scan lock resonator: $R_1 = 80 \text{ K}\Omega \parallel 1 \text{ M}\Omega$, $R_2 = R_3 = 100 \text{ K}\Omega$, $R_{gain} = 249 \text{ }\Omega$, gain 200. All resistors used are precision resistors (0.1% tolerance).

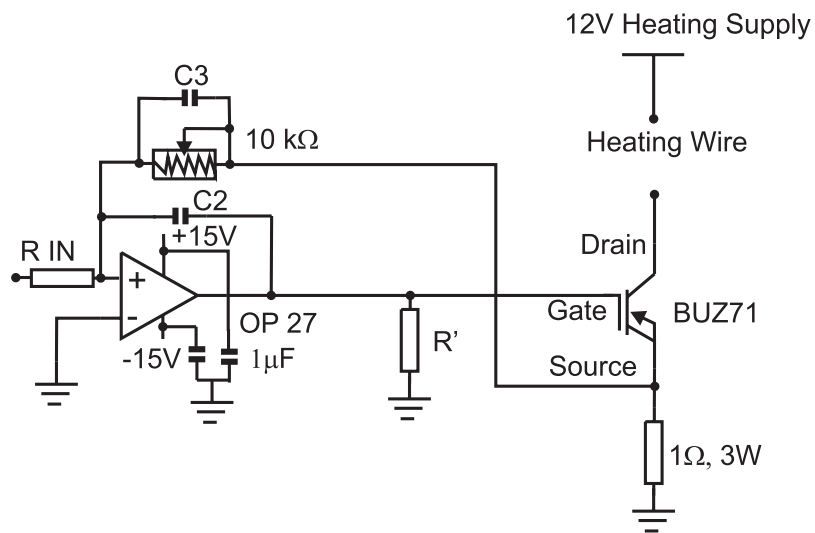
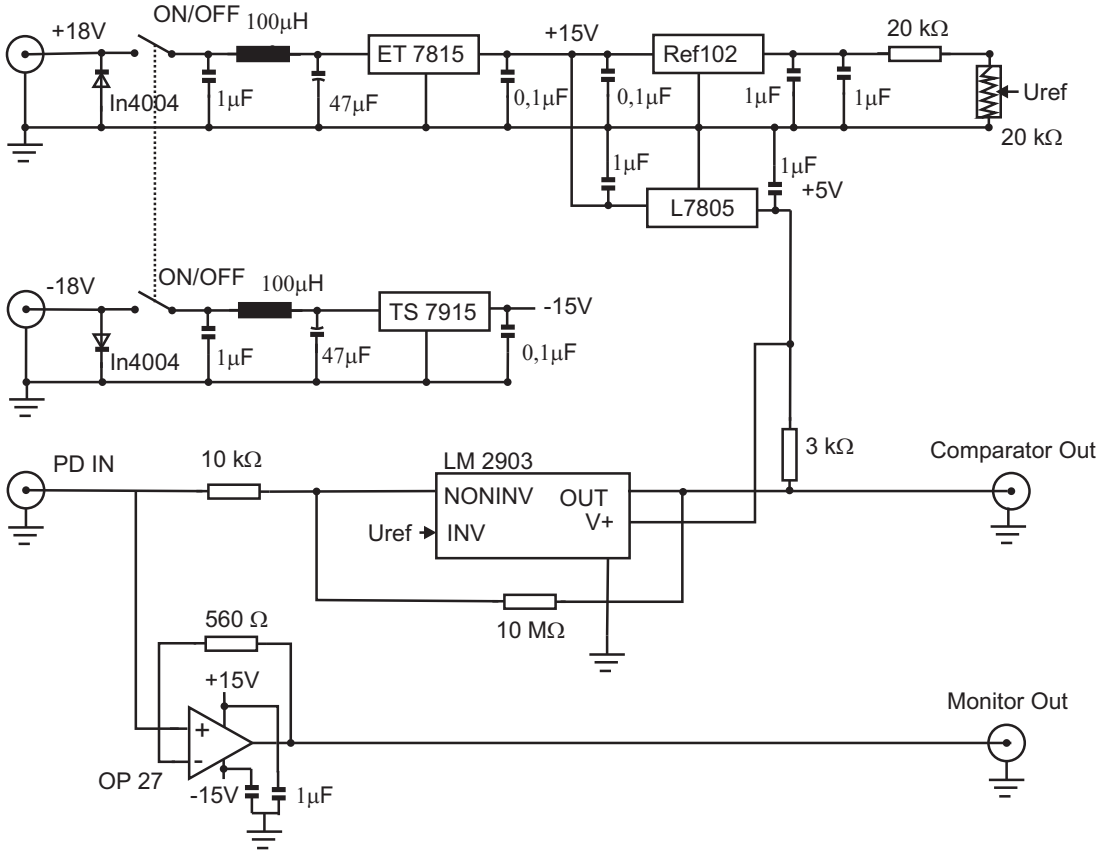
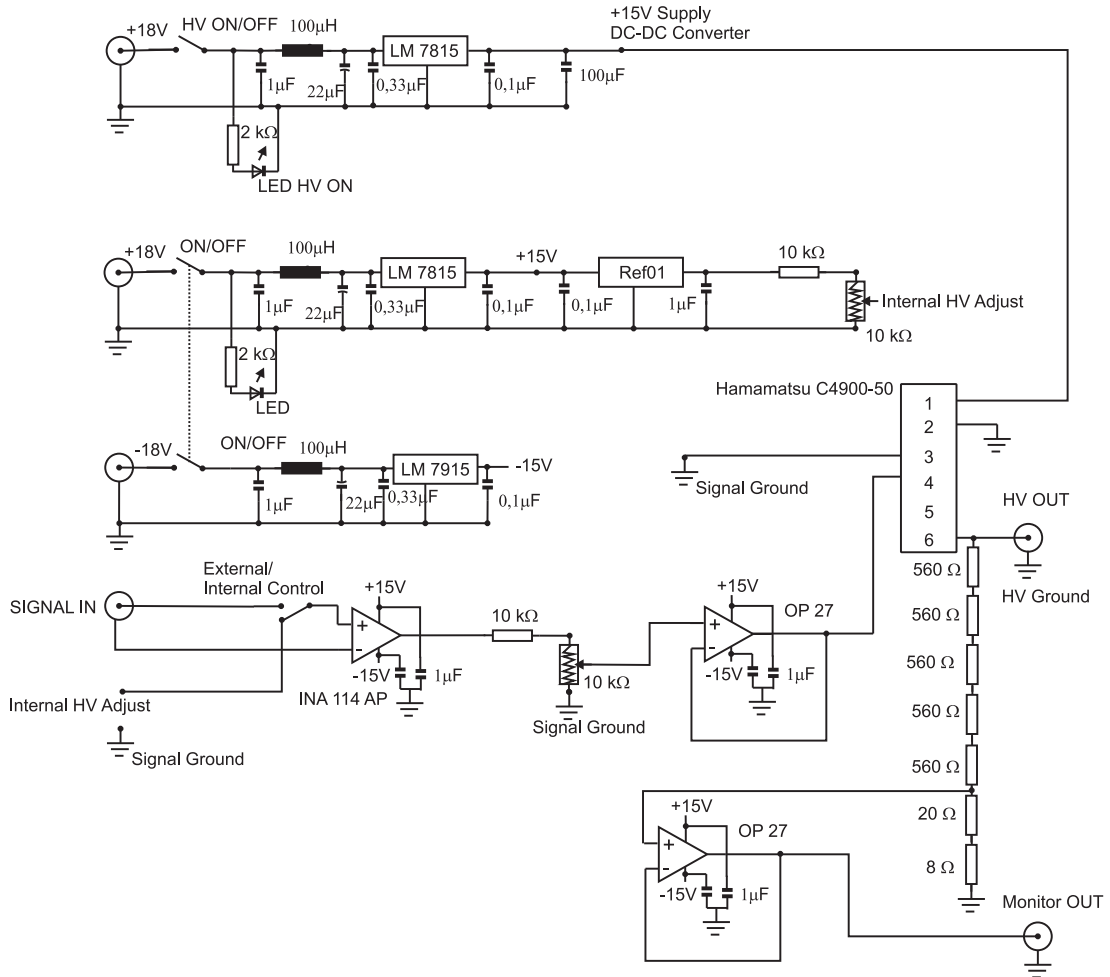


Figure D.2: Power stage of temperature PID servo.

D.2 Comparator Circuits



D.3 High-Voltage DC-DC Converter



References

- [Ami88a] C. Amiot, *The Cs₂ (3)¹Π_u electronic state pumped by Ar⁺ laser lines*, J.Chem.Phys. **89**, 3993 (1988).
- [Ami88b] C. Amiot, W. Demtröder, and C. Vidal, *High resolution Fourier spectroscopy and laser spectroscopy of Cs₂: The 2¹Σ_g⁺, (C)2¹Π_u, (D)2¹Σ_u⁺, 3¹Σ_g⁺, and (E)3¹Σ_u⁺ electronic states*, J.Chem.Phys. **88**, 5265 (1988).
- [Ami99] C. Amiot, O. Dulieu, and J. Vergès, *Resolution of the Apparent Disorder of the Rb₂ A¹Σ_u⁺(0_u⁺) and b³Π_u(0_u⁺) Spectra: A case of Fully Coupled Electronic States*, Phys. Rev. Lett. **83**, 2316 (1999).
- [Ami02] C. Amiot and O. Dulieu, *The Cs₂ ground electronic state by Fourier transform spectroscopy: Dispersion coefficients*, Journal of Chemical Physics **117**, 5155 (2002).
- [And95] M. H. Anderson, J. R. Ensher, M. R. Matthews, C. E. Wieman, and E. A. Cornell, *Observation of Bose-Einstein Condensation in a Dilute Atomic Vapor*, Science **269**, 198 (1995).
- [And97] M. R. Andrews, C. G. Townsend, H.-J. Miesner, D. S. D. and D. M. Kurn, and W. Ketterle, *Observation of Interference Between Two Bose-Einstein Condensates*, Science **275**, 637 (1997).
- [AS01] J. R. Abo-Shaeer, C. Raman, J. M. Vogels, and W. Ketterle, *Observation of Vortex Lattices in Bose-Einstein Condensates*, Science **292**, 476 (2001).
- [Bal05] P. Balling, M. Fischer, P. Kubina, and R. Holzwarth, *Absolute frequency measurement of wavelength standard at 1542nm: acetylene stabilized DFB laser*, Optics Express **13**, 9196 (2005).
- [Bar04a] M. Bartenstein, A. Altmeyer, S. Riedl, S. Jochim, C. Chin, J. H. Denschlag, and R. Grimm, *Collective excitations of a degenerate gas at the BEC-BCS crossover*, Phys. Rev. Lett. **92**, 203201 (2004).
- [Bar04b] M. Bartenstein, A. Altmeyer, S. Riedl, S. Jochim, C. Chin, J. H. Denschlag, and R. Grimm, *Crossover from a molecular Bose-Einstein condensate to a degenerate Fermi gas*, Phys. Rev. Lett. **92**, 120401 (2004).
- [Ber98] K. Bergmann, H. Theuer, and B. W. Shore, *Coherent population transfer among quantum states of atoms and molecules*, Rev. Mod. Phys. **70**, 1003 (1998).
- [Ber01] F. Bertinetto, P. Cordiale, G. Galzerano, and E. Bava, *Frequency Stabilisation of DBR Diode Laser Against Cs Absorption Lines at 852 nm Using the Modulation Transfer Method*, IEEE **50**, 490 (2001).

References

- [Ber04] T. Bergeman, A. Kerman, J. Sage, S. Sainis, and D. DeMille, *Prospects for production of ultracold RbCs molecules*, The European Physical Journal D-Atomic, Molecular and Optical Physics **31**, 179 (2004).
- [Bet99] H. L. Bethlem, G. Berden, and G. Meijer, *Decelerating Neutral Dipolar Molecules*, Phys. Rev. Lett. **83**, 1558 (1999).
- [Bet00] H. L. Bethlem, G. Berden, F. M. H. Crompvoets, R. Jongma, A. J. A. van Roij, and G. Meijer, *Electrostatic trapping of ammonia molecules*, Nature **406**, 491 (2000).
- [Bir94] K. Birch and M. Downs, *Correction to the updated Edlén equation for the refractive index of air*, Metrologia **31**, 315 (1994).
- [Bla00] G. Blasbichler, *Ein Lambdameter mit 10^{-7} Messunsicherheit*, Master's thesis, University of Innsbruck (2000).
- [Bos24] S. Bose, *Plancks Gesetz und Lichtquantenhypothese*, Z. Phys. **26**, 178 (1924).
- [Bou06] N. Bouloufa and O. Dulieu, private communication (2006).
- [Bra95] C. C. Bradley, C. A. Sackett, J. J. Tollett, and R. G. Hulet, *Evidence of Bose-Einstein Condensation in an Atomic Gas with Attractive Interactions*, Phys. Rev. Lett. **75**, 1687 (1995), *ibid.* **79**, 1170 (1997).
- [Bra97] C. C. Bradley, C. A. Sackett, and R. G. Hulet, *Bose-Einstein Condensation of Lithium: Observation of Limited Condensate Number*, Phys. Rev. Lett. **78**, 985 (1997).
- [Bur99] S. Burger, K. Bongs, S. Dettmer, W. Ertmer, K. Sengstock, A. Sanpera, G. V. Shlyapnikov, and M. Lewenstein, *Dark Solitons in Bose-Einstein Condensates*, Phys. Rev. Lett. **83**, 5198 (1999).
- [Bur02] K. Burnett, P. S. Julienne, P. D. Lett, E. Tiesinga, and C. J. Williams, *Quantum encounters of the cold kind*, Nature **416**, 225 (2002).
- [Chi00] C. Chin, V. Vuletić, A. J. Kerman, and S. Chu, *High Resolution Feshbach Spectroscopy of Cesium*, Phys. Rev. Lett. **85**, 2717 (2000).
- [Chi01] C. Chin, *Cooling, Collisions and Coherence of Cold Cesium Atoms in a Trap*, Ph.D. thesis, Stanford University (2001).
- [Chi04a] C. Chin, M. Bartenstein, A. Altmeyer, S. Riedl, S. Jochim, J. H. Denschlag, and R. Grimm, *Observation of the pairing gap in a strongly interacting Fermi gas*, Science **305**, 1128 (2004).
- [Chi04b] C. Chin, V. Vuletic, A. J. Kerman, S. Chu, E. Tiesinga, P. J. Leo, and C. J. Williams, *Precision Feshbach spectroscopy of ultracold Cs₂*, Physical Review A **70**, 032701 (2004).
- [Chu98] S. Chu, *The manipulation of neutral particles*, Rev. Mod. Phys. **70**, 685 (1998).

- [Cid96] P. Ciddor, *Refractive index of air: new equations for the visible and near infrared*, Appl. Optics **35**, 1566 (1996).
- [Com00] D. Comparat, C. Drag, B. Laburthe Tolra, A. Fioretti, P. Pillet, A. Crubellier, O. Dulieu, and F. Masnou-Seeuws, *Formation of cold Cs₂ ground state molecules through photoassociation in the 1_u pure long-range state*, Eur. Phys. J. D **11**, 59 (2000).
- [Cor99] E. A. Cornell, J. R. Ensher, and C. E. Wieman, *Experiments in dilute atomic Bose-Einstein condensation*, in: M. Inguscio, S. Stringari, and C. E. Wieman (Eds.), *Proceedings of the International School of Physics - Enrico Fermi*, 15, IOS Press, 1999.
- [Cor00] S. L. Cornish, N. R. Claussen, J. L. Roberts, E. A. Cornell, and C. E. Wieman, *Stable ⁸⁵Rb Bose-Einstein Condensates with Widely Tunable Interactions*, Phys. Rev. Lett. **85**, 1795 (2000).
- [Cor02] E. A. Cornell and C. E. Wieman, *Nobel Lecture: Bose-Einstein condensation in a dilute gas, the first 70 years and some recent experiments*, Rev. Mod. Phys. **74**, 875 (2002).
- [CT98] C. N. Cohen-Tannoudji, *Manipulating atoms with photons*, Rev. Mod. Phys. **70**, 707 (1998).
- [CT99] C. Cohen-Tannoudji, B. Diu, and F. Laloë, *Quantenmechanik*, Walter de Gruyter, 1999.
- [Cub03] J. Cubizolles, , T. Bourdel, S. J. J. M. F. Kokkelmans, G. V. Shlyapnikov, and C. Salomon, *Production of Long-Lived Ultracold Li₂ Molecules from a Fermi Gas*, Phys. Rev. Lett. **91**, 240401 (2003).
- [Dal99] F. Dalfovo, S. Giorgini, L. P. Pitaevskii, and S. Stringari, *Theory of Bose-Einstein condensation in trapped gases*, Rev. Mod. Phys. **71**, 463 (1999).
- [Dav95] K. B. Davis, M.-O. Mewes, M. R. Andrews, N. J. van Druten, D. Durfee, D. M. Kurn, and W. Ketterle, *Bose-Einstein Condensation in a Gas of Sodium Atoms*, Phys. Rev. Lett. **75**, 3969 (1995).
- [Day93] T. Day, F. Luecke, and M. Brownell, *Continuously tunable diode lasers*, Lasers and Optronics 15–17 (1993).
- [DeM02] D. DeMille, *Quantum Computation with Trapped Polar Molecules*, Phys. Rev. Lett. **88**, 067901 (2002).
- [Dem05] W. Demtröder, *Molecular Physics*, Wiley-VCH, 2005, 1st ed.
- [Den00] J. Denschlag, J. E. Simsarian, D. L. Feder, C. W. Clark, L. A. Collins, J. Cubizolles, L. Deng, E. W. Hagley, K. H. W. P. Reinhardt, S. L. Rolston, B. I. Schneider, and W. D. Phillips, *Generating Solitons by Phase Engineering of a Bose-Einstein Condensate*, Science **287**, 97 (2000).

References

- [Dio01] C. M. Dion, C. Drag, O. Dulieu, B. Laburthe Tolra, F. Masnou-Seeuws, and P. Pillet, *Resonant Coupling in the Formation of Ultracold Ground State Molecules via Photoassociation*, Phys. Rev. Lett. **86**, 2253 (2001).
- [Don02] E. A. Donley, N. R. Claussen, S. T. Thompson, and C. Wieman, *Atom-molecule coherence in a Bose-Einstein condensate*, Nature **417**, 529 (2002).
- [Dre83] R. Drever, J. Hall, F. Kowalski, J. Hough, G. Ford, A. Munley, and H. Ward, *Laser phase and frequency stabilization using an optical resonator*, Applied Physics B: Lasers and Optics **31**, 97 (1983).
- [Dul04] O. Dulieu, *Workshop on Cold Molecules - Lecture*, Les Houches (2004).
- [Dul06] O. Dulieu, private communication (2006).
- [Dür04] S. Dürr, T. Volz, A. Marte, and G. Rempe, *Observation of Molecules Produced from a Bose-Einstein Condensate*, Phys. Rev. Lett. **92**, 020406 (2004).
- [Edl66] B. Edlén, *The refractive index of air*, Metrologia **2**, 71 (1966).
- [Edw04] C. Edwards, H. Margolis, G. Barwood, S. Lea, P. Gill, G. Huang, and W. Rowley, *Absolute frequency measurement of a 1.5- μm acetylene standard by use of a combined frequency chain and femtosecond comb*, Optics Letters **29**, 566 (2004).
- [Ein25] A. Einstein, *Quantentheorie des einatomigen idealen Gases. Zweite Abhandlung*, Sitzungsber. Preuss. Akad. Wiss. **1925**, 3 (1925).
- [Elb99] M. Elbs, H. Knöckel, T. Laue, C. Samuelis, and E. Tiemann, *Observation of the last bound levels near the Na_2 ground-state asymptote*, Phys. Rev. A **59**, 3665 (1999).
- [Fio98] A. Fioretti, D. Comparat, A. Crubellier, O. Dulieu, F. Masnou-Seeuws, and P. Pillet, *Formation of Cold Cs_2 Molecules through Photoassociation*, Phys. Rev. Lett. **80**, 4402 (1998).
- [Fio99] A. Fioretti, D. Comparat, C. Drag, C. Amiot, O. Dulieu, F. Masnou-Seeuws, and P. Pillet, *Photoassociative spectroscopy of the Cs_2 0_g^- long range state*, European Physical Journal D **5**, 389 (1999).
- [Fri98] D. G. Fried, T. C. Killian, L. Willmann, D. Landhuis, S. C. Moss, D. Kleppner, and T. J. Greytak, *Bose-Einstein Condensation of Atomic Hydrogen*, Phys. Rev. Lett. **81**, 3811 (1998).
- [Ger99] M. Gertszov and M. Rosenbluh, *Injection Locking of a Diode Laser Locked to a Zeeman Frequency Stabilized Laser Oscillator*, Opt. Comm. **170**, 269 (1999).
- [Gib93] K. Gibble and S. Chu, *Laser-Cooled Cs Frequency Standard and a Measurement of the Frequency Shift due to Ultracold Collisions*, Phys. Rev. Lett. **70**, 1771 (1993).

- [Gil01] S. Gilbert and W. Swann, *Acetylene $^{12}\text{C}_2\text{H}_2$ absorption reference for 1510 nm to 1540 nm wavelength calibration - SRM2517a*, Natl. Inst. Stand. Technol. (US) Spec. Publ. **260-133** (2001).
- [Gre02] M. Greiner, O. Mandel, T. Esslinger, T. W. Hänsch, and I. Bloch, *Quantum phase transition from a superfluid to a Mott insulator in a gas of ultracold atoms*, Nature **415**, 39 (2002).
- [Gre03] M. Greiner, C. Regal, and D. Jin, *Emergence of a molecular Bose-Einstein condensate from a Fermi gas*, Nature **426**, 537 (2003).
- [Gri93] G. F. Gribakin and V. V. Flambaum, *Calculation of the scattering length in atomic collisions using the semiclassical approximation*, Phys. Rev. A **48**, 546 (1993).
- [Gri00] R. Grimm, M. Weidemüller, and Y. Ovchinnikov, *Optical dipole traps for neutral atoms*, Adv. At. Mol. Opt. Phys. **42** (2000).
- [Hag99] E. Hagley, L. Deng, M. Kozuma, J. Wen, K. Helmerson, S. Rolston, and W. Phillips, *A well-collimated quasi-continuous atom laser*, Science **283**, 1706 (1999).
- [Hal76] J. Hall and S. Lee, *Interferometric real-time display of cw dye laser wavelength with sub-Doppler accuracy*, Appl.Phys.Lett. **29**, 367 (1976).
- [Hei00] D. J. Heinzen, R. Wynar, P. D. Drummond, and K. V. Kheruntsyan, *Superchemistry: Dynamics of Coupled Atomic and Molecular Bose-Einstein Condensates*, Phys. Rev. Lett. **84**, 5029 (2000).
- [Her03] J. Herbig, T. Kraemer, M. Mark, T. Weber, C. Chin, H.-C. Nägerl, and R. Grimm, *Preparation of a Pure Molecular Quantum Gas*, Science **301**, 1510 (2003).
- [Her05] J. Herbig, *Quantum-degenerate cesium: Atoms and molecules*, Ph.D. thesis, University of Innsbruck (2005).
- [Hil07] W. Hill and C. Lee, *Light-Matter Interactions: Atoms and Molecules in External Fields and Nonlinear Optics*, Wiley-VCH, Weinheim, 2007.
- [Hou01] J. T. Hougen, *The Calculation of Rotational Energy Levels and Rotational Line Intensities in Diatomic Molecules*, NBS Monograph 115 (<http://physics.nist.gov/Pubs/Mono115/>) (1970 - online: 2001).
- [Hud02] J. Hudson, B. Sauer, M. Tarbutt, and E. Hinds, *Measurement of the Electron Electric Dipole Moment Using YbF Molecules*, Physical Review Letters **89**, 23003 (2002).
- [Ino98] S. Inouye, M. R. Andrews, J. Stenger, H.-J. Miesner, D. M. Stamper-Kurnand, and W. Ketterle, *Observation of Feshbach resonances in a Bose-Einstein condensate*, Nature **392**, 151 (1998).

References

- [Jak02] D. Jaksch, V. Venturi, J. I. Cirac, C. J. Williams, and P. Zoller, *Creation of a Molecular Condensate by Dynamically Melting a Mott Insulator*, Phys. Rev. Lett. **89**, 040402 (2002).
- [Joc03a] S. Jochim, M. Bartenstein, A. Altmeyer, G. Hendl, S. Riedl, C. Chin, J. H. Denschlag, and R. Grimm, *Bose-Einstein condensation of molecules*, Science **302**, 2101 (2003).
- [Joc03b] S. Jochim, M. Bartenstein, A. Altmeyer, G. Hendl, C. Chin, J. H. Denschlag, and R. Grimm, *Pure Gas of Optically Trapped Molecules Created from Fermionic Atoms*, Phys. Rev. Lett. **91**, 240402 (2003).
- [Jon06] K. M. Jones, E. Tiesinga, P. D. Lett, and P. S. Julienne, *Ultracold photoassociation spectroscopy: Long-range molecules and atomic scattering*, Reviews of Modern Physics **78**, 483 (2006).
- [Ket96] W. Ketterle and N. J. van Druten, *Evaporative Cooling of Trapped Atoms*, Adv. At. Mol. Opt. Phys. **37**, 181 (1996).
- [Ket99] W. Ketterle, D. S. Durfee, and D. M. Stamper-Kurn, *Making, probing and understanding Bose-Einstein condensates*, in: M. Inguscio, S. Stringari, and C. E. Wieman (Eds.), *Proceedings of the International School of Physics - Enrico Fermi*, 67, IOS Press, 1999.
- [Ket02] W. Ketterle, *Nobel lecture: When atoms behave as waves: Bose-Einstein condensation and the atom laser*, Rev. Mod. Phys. **74**, 1131 (2002).
- [Kha02] L. Khaykovich, F. Schreck, G. Ferrari, T. Bourdel, J. Cubizolles, L. D. Carr, Y. Castin, and C. Salomon, *Formation of a Matter-Wave Bright Soliton*, Science **296**, 1290 (2002).
- [Kin05] I. Kinski, *Magnetic Trapping Apparatus and Frequency Stabilization of a Ring Cavity Laser for Bose-Einstein Condensation Experiments*, Master's thesis, Freie Universität Berlin (2005).
- [Kiu81] K. Kiu and M. Littman, *Novel geometry for single mode scanning of tunable lasers*, Optics Letters **6**, 117 (1981).
- [Koc06a] C. Koch, private communication (2006).
- [Koc06b] C. P. Koch, R. Kosloff, and F. Masnou-Seeuws, *Short-pulse photoassociation in rubidium below the D_1 line*, Physical Review A **73**, 043409 (2006).
- [Koh06] T. Kohler, K. Goral, and P. S. Julienne, *Production of cold molecules via magnetically tunable Feshbach resonances*, Reviews of Modern Physics **78**, 1311 (2006).
- [Kok00a] V. Kokoouline, O. Dulieu, R. Kosloff, and F. Masnou-Seeuws, *Theoretical treatment of channel mixing in excited Rb_2 and Cs_2 ultracold molecules: Determination of predissociation lifetimes with coordinate mapping*, Phys. Rev. A **62**, 032716 (2000).

- [Kok00b] V. Kokoouline, O. Dulieu, and F. Masnou-Seeuws, *Theoretical treatment of channel mixing in excited Rb_2 and Cs_2 ultracold molecules: Perturbations in 0_u^+ photoassociation and fluorescence spectra*, Phys. Rev. A **62**, 022504 (2000).
- [Kow78] F. Kowalski, R. Teets, W. Demtroeder, and A. Schawlow, *Improved wavemeter for cw lasers (E)*, J. Opt. Soc. Am **68**, 1611 (1978).
- [Kra04] T. Kraemer, J. Herbig, M. Mark, T. Weber, C. Chin, H.-C. Nägerl, and R. Grimm, *Optimized production of a cesium Bose-Einstein condensate*, Appl. Phys. B **79**, 1013 (2004).
- [Kra05] S. D. Kraft, M. Mudrich, M. U. Staudt, J. Lange, O. Dulieu, R. Wester, and M. Weidemüller, *Saturation of Cs_2 photoassociation in an optical dipole trap*, Physical Review A **71**, 013417 (2005).
- [Kra06a] T. Kraemer, Ph.D. thesis, University of Innsbruck (2006).
- [Kra06b] T. Kraemer, M. Mark, P. Waldburger, J. Danzl, C. Chin, B. Engeser, A. Lange, K. Pilch, A. Jaakola, H.-C. Nägerl, and R. Grimm, *Evidence for Efimov quantum states in an ultracold gas of caesium atoms*, Nature **440**, 315 (2006).
- [Lab94] M. de Labachellerie, K. Nakagawa, and M. Ohtsu, *Ultranarrow $^{13}C_2H_2$ saturated absorption lines at 1.5 μm* , Optics Letters **19**, 840 (1994).
- [LB04] H. Lefebvre-Brion and R. Field, *The Spectra and Dynamics of Diatomic Molecules*, Elsevier, 2004.
- [Leo00] P. J. Leo, C. J. Williams, and P. S. Julienne, *Collision Properties of Ultracold ^{133}Cs Atoms*, Phys. Rev. Lett. **85**, 2721 (2000).
- [Lit78a] M. Littman, *Single-mode operation of grazing-incidence pulsed dye laser*, Optics Letters **3**, 138 (1978).
- [Lit78b] M. Littman and H. Metcalf, *Spectrally narrow pulsed dye laser without beam expander*, Applied Optics **17**, 2224 (1978).
- [Lit84] M. Littman, *Single-mode pulsed tunable dye laser*, Applied Optics **23**, 4465 (1984).
- [LK04] E. Luc-Koenig, M. Vatasescu, and F. Masnou-Seeuws, *Optimizing the photoassociation of cold atoms by use of chirped laser pulses*, Eur. Phys. J. D **31**, 239 (2004).
- [Mad06] A. Madej, A. Alcock, A. Czajkowski, J. Bernard, and S. Chepurov, *Accurate absolute reference frequencies from 1511 to 1545 nm of the $v_1 + v_3$ band of $^{12}C_2H_2$ determined with laser frequency comb interval measurements*, J. Opt. Soc. Am. B **23**, 2200 (2006).
- [Mar03] M. Mark, *Bose -Einstein-Kondensation von Caesium*, Master's thesis, University of Innsbruck (2003).

References

- [Mar05] M. Mark, T. Kraemer, J. Herbig, C. Chin, H.-C. Nägerl, and R. Grimm, *Efficient creation of molecules from a cesium Bose-Einstein condensate*, *Europhysics Letters* **69** (2005).
- [Mar07] M. Mark, F. Ferlaino, S. Knoop, J. G. Danzl, T. Kraemer, C. Chin, H. C. Nägerl, and R. Grimm, *Spectroscopy of Cesium Feshbach Molecules*, to be submitted (2007).
- [Mat99] M. R. Matthews, B. P. Anderson, P. C. Haljan, D. S. Hall, C. Wieman, and E. A. Cornell, *Vortices in a Bose-Einstein Condensate*, *Phys. Rev. Lett.* **83**, 2498 (1999).
- [Met99] H. J. Metcalf and P. van der Straten, *Laser cooling and trapping*, Springer-Verlag, New York, 1999.
- [Mew97] M.-O. Mewes, M. R. Andrews, D. M. Kurn, D. S. Durfee, C. G. Townsend, and W. Ketterle, *Output Coupler for Bose-Einstein Condensed Atoms*, *Phys. Rev. Lett.* **78**, 582 (1997).
- [Mil93] J. D. Miller, R. A. Cline, and D. J. Heinzen, *Photoassociation Spectrum of Ultracold Rb Atoms*, *Phys. Rev. Lett.* **71**, 2204 (1993).
- [Mod01] G. Modugno, G. Ferrari, G. Roati, R. J. Brecha, A. Simoni, and M. Inguscio, *Bose-Einstein Condensation of Potassium Atoms by Sympathetic Cooling*, *Science* **294**, 1320 (2001).
- [MS01] F. Masnou-Seeuws and P. Pillet, *Formation of ultracold molecules ($T \leq 200 \mu\text{K}$) via photoassociation in a gas of laser-cooled atoms*, *Advances in Atomic, Molecular, and Optical Physics* **47**, 53 (2001).
- [Nel97] L. Nelsen, D. Jones, K. Tamura, H. Haus, and E. Ippen, *Ultrashort-pulse fiber ring lasers*, *Appl. Phys. B* **65**, 277 (1997).
- [Nik00] A. N. Nikolov, J. R. Ensher, E. E. Eyler, H. Wang, W. C. Stwalley, and P. L. Gould, *Efficient Production of Ground-State Potassium Molecules at Sub-mK Temperatures by Two-Step Photoassociation*, *Phys. Rev. Lett.* **84**, 246 (2000).
- [NIS07] NIST, *Chemistry WebBook*, <http://webbook.nist.gov> (2007).
- [Ona97] A. Onae, K. Okumura, Y. Miki, T. Kurosawa, E. Sakuma, J. Yoda, and K. Nakagawa, *Saturation spectroscopy of an acetylene molecule in the 1550 nm region using an erbium doped fiber amplifier*, *Optics Communications* **142**, 41 (1997).
- [PDS02] F. Pereira Dos Santos, H. Marion, S. Bize, Y. Sortais, A. Clairon, and C. Salomon, *Controlling the Cold Collision Shift in High Precision Atomic Interferometry*, *Phys. Rev. Lett.* **89**, 233004 (2002).
- [Pet02] C. J. Pethick and H. Smith, *Bose-Einstein Condensation in Dilute Gases*, Cambridge University Press, 2002.

- [Phi98] W. D. Phillips, *Laser cooling and trapping of neutral atoms*, Rev. Mod. Phys. **70**, 721 (1998).
- [Pic04] M. Pichler, W. C. Stwalley, R. Beuc, and G. Pichler, *Formation of ultracold Cs₂ molecules through the double-minimum Cs₂ 3¹Σ_u⁺ state*, Physical Review A **69**, 013403 (2004).
- [Pic06] M. Pichler, W. C. Stwalley, and O. Dulieu, *Perturbation effects in photoassociation spectra of ultracold Cs₂*, J.Phys.B: At.Mol.Opt.Phys. **39**, S981 (2006).
- [Pit03] L. Pitaevskii and S. Stringari, *Bose-Einstein Condensation*, International Series of Monographs on Physics 116, Oxford University Press, 2003.
- [Raj79] R. Raj, D. Bloch, J. Sydner, G. Camy, and M. Ducloy, *High-Frequency Optically Heterodyned Saturation Spectroscopy Via Resonant Degenerate Four-Wave Mixing*, Phys. Rev. Lett. **32**, 145 (1979).
- [Reg03] C. A. Regal, C. Ticknor, J. L. Bohn, and D. S. Jin, *Creation of ultracold molecules from a Fermi gas of atoms*, Nature **424**, 47 (2003).
- [Sag05] J. M. Sage, S. Sainis, T. Bergeman, and D. DeMille, *Optical Production of Ultracold Polar Molecules*, Phys. Rev. Lett. **94**, 203001 (2005).
- [Sal91] B. Saleh and M. Teich, *Fundamentals of Photonics*, John Wiley and Sons, 1991.
- [Sam00] C. Samuelis, E. Tiesinga, T. Laue, M. Elbs, H. Knöckel, and E. Tiemann, *Cold atomic collisions studied by molecular spectroscopy*, Phys. Rev. A **63**, 012710 (2000).
- [Sie86] A. E. Siegmann, *Lasers*, University Science Books, Mill Valley, 1986.
- [Spi89] N. Spiess, Ph.D. thesis, Universität Kaiserslautern, Fachbereich Chemie (1989).
- [Ste03] D. Steck, *Cesium D Line Data*, <http://steck.us/alkalidata> (2003).
- [Sto06] J. A. Stone and J. H. Zimmerman, *Index of Refraction of Air*, <http://emtoolbox.nist.gov/Main/Main.asp> (2006).
- [Str02] K. E. Strecker, G. B. Partridge, A. G. Truscott, and R. Hulet, *Formation and propagation of matter-wave soliton trains*, Nature **417**, 150 (2002).
- [Str03] K. E. Strecker, G. B. Partridge, and R. G. Hulet, *Conversion of an atomic Fermi gas to a long-lived molecular Bose gas*, Phys. Rev. Lett. **91**, 080406 (2003).
- [Str07] P. van der Straten, private communication (2007).
- [Stu04] R. Stutz and E. Cornell, Bull. Am. Soc. Phys. **89**, 76 (2004).
- [Stw76] W. C. Stwalley, *Stability of Spin-Aligned Hydrogen at Low Temperatures and High Magnetic Fields: New Field-Dependent Scattering Resonances and Predissociations*, Phys. Rev. Lett. **37**, 1628 (1976).

References

- [Stw04] W. Stwalley, *Efficient conversion of ultracold Feshbach-resonance-related polar molecules into ultracold ground state ($X^1\Sigma^+$, $v = 0$, $J = 0$) molecules*, Eur. Phys. J. D **31**, 221 (2004).
- [Swa00] W. Swann and S. Gilbert, *Pressure-induced shift and broadening of 1510-1540-nm acetylene wavelength calibration lines*, J.Opt.Soc.Am.B **17**, 1263 (2000).
- [Tak98] T. Takekoshi, B. M. Patterson, and R. J. Knize, *Observation of Optically Trapped Cold Cesium Molecules*, Phys. Rev. Lett. **81**, 5105 (1998).
- [Tie93] E. Tiesinga, B. Verhaar, and H. T. C. Stoof, *Threshold and resonance phenomena in ultracold ground-state collisions*, Phys. Rev. A **47**, 4114 (1993).
- [Ude02] T. Udem, R. Holzwarth, and T. Hänsch, *Optical frequency metrology*, Nature **416**, 233 (2002).
- [Van04] N. Vanhaecke, C. Lisdat, B. T'Jampens, D. Comparat, A. Crubellier, and P. Pillet, *Accurate asymptotic ground state potential curves of Cs_2 from two-color photoassociation*, European Physical Journal D **28**, 351 (2004).
- [Ver87] J. Vergès and C. Amiot, *The Cs_2 $A^1\Sigma_g^+$ Fluorescence Excited by the Ar^+ 1.09- μ m Laser Line*, Journal of Molecular Spectroscopy **126**, 393 (1987).
- [Vit97] N. V. Vitanov and S. Stenholm, *Population transfer via a decaying state*, Phys. Rev. A **56**, 1463 (1997).
- [Vit01] N. Vitanov, T. Halfmann, B. W. Shore, and K. Bergmann, *Laser-induced population transfer by adiabatic passage techniques*, Annu. Rev. Phys. Chem. **52**, 763 (2001).
- [Vul99a] V. Vuletić, C. Chin, A. J. Kerman, and S. Chu, *Suppression of Atomic Radiative Collisions by Tuning the Ground State Scattering Length*, Phys. Rev. Lett. **83**, 943 (1999).
- [Vul99b] V. Vuletić, A. J. Kerman, C. Chin, and S. Chu, *Observation of Low-Field Feshbach Resonances in Collisions of Cesium Atoms*, Phys. Rev. Lett. **82**, 1406 (1999).
- [Wan97] H. Wang, P. Gould, and W. Stwalley, *Long range interaction of the $^{39}K(4s)+^{39}K(4p)$ asymptote by photoassociation spectroscopy. I. The 0_g^- pure long-range state and the long-range potential constants*, J.Chem.Phys. **106**, 7899 (1997).
- [Web03a] T. Weber, *Bose-Einstein condensation of optically trapped cesium*, Ph.D. thesis, University of Innsbruck (2003).
- [Web03b] T. Weber, J. Herbig, M. Mark, H.-C. Nägerl, and R. Grimm, *Bose-Einstein Condensation of Cesium*, Science **299**, 232 (2003).
- [Web03c] T. Weber, J. Herbig, M. Mark, H.-C. Nägerl, and R. Grimm, *Three-body recombination at large scattering lengths in an ultracold atomic gas*, Phys. Rev. Lett. **91**, 123201 (2003).

- [Wei85] U. Weickenmeier, M. Diemer, M. Wahl, M. Raab, W. Demtröder, and W. Müller, *Accurate ground state potentials of Cs₂ up to the dissociation limit*, J.Chem.Phys. **82**, 5354 (1985).
- [Wei98] J. D. Weinstein, R. deCarvalho, T. Guillet, B. Friedrich, and J. M. Doyle, *Magnetic trapping of calcium monohydride molecules at millikelvin temperatures*, Nature **395**, 148 (1998).
- [Wei99] J. Weiner, V. S. Bagnato, S. Zilio, and P. S. Julienne, *Experiments and theory in cold and ultracold collisions*, Rev. Mod. Phys. **71**, 1 (1999).
- [Wes04] R. Wester, S. Kraft, M. Mudrich, M. Staudt, J. Lange, N. Vanhaecke, O. Dulieu, and M. Weidemüller, *Photoassociation inside an optical dipole trap: absolute rate coefficients and Franck-Condon factors*, Applied Physics B: Lasers and Optics **79**, 993 (2004).
- [Win06a] K. Winkler, private communication (2006).
- [Win06b] K. Winkler, F. Lang, G. Thalhammer, P. v d Straten, R. Grimm, and J. H. Denschlag, *Coherent optical transfer of Feshbach molecules to a lower vibrational state*, arXiv.org:cond-mat/0611222 (2006).
- [Woo09] R. Wood and F. Hackett, *Astrophys. J.* **30**, 339 (1909).
- [Xu03] K. Xu, T. Mukaiyama, J. R. Abo-Shaeer, J. K. Chin, D. E. Miller, and W. Ketterle, *Formation of Quantum-Degenerate Sodium Molecules*, Phys. Rev. Lett. **91**, 210402 (2003).
- [Ye06a] J. Ye, private communication (2006).
- [Ye06b] J. Ye, S. Blatt, M. M. Boyd, S. M. Foreman, E. R. Hudson, T. Ido, B. Lev, A. D. Ludlow, B. C. Sawyer, B. Stuhl, and T. Zelevinsky, *Precision Measurement Based on Ultracold Atoms and Cold Molecules*, in: C. Roos, H. Haffner, and R. Blatt (Eds.), *ATOMIC PHYSICS 20: XX International Conference on Atomic Physics - ICAP 2006*, vol. 869, 80–91, AIP, 2006.
- [Zwi05] M. W. Zwierlein, J. R. Abo-Shaeer, A. Schirotzek, C. H. Schunck, and W. Ketterle, *Vortices and superfluidity in a strongly interacting Fermi gas*, Nature **435**, 1047 (2005).

Acknowledgments

After finishing medical school I was wondering about what to do for my diploma thesis in physics. At the time I was close to doing a medical postdoc that would have some physics connection. But then I was fascinated by the field of ultracold quantum gases and decided that it's a good idea to get a solid experimental physics background after going through all the coursework. I had the pleasure to join a very active and stimulating group. Therefore, I would first like to thank Rudi Grimm for providing me with the opportunity to join his group. Rudi is a far sighted scientist and he has created a very motivated and productive group here in Innsbruck. His advice and intellectual input has to a large extent determined the success of the individual experiments and it is a pleasure to work in such an environment.

Hanns-Christoph Nägerl is in charge of the cesium experiments and he is crucially contributing to the experiments with both his technical and his scientific expertise. He had the idea for the spectroscopy project and he has been an encouraging mentor during the entire time. I very much appreciate that Hanns-Christoph has given me the opportunity to solve problems independently but was always there to help when I needed advice. Thanks as well for showing me the best off-piste skiing and snowboarding at the Nordkette.

I'm indebted to the LevT team for the good working atmosphere, for all their help and for the fun we had. Tobias Kraemer and Michael Mark did a great job as PhD students running the experiment and improving it. Michael helped with adjusting the spectroscopy beam and building a dipole trap with it and both were eager climbing partners. Francesca Ferlaino and Steven Knoop are both very motivated and competent postdocs pushing the experiment forward. Harald Schöbel and Martin Berninger have recently joined the team and they are working on new directions the experiment is heading for. Jens Herbig was among the first generation LevT people and, after finishing his PhD, he helped starting off the spectroscopy project, which is gratefully acknowledged. I would also like to thank the two student apprentices who have helped on the project for a few weeks, namely Lukas An der Lan and Manfred Mark who are both doing a diploma thesis in quantum physics now.

During the buildup phase the spectroscopy setup was hosted in the Rb lab due to space limitations in the LevT. I'm grateful to the Rb team led by Johannes Hecker Denschlag for sharing their lab space with me and for the good cooperation. These are Gregor Thalhammer, Klaus Winkler, Florian Lang, Sascha Hoinka and Stefan Schmid. Especially the senior PhD students Gregor and Klaus were always willing to share their technical expertise with me and therefore have made many things much easier.

I would like to thank all the other members of the group for the very open and constructive attitude. Part of the success of the group relies on the fact that knowledge transfer between the experiments works so smoothly. In addition to those mentioned before, these are the GOST, the CsIII, the Li and the FeLiKx teams.

There are several people outside Innsbruck who have provided very valuable input to the spectroscopy project. Olivier Dulieu and Nadia Bouloufa from Orsay have calcu-

lated Franck-Condon factors, which is gratefully acknowledged. Moreover, they have provided valuable advice and explanations. Together with Anne Crubellier they are currently setting up calculations for expected transition rates including the hyperfine interaction in the ground state. Thanks to Olivier as well for organizing a great workshop in Les Houches.

Christiane Koch from Berlin has been a great source of insight concerning molecular physics. She has always been available for clarifying my questions and providing me with a clearer picture of what molecules are all about. I very much appreciate her help and I'm grateful for proofreading chapter 3 of this thesis.

Peter van der Straten from Utrecht, one of the authors of the "yellow pages", visited us as a guest professor for several months. He has been very accessible to discussions and it was a pleasure to have him here. He did calculations on the structure of Feshbach molecules in order to help me find a good molecular state to start with for the optical spectroscopy. The code was provided by Paul Julienne, which is also gratefully acknowledged.

On the technical side, support both from Manuel Kluibenschädl and Arthur Wander in the electronic workshop and from Josef Dummer, Anton Schönherr and Helmut Jordan in the mechanical workshop is greatly appreciated. Arthur ventured out into the realm of microcontrollers with me and Manuel, Josef, Toni and Helmut were always willing to help.

When it comes to administrative tasks, Christine Götsch-Obmascher, Karin Köhle and Gabriel Wenger are always supportive and I would like to thank them.

I would like to thank the University of Innsbruck for their open mindedness and belief in the potential of interdisciplinary education when granting me a postdoc scholarship in acknowledgment of my medical degree.

In addition to the people who have contributed to the project directly, I owe my sincere gratitude to my family, my friends and my girlfriend Barbara who have provided a very supportive environment.

All these people have contributed in one or the other way and have made the decision to do some really cold stuff a very good one.